Doctoral Dissertation
Doctoral Program in Science and technology of materials (29th Cycle)

Thermally conductive polymer/graphene-related materials nanocomposites prepared by melt reactive processing

By

Samuele Colonna

******

Supervisor:
Prof. A. Fina, Supervisor

Doctoral Examination Committee:
Prof. Karl Schulte, Referee, Technische Universität Hamburg
Prof. Maurizio Galimberti , Referee, Politecnico di Milano
Prof. Emiliano Bilotti, Referee, Queen Mary University of London
Prof. Francesco Geobaldo, Referee, Politecnico di Torino
Prof. Giulio Malucelli, Referee, Politecnico di Torino

Politecnico di Torino
2016

Declaration

I hereby declare that, the contents and organization of this dissertation constitute my own original work and does not compromise in any way the rights of third parties, including those relating to the security of personal data.

Samuele Colonna

2017

* This dissertation is presented in partial fulfillment of the requirements for **Ph.D. degree** in the Graduate School of Politecnico di Torino (ScuDo).

Alla mia Famiglia!

Acknowledgment

Firstly, I would like to thank my supervisor, Prof. Alberto Fina, for his tutorship and support. Its ideas, suggestions and constructive comments provided me a strong background for my personal growth in the responsible organization of the scientific research. Great thanks are also due to Prof. Alejandro Jesus Müller for giving me the opportunity to join his group at POLYMAT, Centre for Polymeric Materials (University of the Basque Country), and to learn much about crystallization of polymer materials.

A special mention to all the colleagues, at the Politecnico, which helped me in growing both from the scientific and from the personal point of view. A special thanks to the Advanced Multiphasic Groups in San Sebastian, where I met brilliant scientist, colleagues and true friends. Lastly, and most importantly, I want to express my gratitude to my girlfriend and to my family, who supported me during these long three years.

Abstract

Polymer nanocomposites containing graphene-related materials attracted a wide research interest thanks to the combination of the processability, lightweight and corrosion resistance typical of polymers, with the outstanding properties of graphene-related materials, including mechanical properties, thermal conductivity and electrical conductivity. Nanocomposites exploiting graphene-related materials are indeed showing interesting properties and several industrial applications for such nanomaterials are currently being developed, including structural materials, as well as functional materials, electrodes and conductors in flexible electronics, waste heat management, gas-barrier materials, etc., also taking into advantage of the large European initiative for graphene research, development and application called Graphene Flagship (http://graphene-flagship.eu/).

This thesis aims to the preparation of polymer nanocomposites, exploiting graphene-related materials, by the development of industrially viable preparation methods, for the application as heat management materials. These are currently of interest in several application fields, including low temperature heat recovery, heat exchange in highly corrosive environments as well as heat dissipation in electronics and flexible electronics. Beside the thermal conductivity property, this PhD thesis was aimed at the fundamental understanding of phenomena controlling nanoparticle dispersion into the polymer matrix as well as the correlations between structure and properties of the prepared materials, including electrical conductivity, rheological properties and polymer crystallization phenomena.

As the availability of graphene (*i.e.* a single layer of sp^2 carbons) nanoflakes remains extremely limited and insufficient for the exploitation in large scale applications embedding graphene in the polymer bulk, different types of graphene-related materials were selected for exploitation in this PhD thesis, namely graphite nanoplatelets (GNP) and reduced graphene oxide (rGO). In particular, different grades of GNP and rGO were selected aiming at the

correlation between their quality, mainly in terms of defectiveness and aspect ratio, and the properties of their corresponding polymer nanocomposite. For these reasons, the initial part of this thesis is focused on thorough characterization of nanoflake quality, *i.e.* defectiveness and aspect ratio, through electron microscopy, Raman spectroscopy, X-ray photoelectron spectroscopy and thermogravimetric analysis. On the other hand, the second part is focused on the preparation and detailed characterization of nanocomposites prepared by ring opening polymerization of polyester oligomers (CBT) during melt mixing in presence of graphene-related materials. In particular, the effects of the exploitation of different graphene-related materials, of the polymerization during reactive mixing and of the processing parameters (processing temperature, time and shear rate) on the electrical and thermal properties of polymer nanocomposites is addressed. Thorough characterization of the effect of the exploitation of pristine and high temperature-annealed reduced graphene oxide on the nanocomposite properties is also reported, in terms of both of conductivities and modification in the crystallization of the polymer matrix.

The results reported in this thesis demonstrate the viability of CBT polymerization during melt mixing with graphene-related materials to produce thermally and electrically conductive polymer nanocomposites aiming at possible industrial applications.

Index

List of Figures

List of Tables

List of abbreviations

BE:	Binding Energy
CB:	Carbon Black
CBT:	Cyclic Butylene Terephthalate oligomers
CF:	Carbon Fibers
CNT:	Carbon NanoTubes
CVD:	Chemical Vapor Deposition
DMTA:	Dynamic Mechanical Thermal Analysis
DSC:	Differential Scanning Calorimetry
EVA:	Ethylene-Vinyl Acetate
FESEM :	Field-Emission Scanning Electron Microscopy
FLG:	Few-Layer Graphene
FWHM:	Full-Width at Half Maximum
GIC:	Graphite Intercalated Compounds
GNP:	Graphite Nanoplatelets or Graphite Nanoplates
GO:	Graphene Oxide
GRM:	Graphene-Related Materials
h-BN:	Hexagonal Boron Nitride
HDPE:	High Density PolyEthylene
HFIP:	1,1,1,3,3,3 HexaFluoroIsoPropanol
HOPG:	Highly Oriented Pyrolytic Graphite
LDPE:	Low Density PolyEthylene

LH:	Lauritzen-Hoffman
LPE:	Liquid-Phase Exfoliation
MLG:	Multi-Layer Graphene
NE:	Nucleation Efficiency
NMP:	N-Methyl-2-pyrrolidone
Ox-GIC:	Oxidized Graphite intercalated compound
PA6:	PolyAmide 6
PA66:	PolyAmide 6.6
PBT:	Poly (Butylene Terephthalate)
PC:	PolyCarbonate
pCBT:	poly Butylene Terephthalate (obtained from CBT)
PE:	PolyEthylene
PET:	Poly (Ethylene Terephthalate)
PI:	PolyImide
PLA:	Poly (Lactic Acid)
PMMA:	Poly (MethylMethAcrylate)
PP:	PolyPropylene
PPC:	Poly(Propylene Carbonate)
PPS:	Poly (Phenylene Sulfide)
PS:	PolyStyrene
PTFE:	PolyTetraFluoroEthylene
PU:	PolyUrethane

PVA:	Poly (Vinyl Alcohol)
PVDF:	Poly (VinyliDene Fluoride)
PVDF-HFP:	Poly (VinyliDene Fluoride-co-HexaFluoroPropylene)
RGO:	Reduced Graphene Oxide
rpm:	revolutions per minutes
SiC:	Silicon Carbide
Si3N4:	Silicon Nitride
SiO2:	Silica
SN:	Self-Nucleation
SSA:	Successive Self-nucleation and Annealing
TGA:	ThermoGravimetric Analysis
THF:	TetraHydroFuran
v/v:	volume/volume concentration
WAXS:	Wide-Angle X-ray Scattering
XPS:	X-ray Photoelectron Spectroscopy
XRD:	X-ray diffraction

List of symbols

δ	-	Phase lag between stress and strain in DMTA
ΔH_c:	[J g^{-1}]	crystallization enthalpy
ΔH_m:	[J g^{-1}]	melting enthalpy
ε_b:	[%]	elongation at break
η^*:	[Pa s]	complex viscosity
Θ:	[°]	diffraction angle
λ:	[W m^{-1} K^{-1}]	thermal conductivity
σ:	[S m^{-1}]	electrical conductivity
Σ_{max}:	[MPa]	maximum stress
ϕ:	[%]	filler volume content
ϕ_c:	[%]	electrical percolation threshold
φ:	[%]	filler weight content
ω	[rad s^{-1}]	angular frequency
C_{1s}:	-	Carbon 1s
D:	[nm]	correlation lenght
d_{50}:	[µm]	relative amount of particles: 50% of particles have size below the indicated size
E:	[GPa]	elastic modulus

E':	[MPa]	storage modulus (measured by DMTA)
E'':	[MPa]	loss modulus (measured by DMTA)
G':	[Pa]	storage modulus (measured by rheology)
G'':	[Pa]	loss modulus (measured by rheology)
K_{IC}:	[MPa $m^{0.5}$]	fracture toughness
I:	[C/S]	x-ray diffraction patterns intensity
I_D:	-	Raman intensity of the graphene D-band (~ 1350 cm^{-1})
I_G:	-	Raman intensity of the graphene G-band (~ 1580 cm^{-1})
m_p:	[°C]	melting point
M_v:	[kg mol^{-1}]	viscosity-average molecular weight
M_W:	[kg mol^{-1}]	molecular weight
n:	-	Avrami Index
n:	-	Wagener and Reisinger equation exponential factor
N/N_{tot}:	-	relative amount of nanoflakes with a given projected area
O_{1s}:	-	Oxygen 1s
T:	[°C]	temperature
T_c:	[°C]	crystallization temperature
T_m:	[°C]	melting temperature
T_{max}:	[°C]	maximum temperature

T_{onset}:	[°C]	temperature at which the material loose about 3 wt.% of its initial weight
T_{peak}:	[°C]	temperature at which is observed the Tanδ peak
T_s:	[°C]	self-nucleation temperature
$T_{s,ideal}$:	[°C]	ideal self-nucleation temperature
Tanδ:	-	tangent of δ
X_c	[%]	Crystallinity degree

Chapter 1

Introduction

Polymers are versatile materials, which have been exploited for a wide range of applications, including packaging, biomedical, buildings, automotive, aerospace sectors. Often, the exploitation of polymers is related to their electrical and thermal insulation properties [1-3], *e.g.* to insulation of conducting copper cables, reduction of the dissipation of heat in buildings, etc. However, for some application the peculiar properties of polymers, like corrosion resistance, processability, low cost, attracted the attention for their exploitation as electrically and/or thermally conductive materials, including heat exchangers, sensors, etc. [1, 4, 5]. Regarding electrical conductivity, it is worth noting that it exists a class of polymers which are intrinsically electrically conductors: these materials are characterized by the presence of conjugation in the chain backbone [3, 6]. Doping of this materials, by exposure to a corresponding gas or placing the material in a corresponded liquid, can lead to the addition of oxidizing or reducting species, which act as positive or negative charge carriers, respectively, resulting in electrical conductivity values up to 10^6-10^7 S m^{-1}. However, such materials suffer from poor processability, high cost and loss of electrical conduction properties over the time [3]. For these reasons, often the exploitation of electrically conductive fillers in conventional polymer matrices is preferred, combining the high electrical conductivity of fillers and the processability, corrosion resistance and low cost of common polymer matrices [7-9]. Mixing of polymer matrices with the proper filler is a typical way for the improvement of the thermal conductivity of polymers [1, 4, 10], and will be thoroughly described in the following section.

1.1 Thermal conductivity of polymers

Thermal conductivity is an intrinsic property that indicates the ability of a material to transfer heat by conduction. For one-dimensional, steady state heat flow, the heat conduction rate is expressed by the following Fourier's equations [11]:

$$q = \lambda A \frac{\Delta T}{L} \quad (1)$$

or

$$J = \frac{q}{A} = -\lambda \frac{dT}{dX} \quad (2)$$

with q = heat transfer rate (W), J = heat flux (W m^{-2}), λ = thermal conductivity (W m^{-1} K^{-1}), A = cross sectional transfer area (m^2); ΔT represent the temperature difference (°C) between two parallel surfaces A separated by a distance L (m).

At molecular level, the heat transport process typically involves the energy transfer by collisions, which lead to exchange of energy and momentum from the more energetic molecules to those with a lower energy level. This results in a continuous transfer of energy from high- to low-temperature regions [12]. In solids, the main heat transfer mode is, in general, conduction and the energy can be carried out by electrons, phonons or photons [1]. Phonons are quantized modes of vibration occurring in a rigid crystal lattice and are the principal energy carrier in those solids that are nonconductors of electricity. In good conductors of electricity (*i.e.* metals), free electrons may also play a key role in the heat transfer. However, electrons are not always the principal energy carriers in electrically conductive materials: in fact, in graphene the contribute of electrons to heat transfer was estimated, at room temperature, between 0.4 and 10% of the total thermal conductivity of bulk graphene [13, 14].

Thermal conductivity can be theoretically obtained from the Debye equation:

$$\lambda = \frac{1}{3} C_p v l \quad (3)$$

where C_p is the volumetric heat capacity (J m^{-3} K^{-1}), v is the group velocity (m s^{-1}) and l is the mean free path (m); all these three parameters directly affect the thermal conductivity of materials.

Polymers are well-known insulating materials, with a thermal conductivity typically in the range 0.1 ÷ 0.5 W m^{-1} K^{-1} (Table 1), for which the energy carriers are phonons. Phonons in polymers are very much limited in their mean free path, owing to the amorphous or semicrystalline nature of polymers, which determines their low thermal conductivity. However, it is worth remembering that polymer chains are good thermal conductors along the axial direction. In fact, it was reported, by molecular dynamic simulations, that the thermal conductivity of single polyethylene (PE) chains with extended conformation could be as high as 350 W m^{-1} K^{-1}, along the axial direction, when the chain length is higher than 100 nm [11]. Furthermore, for most polymers, both volumetric heat capacity and phonon group velocity for individual chains are almost the same as those in bulk polymers. Thus, based on the Debye equation, above reported (eq. 3), the difference in thermal conductivity between bulk polymers and individual chains is related to phonon mean free path, as already proposed by Pietralla [15] to explain the low thermal conductivity of polymers. In bulk polymers, polymer chains are randomly oriented and exhibit a weak intermolecular coupling with other chains, mainly via van der Waals forces, resulting in a small phonon mean free path respect to that occurring in the skeleton of polymer chains. Furthermore it is worth observing that defects such as voids, entanglements, impurities further affect the phonon mean free path, resulting in the reduction of polymer thermal conductivity [16].

The crystallinity influence on the thermal conductivity of polymer matrices was reported to be related to the phonon mean free path. This was reported to be in the order of few angstroms for amorphous polymers [17, 18], whereas, in the crystalline fraction, of semi-crystalline polymers, it was estimated to be slightly higher. Indeed, Weidenfeller et al [18] reported a mean free path of ~ 0.450 nm and ~ 0.155 nm for the crystalline and amorphous fractions of polypropylene (PP), respectively. In their work the values were estimated considering a free path length of phonons in amorphous phase in the range of the distance of carbon atoms (in PP ~ 0.154 nm). On the other hand, the calculation of phonon mean free path in the crystalline phase was calculated by a simple rule of mixture between the crystalline and amorphous fractions, knowing the crystallinity of the material and the phonon mean free path in PP (~ 0.3 nm). The higher phonon mean free path in the crystalline phase is reflected on the generally higher thermal

conductivity observed for semi-crystalline polymers respect to the amorphous ones [19], as showed in Table 1. Furthermore, the thermal conductivity of semi-crystalline polymers was reported to increase with crystallinity, even if in literature a large scatter of values and some contradictory results are observed [1].

The orientation of polymer chains was reported to affect the thermal conductivity of polymers along the chain direction, especially for semi-crystalline polymers [11]. This was related to a longer phonon mean free path and to an increase in the overall crystallinity, which results in a better thermal transfer between crystals, despite an obvious phonon scattering due to the Van der Waals interaction between chains. However, in ultradrawn polyethylene nanofibers, a thermal conductivity up to ~ 100 W m^{-1} K^{-1}, along the fiber direction, was reported by Shen *et al.* [20]. On the other hand, in the radial direction low thermal conductivity values (in the range 0.1 ÷ 0.3 W m^{-1} K^{-1}) were measured, for different fibers, by using time-domain thermoreflectance [21].

Another parameter, which strongly affects the thermal conductivity of polymeric materials, is the chain structure. In fact, in a recent molecular dynamic simulation, Zhang *et al.* [22] reported that the presence of π-conjugated rigid backbone can suppress the rotation of chain segments, resulting in a higher phonon group velocity which lead to higher thermal conductivity for molecular chains. On the other hand, the opposite occurred when heteroatoms were included both as segments in the main chain or as lateral groups.

Finally, thermal conductivity of polymers is affected by the temperature, with different behavior observed for amorphous and semi-crystalline materials. In fact, amorphous materials exhibit an increase in the thermal conductivity up to the glass transition temperature (T_g) owed to the higher molecular mobility [16] whereas a decrease occurred above T_g [1, 23]. On the other hand, for semi-crystalline polymers, the thermal conductivity was observed to decrease as the temperature increases up to the melting point, owed to a decrease in the phonon mean free path and in the sample density [23].

Table 1. Thermal conductivities of some polymers [1, 11]

Material	Thermal conductivity at 25°C W m^{-1} K^{-1}
Low density polyethylene (LDPE)	0.30 ÷ 0.34
High density polyethylene (HDPE)	0.35 ÷ 0.53
Polypropylene (PP)	0.11 ÷ 0.17
Polystyrene (PS)	0.10 ÷ 0.15
Polycarbonate (PC)	0.19 ÷ 0.21
Polyamide 6 (PA6)	0.22 ÷ 0.33
Polyamide 6.6 (PA66)	0.24 ÷ 0.33
Poly (butylene terephthalate) (PBT)	0.24 ÷ 0.29
Poly (ethylene terephthalate) (PET)	0.14 ÷ 0.15
Poly (phenylene sulfide) (PPS)	0.30
Epoxy resin	0.19

1.2 Thermally conductive fillers

Despite the intrinsic low thermal conductivity of bulk polymers, some of their peculiar properties, like corrosion resistance, easily processing and lightweight, pushed for their exploitation as heat exchangers. To achieve this, different thermally conductive fillers, used alone or in combination, are typically exploited in polymer matrices [1, 10, 11, 16]. The thermal conductivity of these fillers ranges between ~ 20 and ~ 6000 W m^{-1} K^{-1} (Table 2), *i.e.* from two- up to four-order of magnitude higher than bulk polymers, depending on many factors including filler purity, particle size, crystallinity, measurement method, etc. Thermally conductive fillers can be classified based on their size, *i.e.* nanoparticles, microparticles, fibers, whiskers, etc. However, to allow a more

clear discussion, the different fillers will be classified into three classes: metals, ceramics and carbon.

Metallic fillers

In metals, heat is mainly transferred by the motion of free electrons, as above-mentioned. This is reflected on the thermal conductivity of metallic fillers, which usually is in the order of 10^2 W m^{-1} K^{-1} (Table 2). Metal based fillers have been widely used in literature for thermally conductive polymer composites [1, 11, 16]. They are quite effective in increasing thermal conductivity in composites, with improvements depending on the thermal conductivity of the filler, the particle aspect ratio, the volume fraction and the distribution and dispersion in the polymer matrix. However, their intrinsic electrical conductivity limited their use only in those applications where electrical insulation is not required. Furthermore, they cannot be exploited, in high concentration, in composites where lightweight is required, considering their typical high density.

Ceramic fillers

In ceramic fillers, the heat is mainly transferred by lattice vibration, *i.e.* phonons, owed to the lack of free electrons [11]. Not all the available ceramic fillers are good candidates for the improvement of polymer thermal conductivity. Indeed, silica (SiO_2) particles, and generally most metal oxide fillers, exhibit a low thermal conductivity, which hinder avoid their exploitation for thermally conductive polymer composites. However, several ceramic materials, including hexagonal boron nitride, silicon carbide, graphitic materials, etc., gained attention as thermally conductive fillers owed to their high thermal conductivity (~ 10^2 W m^{-1} K^{-1}, Table 2) coupled with high electrical resistivity. [1] The combination of these properties makes the exploitation of thermally conductive ceramic particles interesting in all those applications where electrical insulation is required. The presence of impurities or a low crystallinity results in an additional phonon scattering, thus decreasing the thermal conductivity of ceramic fillers [11]. Thermal conductivity of composites containing ceramic fillers was reported to be affect by the particle thermal conductivity, particle size and size distribution, volume content, mixing methods and filler packing density [1]. Despite carbon-based fillers belong to ceramic fillers, the variety of available carbon allotropes and their peculiar properties will be discussed below, as a different filler family.

Carbon-based fillers

Carbon-based materials, including graphite, carbon black, carbon fiber, carbon nanotubes (CNT), graphene and graphene-related materials (GRM), are currently the best candidates for the improvement of polymer thermal conductivity, considering their intrinsic high thermal conductivity (theoretically up to ~ 6000 W m^{-1} K^{-1} for suspended graphene) and lightweight (if compared with the other thermally conductive particles) [1, 16]. However, as for metallic particles, the exploitation of carbon-based fillers in polymer matrix leads to electrically conductive materials, thus preventing their use when electrical insulation is required. In carbon based materials, heat transfer mainly occurs by phonons, even if the presence of π-conjugation results in a contribution of electrons to the thermal conductivity. As for ceramic fillers, to which carbon-based fillers belong, the presence of defects, *i.e.* vacancies, grain boundaries, heteroatoms, etc., affects the intrinsic thermal conductivity of carbon-based materials [16].

Carbon fibers (CF) are one-dimensional fillers with high thermal conductivity (up to ~ 1000 W m^{-1} K^{-1} for fiber produced by mesophase pitch) along the longitudinal direction, whereas lower values where measured along the transvers direction (~ 10 ÷ 110 W m^{-1} K^{-1}), thus leading to an anisotropic thermal conductivity in aligned polymer/CF nanocomposites [1, 11].

Graphite is recognized as one of the best conductive fillers because of its high thermal conductivity, low cost and fair dispersability in polymer matrices [1]. Graphite is constituted by a stack of graphene layers, each of which was reported to have a theoretical thermal conductivity up to 5300 W m^{-1} K^{-1} (theoretical value for free suspended graphene). However, the in plane thermal conductivity of bulk graphite was reported to be in the range 100 ÷ 400 W m^{-1} K^{-1}, whereas the cross-plane thermal conductivity was reported to be ~ 6 W m^{-1} K^{-1} at room temperature [24].

Carbon nanotubes are one-dimensional fillers with diameter in the order of some nanometers. Theoretical simulations and calculations reported a thermal conductivity up to 6000 W m^{-1} K^{-1}. However, the thermal conductivity of CNT depends on many parameters such as the aspect ratio (*i.e.* the ratio between length and diameter), the number of walls, the atomic arrangement (*i.e.* how graphite sheets are rolled), the number of structural defects as well as the presence of impurities, etc. [1]. The extremely high thermal conductivity of carbon nanotubes attracted researchers for their exploitation in the preparation of thermally conductive polymer nanocomposites [1, 25, 26]. The main drawback of CNT is

their poor dispersability [16], which requires high energy processes or chemical functionalization to be improved, limiting, at the moment, their use for commercial purposes.

Finally, graphene is a single-atom-thick sheet of hexagonally arranged, sp^2-bonded carbon atoms freely suspended or adhered on a foreign substrate [27]. It was isolated for the first time in 2004 [28] and gain huge worldwide attention thanks to its electronic, thermal and mechanical properties [29-31]. Graphene as thermally conductive material will be thoroughly in the following section.

Table 2. Thermal conductivities of some thermally conductive fillers [1, 11, 16, 32]

Material	**Thermal conductivity at 25°C** **$W\ m^{-1}\ K^{-1}$**
Aluminum	204
Copper	483
Nickel	158
Silver	450
Gold	345
Hexagonal boron nitride (h-BN)	185 ÷ 300
Silicon nitride (β-Si_3N_4)	103 ÷ 200
Silicon carbide (SiC)	120 ÷ 270
Aluminum oxide (Al_2O_3)	20 ÷ 30
Berillium oxide (BeO)	260
Diamond	2000
Carbon nanotubes (CNT)	2000 ÷ 6000
Graphite	100 ÷ 400 (in-plane)
Carbon Black (CB)	6 ÷ 174
Pitch-based Carbon Fibers	530 ÷ 1100 (along the axis)
Graphene	2000 ÷ 6000

1.3 Graphene

Since its isolation from bulk graphite in the early 2004 [28], graphene attracted the interest of worldwide scientists. Graphene is defined as a single-atom-thick sheet of hexagonally arranged, sp^2-bonded carbon atoms that is not an integral part of a carbon material, but is freely suspended or adhered on a foreign substrate [27]. While the thickness is well defined, the lateral dimension of graphene can vary from several nanometers to the macroscale. The peculiar structure of graphene directly affects the mechanical (1.0 TPa and 130 GPa for the Young's modulus and the intrinsic strength, respectively), electrical and thermal properties [29-31].

1.3.1 Graphene-related materials

The growing demand for graphene pushed the research to the development of many synthesis techniques for large-scale production of graphene coupled with cost-containment. Method for large scale production, including liquid-phase exfoliation, graphite oxidation, followed by thermal expansion and thermal or chemical reduction, electrochemical exfoliation of graphite, will be more thoroughly discussed in section 1.4.3. However, often the yield of graphene with such techniques is very limited and materials constituted by more than one graphene layer are typically available. In order to try to rationalize naming of different two-dimensional carbon forms, Bianco *et al.* [27] recently published a guideline. This section will be referred to that guideline in order clarify the different terms and acronyms that will be used in this thesis.

Graphene-related materials (GRM): intended as all those 2D materials that contain the word graphene.

Few-layer graphene (FLG): a 2D material consisting of a small number (between 2 and about 5) of well defined, stacked graphene layers of extended lateral dimension. Considering a thickness of ~ 0.34 nm for graphene [33], FLG should not exceed a thickness of ~ 1.7 nm.

Multi-layer graphene (MLG): like few-layer graphene but with layer amount between 2 and 20, *i.e.* a maximum expected thickness of about 3.4 nm.

Graphite nanoplatelets or *graphite nanoplates* (GNP): a 2D graphitic material (ABA or ABCA stacked) having a thickness and/or lateral size less than 100 nm.

Graphene oxide (GO): graphene which present an extensive oxidation of the basal plane. GO is a monolayer material and has to be distinguish from few-layer (FLGO) or multi-layer graphene oxide (MLGO), which are obtained from exfoliation of graphite oxide.

Reduced graphene oxide (rGO): graphene oxide, including few- and multi-layer graphene oxide, which underwent a reduction process by thermal, chemical, photo-thermal, etc. methods, or a combination of them, to reduce its oxygen content.

Sometimes, one of these definitions can overlap with another one, such as rGO and MLG or GNP when an extensively reduction of the oxygen content was applied to FLGO or MLGO.

1.3.2 Thermal conductivity of graphene

Among the different extraordinary properties of graphene, its extremely high thermal conductivity attracted the interest of scientists for use as heat exchanger material, alone or compounded in polymer matrices. The thermal conductivity of graphene was measured and calculated in the range ~ 2000 ÷ 5800 W m^{-1} K^{-1} for suspended graphene [30, 34], whereas a value of ~ 600 W m^{-1} K^{-1} was reported for graphene supported by a substrate like SiO_2 [35, 36]. This difference can be explained by an increased phonon scattering, in supported graphene, owed to the coupling of the out-of plane acoustic phonons (ZA) to the substrate or to other graphene layers [35]. Furthermore, it is worth noting that the upper limit in graphene thermal conductivity is achieved by isotopically purified samples with large grain size, whereas the lower limit corresponds to samples with smaller grain size [24, 37].

In graphene, heat is transferred by phonons and electrons. However, the main contribution to the thermal conductivity was related to phonon vibrations, considering that experimental studies reported an electronic contribute $\lambda_e \approx 11 \div 300$ W m^{-1} K^{-1} at room temperature, *i.e.* between ~ 0.3 and 10 % of the overall thermal conductivity [13, 14, 38]. Thus, the thermal conductivity of graphene can be explained mainly by the high phonon mean free path, $l \approx 775$ nm, reported for suspended graphene near room temperature [38].

The thermal conductivity in graphene is affected by the grain size and the presence of defects (vacancies, grain boundaries, dislocations, etc.) or heteroatoms. Nika *et al.* [39] reported that the thermal conductivity measure for

flake width of 9 μm was about 1.8 times that measured for flake width of 3 μm, due to a more pronounced effect of phonon scattering at grain edges for smaller graphene samples. Furthermore, the presence of defects in graphene, studied by molecular dynamic simulations, was reported to dramatically affect the thermal conductivity of pristine graphene, with up to 90% decrease in the thermal conductivity, with respect to the non-defective graphene [40, 41]. Feng *et al.* [40] reported that the presence of 1.1% ^{13}C decreased the thermal conductivity by about 15 %, whereas reduction by about 90 ÷ 95% were observed for 1.1% of stone-wales defects (consisting in the rotation of one C-C bonds by 90° with the consequent transformation of four hexagons into two pentagons and two heptagons), double vacancies (formed by the coalescence of two point vacancy or by the elimination of two bonding atoms with the formation of one octagon and two pentagons instead of four hexagons), and monovacancy (missing of one carbon atoms in the lattice resulting in the formation of a nine-membered and five-membered ring). The presence of heteroatoms, was reported to reduce the thermal conductivity of graphene with a reduction by about 70 and 60% whit 1% concentration of Boron and Nitrogen atoms, respectively [42, 43]. Very recently, Malekpour *et al.* [44] created defects on graphene by electron beam irradiation and observed experimentally that higher defect concentration resulted in a low thermal conductivity of graphene (~ 400 W m^{-1} K^{-1} with a density of defect ~ 20 10^{10} cm^{-2}).

The thermal conductivity results above-reported are related to graphene, intended as single-atom-thick sheet. However, in many practical applications, such as in polymer nanocomposites, graphene-related materials are used. For these materials, it was reported that thermal conductivity on suspended few-layer graphene decreases as the number of layers (n) increases, approaching the limit of bulk graphite, especially for $n \geq 4$. This reduction was related to the changes in the phonon dispersion and to more phase-space states becoming available for phonon scattering [33]. Furthermore, in a recent experimental research, Tortello *et al.* [35] reported an increase in the heat transfer properties of rGO after thermal annealing at 1700 °C in vacuum, which was responsible of a decrease in the nanoflake defectiveness.

1.3.3 Synthesis of graphene-related materials

The growing demand for graphene pushed the research to the development of many synthesis techniques. However, for many of these techniques, including mechanical cleavage of graphite [28], epitaxial growth on SiC [45], chemical

vapor deposition [46-48] and liquid phase exfoliation [49, 50], the industrial scale up of graphene, still remain highly challenging [51]. On the other hand, large-scale preparation techniques, such as chemical reduction of graphene oxide [52, 53], thermal exfoliation and reduction of GO [54], liquid phase exfoliation of graphite [50, 55], electrochemical exfoliation of graphite [56] and other techniques [57] often lead to relatively low quality flakes, in terms of average thickness and distribution as well as in chemical defectiveness of the sp^2 structure. [51]. Some of the above-mentioned techniques will be further described in this section.

Mechanical cleavage of graphite

Graphene production by mechanical cleavage of graphite is the method that was used to isolate graphene for the first time in 2004 [28]. It consists on rubbing a fresh surface of graphite against another surface, to which a wide variety of flakes remains attached. Authors reported that among this flakes they always found some single layers [58]. This technique can lead to graphene with a large crystallite size depending on the used graphite, but the low yield limits its application only for research purpose [57].

Chemical vapor deposition

Chemical vapor deposition (CVD) is the most promising synthesis technique for the production of graphene. In CVD, carbon precursors are adsorbed on the catalyst surface, where they decompose to form hydrocarbon intermediate species, which subsequently reacts to form graphene [59]. Many parameters affect graphene formation, such as precursors (methane, acetylene, isopropanol, hexane, etc), catalyst geometry, and composition (Cu, Ni, Pt, alloys Cu-Ni, etc), reaction time, temperature, precursor flux and experimental set-up [59, 60]. Despite the possibility of exploit many catalysts, usually the largest area and highest quality graphene foils are growth on copper [57]. In the last years, scientist synthetized graphene on dielectric substrates, like sapphire, silica, SiC [60, 61], sometimes aided by the presence of oxygen or carbon dioxide. Avoiding the need for metal catalyst, in these processes post-growth transfer is not required, reducing the risk of damage graphene. However, it is noteworthy that CVD is an expensive process, owed to large energy consumption and to the need of removing the underlying metal (when process is performed in presence of metal catalyst). Furthermore, CVD, being not affordable for large-scale production, is typically exploited for the synthesis of graphene for nanoelectronics, transparent conductive layers,

sensors, etc. where the need for high amount of high quality graphene is limited [57].

Liquid-phase exfoliation

Liquid-phase exfoliation (LPE) of graphite consists in splitting graphite into individual platelets with the aid of sonication into a solvent [49, 50, 55]. Different solvents can be employed, typically non-aqueous (*i.e.* N-Methyl-2-pyrrolidone, NMP), but water solutions containing a surfactant were also used. The main requirements is that the solvent must have a surface tension that allows to increase the total area of graphite crystallites [57]. This technique allows for the production of a wide distribution of graphene-related materials, including high quality graphene, which concentration can be further enriched by centrifugation, with a graphene concentration in NMP up to 1.2 mg mL^{-1} [49]. Respect to the above reported techniques, LPE allows the production of graphene with a lower energy consumption, even if the drawback is the use of organic solvents or surfactant that have to be recycled or disposed. On the other hand, LPE can lead to kilos scale production of graphene or GRM, thus making possible its exploitation in polymer nanocomposites.

Graphite oxidation or intercalation

Another method for the production of graphene and GRM is the chemical modification of graphite through oxidation or intercalation with small molecules, which help for separation of graphene layers in the graphite [57]. These two synthesis techniques usually moves from the oxidation method reported by Hummers in 1958 [62] or from the intercalation of graphite by sulfur compounds described by Hofmann in 1938 [63]. However, it is worth noting that after oxidation or intercalation, the obtained materials need to be further treated in order to separate graphene layers. The principal techniques to separate graphene layers are:

- LPE: as above described, but using graphite oxide or intercalated compound instead of pristine graphite;
- Thermal exfoliation: this method requires a rapid heating (> 2000 °C min^{-1}) up to ~ 1050 °C in inert atmosphere, leading to a splitting of graphite oxide into individual sheets through evolution of CO_2 [53, 54];
- Chemical exfoliation: recently reported by Lin *et al.* [64] it consists in the intercalation of graphite with CrO_3 obtaining CrO_3-GIC, then

CrO_3-GIC was immersed in 30% H_2O_2 solution which reacts with Cr leading to the expansion of GIC.

These methods allow to the production of large amount of GRM, including MLG and GNP, with a variable degree of oxidation and defectiveness, which are typically available on the market in large quantities. Owed to the typically high content of oxygen species and defect in GRM prepared by this technique, these materials are usually further treated to reduce the oxidation, by thermal or chemical reduction [65-67], or the defectiveness, by thermal treatment at high temperatures (> 1400 °C) [68, 69].

Electrochemical exfoliation

Electrochemical exfoliation of graphite consists in a two-electrode system, where platinum typically is the counter electrode while graphite flake is the working electrode [70], both dipped in an electrolyte. The application of a voltage (typically 10 V) leads to an initial intercalation of electrolyte ions between graphene layers. Keeping the applied voltage constant, graphite flakes expand, dissociate and disperse into the solution [71]. This synthesis technique is highly flexible: indeed, exfoliation can occur with either cathodic or anodic potentials. Anodic exfoliation is mainly performed in aqueous electrolytes (ionic liquids, acids or inorganic salts), and is less time demanding (~ 1 h) but typically leads to the functionalization with oxygen groups. On the other hand, cathodic exfoliation is mostly based on the use of lithium or alkylammonium salts dissolved in organic solvents (*i.e.* propylene carbonate, dymethyl sulfozxide, etc.) and no oxidation occurs owed to the absence of oxidizing conditions. However, the drawback of cathodic exfoliation is that can produce only few-layer graphene, which need to be further processed by other methods to obtain graphene [56, 72-75]. The high flexibility of such process, coupled with the possibility to obtain good quality GRM, makes it a good candidate for the production of large amount of graphene and GRM.

The production of high quality graphene requires the use of synthesis techniques that are not suitable for large scale production, intended as tons of materials per year. Furthermore, the graphene in yield in those processes, which can easily allow for a large scale production, is typically limited to a few percentage, thus leading to a costly product that could be employed only for niche applications. For these reasons, often in the market are sold graphene-related materials, especially in the form of multi-layer graphene or graphite nanoplatelets,

which are available in large quantities but limiting the material cost, which is fundamental for the inclusion in polymeric materials.

1.4 Polymer/graphene-related materials nanocomposites

The isolation of graphene, and the development of many synthesis techniques for the large-scale production of graphene-related materials, pushed research to exploit this material family in polymer matrix, in order to improve specific properties, *i.e.* mechanical, optical, electrical, thermal, permeability, etc. [2, 7, 11, 76, 77]. The interest in using GRM as filler in polymer matrix, instead of graphite, is related to the higher specific interface typical of nanoparticles. In fact, it was reported that the use of nanofillers, instead of conventional microfillers, led to lower percolation threshold, larger amount of particles per particle volume (10^6 to 10^8 particles μm^{-3}), shorter distance between particles, particle-particle interactions occurring at low-volume fractions, extensive interfacial area per particle volume, and comparable size scales among nanoparticles and the relaxation volume of polymer chains [78].

The preparation of high quality polymer nanocomposites exploiting graphene-related materials requires high dispersion and distribution degree of the flakes and a good interfacial interaction between the matrix and the nanoflakes, similarly to the case of polymer/CNT nanocomposites [1, 25, 26, 79]. Selecting the proper processing method, and optimizing mixing parameters, would results in higher dispersion and distribution degree of nanoparticles in the polymer matrix. Furthermore, the use of functionalized graphene, either covalent and non-covalent, can be a good solution for the preparation of high-performance polymer nanocomposites [76], achieving high dispersion and particle/polymer interaction. Covalent functionalization can be highly efficient for the improvement of mechanical properties of polymer nanocomposites, owed to an improved stress transfer between polymer matrix and reinforcing particles. However, chemical bonding of organic moieties to an sp^2 layer inevitably creates defects (sp^3 carbons), drastically affecting electronic, optical and thermal properties of graphene [41, 76]. On the other hand, non-covalent functionalization has a less severe effect on graphene properties, but the reversible adsorption and the weaker interfacial interaction limit its applications in polymer nanocomposites [76].

The organization of nanoparticles in a polymer matrix has to be properly controlled to obtain high performance polymer nanocomposites. Dispersion and distribution of GRM in polymer matrices could be obtained through different

techniques, such as solution mixing, melt mixing, and *in-situ* polymerization, which will be described below.

1.4.1 Preparation methods

Solution mixing

Solution mixing is a simple route for GRM dispersion and distribution in polymer matrix. Polymer solution (or suspension) and GRM suspension, with the same or a miscible solvent with that used for polymer matrix, are mixed together with the aid of agitation, shear mixing or ultrasonication. This will help with homogeneous dispersion of GRM. Finally, to separate the nanocomposite from the solvent, different procedure, such as solvent evaporation, precipitation in a non-solvent, filtration, etc., can be used [1, 76]. The entropy gained by the desorption of solvent molecules compensates the reduction in conformational entropy of intercalated polymer chains [80]. Solution mixing, potentially, could be the most suitable method to obtain optimal dispersion of nanoflakes [7, 76]. However, such high dispersion can be obtained only by the exploitation of high energy consuming treatments, such as ultrasonication, or the use of solvents that require to be recycled or disposed. Many polymer/GRM nanocomposites were prepared by solution mixing method, including polystyrene (PS) and poly(methyl methacrylate) (PMMA)/GO [81], polyamide 6 (PA6)/rGO [82], epoxy containing GO and rGO [83], poly(propylene carbonate) (PPC)/GO [84], high density polyethylene (HDPE)/rGO [85], poly(vinylidene fluoride-co-hexafluoropropylene) (PVDF-HFP)/rGO [86], silicone [87], polypropylene/GNP [88]. Furthermore, by solution mixing polymer nanocomposites containing functionalized GRM were prepared, including PA6/f-rGO [89], epoxy/f-GNP [90], PVDF/f-rGO [91], PS/f-rGO [92]. However, the extensive use of organic solvents to dissolve polymers typically limits the exploitation of this technique for industrial applications.

Melt mixing

Melt mixing is a versatile and cost-effective process, in which nanocomposites are quickly prepared without the aid of a solvent [1, 7, 76, 80]. It simply consists in mixing molten polymer with the filler through the application of shear and/or elongational forces. Therefore, the main parameters that affect melt mixing are temperature (which should be high enough to produce a fluid polymer, however avoiding its thermo-oxidative degradation), shear rate (which directly affect the shear forces in the extrusion process), and processing time (*i.e.* the time for which

polymer and nanoparticles are mixed). The main drawback of this method is in the difficulty to achieve efficient contact at the nanoscale between the polymer and the matrix, thus often leading to lower dispersion degree compared to solvent mixing processes. Furthermore, heating and locally high stresses can affect the stability of components, especially for the polymer chains, flake sizes, and slight reduction of graphene oxide layers [7]. Given the high interest for industrial applications, reasonably successful methods were developed for the preparation of graphene-related materials nanocomposites based on different thermoplastic polymers.

Gao *et al.* [93], prepared poly(lactic acid) (PLA)/GNP nanocomposites via melt mixing in extruder for electronic packaging and observed by electron microscopy a satisfactory distribution of nanoparticles up to 7 and 10 wt.% when high and low aspect ratio GNP, respectively, were used. Furthermore, these authors measured the lateral size of nanoparticles and observed a reduction by a third and by a half for small and high aspect ratio GNP, respectively, after melt mixing, as a consequence of shear applied on the particles. On the other hand, no changes were observed in the nanoflake thicknesses upon melt mixing. Vallés *et al.* [94] washed GO with a base to remove oxidative debris, obtaining bwGO, and observed a homogeneous distribution up to 1 wt.% GO/bwGO in PMMA. However, increasing further the nanoparticle content up to 10 wt.% led to the formation of aggregates, without the organization of nanoflakes in an electrical percolating network, for both GO and bwGO, despite the elimination of oxidized debris in base-washed GO. Ratzsch *et al.* [95] added thermally reduced graphene, to ethylene-vinyl acetate (EVA), with different vinyl acetate contents, and obtained a rheological percolation threshold of ~ 2.5 vol.% (~ 5 wt.%). However, at this filler content, the dispersion of flakes was poor, with the presence of a huge amount of aggregates. Dul *et al.* [96] prepared acrylonitrile-butadiene-styrene (ABS)/GNP nanocomposites for 3D printing and found that for GNP content higher than 4 wt.% the viscosity of the nanocomposite was too high for 3D printing. Han *et al.* [97] prepared PS nanocomposites containing GO reduced at different temperatures and reported by morphological studies that upon increasing reduction temperature the nanoflake distribution increases owed to a favorable π-π interaction between PS and graphene layers. El Achaby *et al.* [98] prepared polypropylene (PP) nanocomposites containing graphite nanoplatelets and obtained a poor dispersion of nanoparticles with large presence of aggregates, thus indicating a poor interaction between the polymer matrix and the GNP.

In-situ polymerization

In-situ polymerization, which sometimes is referred to as intercalation polymerization, involves the dispersion of GRM in a monomer, or an oligomer, followed by polymerization in presence of the same GRM. This method showed high dispersion ability, which is often better than for the other mixing methods [1, 76, 99, 100]. Furthermore, *in-situ* polymerization can be performed either in solution and in melt, and typically occurs by heating and/or by adding a proper catalyst to the system. The advantage of graphene-related materials is that they can be functionalized in order to act as catalyst or as polymerization initiator, thus enable covalent bonding between GRM and polymer. The exploitation of GRM as catalyst/initiator avoids the need of further purification steps to remove strong acid initiators and/or metal particle catalysts, as reported in a recent review [101]. As for the above mentioned methods, many polymer-based nanocomposites containing GRM were prepared by this technique.

Xu *et al.* [102] prepared PA6/rGO nanocomposites by in-situ melt polymerization of caprolactam in the presence of GO, taking advantage of the condensation reaction to directly graft polyamide chains onto GO surface, which is consequently reduced. This led to high distribution and dispersion degree of nanoflakes, even if they do not reported any data on nanocomposites with GO content higher than 0.5 wt.%. Furthermore, they observed that increasing the concentration of nanoparticles resulted in a decrease of PA6 molecular weight (~ 85% reduction with 10 wt.% content of GO). Yang *et al.* [103] prepared PLA nanocomposites by *in-situ* melt ring opening polymerization of L-Lactide, in presence of thermally reduced graphene oxide, exploiting the hydroxyl groups on the rGO surface as initiator. The authors reported a homogenous dispersion of rGO sheets on composites containing up to 2 wt.% rGO, whereas in samples prepared by simple melt blending PLA and rGO, nanoparticle aggregates were visible even in nanocomposites containing 1 wt.% of rGO. Wang *et al.* [104] prepared PMMA nanocomposites in solution by *in-situ* polymerization of methyl methacrylate in presence of chemically reduced graphene oxide and they observed the presence of rGO aggregates at contents $\geq$ 4 wt.%. This poor dispersability was related to the limited chemical functionalization of rGO, which resulted in a poor wettability of nanoflake surface. Indeed, after further functionalization of rGO with alcoxysilane molecules the same authors observed higher dispersion degree up to 10 wt.% of functionalized rGO. Noh *et al.* [105] prepared PBT nanocomposites by powder mixing cyclic butylene terephthalate oligomers and different GRM (GNP, GO and rGO) followed by polymerization of oligomers

into polymer during compression molding of the powder mixture at high temperature. They evaluated the distribution of nanoparticles in term of distance between nanoflakes and observed higher particle distribution when GO or chemically reduced GO (up to 20 wt.% filler content) were exploited, owed to a high interaction between polymer and oxidized groups or phenyl groups. Liu *et al*. [106] functionalized GO with alcoxysilane molecules, then they *in-situ* polymerized poly(amic acid) which was further imidized to obtained polyimide (PI)/GO nanocomposites and observed the presence of nanoflake aggregates for content $\geq$ 2 wt.%, whereas good dispersion degree was observed with lower content. Finally, Shamsi *et al.* [107] prepared PU/GO nanocomposites by in-situ polymerization of polyurethane and evaluated a good dispersion of nanoflakes, with a good interaction with the polymer matrix, for GO content $\approx$ 1 wt.%, whereas when the nanoparticle content was increased up to 2 wt.% the presence of aggregates with poor interaction with the polymer matrix was observed.

Beside these three main synthesis methods, several other technologies to prepare polymer/GRM nanocomposites were reported in the literature, including Latex mixing, electropolymerization, solid-state shear pulverization [76, 99]. Furthermore, all the described methods can be combined (*i.e.* solution mixing and melt mixing, solution mixing and *in-situ* polymerization, etc.) in order to exploit the advantages proper of each process.

1.4.2 Properties of polymer/GRM nanocomposites

Since its isolation from graphite, graphene and graphene-related materials gained significant attention for their exploitation in polymer matrices, in particular for mechanical, electrical, and thermal properties. In the present section, properties of polymer/GRM nanocomposites will be briefly described.

Electrical conductivity

Polymers are well known insulating materials, with typical electrical conductivities in the order of ~ 10^{-12} – 10^{-14} S m^{-1}. On the other hand, the electrical conductivity of suspended graphene is estimated to be ~ $1 \cdot 10^{8}$ S m^{-1} [28]. This high electrical conductivity value is obviously referred to pristine graphene, whereas, as above discussed, in polymers are typically exploited graphene-related materials. Excluding graphene oxide and graphite oxide, which are insulating materials [65], for FLG, MLG, GNP and rGO, electrical properties could be considered in between those of pristine graphene and graphite (~ $2 \cdot 10^{5}$

S m^{-1}, parallel to the surface, and ~ $3 \cdot 10^2$ S m^{-1}, perpendicular to the graphite surface [108]), depending on different parameters including nanoparticle aspect ratio and presence of oxidized species. The electrical conduction in polymer composites and nanocomposites typically occurs above a critical filler content, namely electrical percolation threshold (φ_c), at which the formation of a continuous network of nanoparticles is observed. At φ_c a sharp increase (several orders of magnitude) in the electrical conductivity of polymer nanocomposites is observed.

Some electrical conductivity results for polymer/GRM nanocomposites are summarized in Table 3, in which the properties of nanocomposites containing different GRM types, prepared by different methods and based on different polymer matrices are compared. The minimum percolation threshold value observed for polymer/GRM nanocomposites is in the order of some tenths of vol.% but values up to 8.0 vol.% were reported in literature, reflecting very different dispersion degrees and particles aspect ratios. These φ_c are higher than the minimum value reported for CNT nanocomposites (φ_c < 0.1 vol.%) [109], owed to the different shape of CNT and GRM. Observing all the results, it may appear that the preparation process alone and the polymer matrix generally play a marginal role on the electrical conductivity enhancement. In fact, φ_c in the order of some tenths of vol.% were measured for both thermoplastic and thermoset nanocomposites prepared by different processes, including melt mixing, three-roll mill, solution mixing, in-situ polymerization. However, Chandrasekaran *et al.* [109] showed that the exploitation of the proper mixing process drastically affected the electrical conductivity of epoxy/GNP nanocomposites. Indeed, at ~ 0.5 vol.% GNP content the electrical conductivity of nanocomposites prepared by three-roll mill or the combination of sonication and high speed shear mixing resulted in $2 \cdot 10^{-3}$ and $1 \cdot 10^{-6}$ S m^{-1}, respectively.

To improve the dispersion of nanocomposites, often researchers resort to functionalization of GRM nanoflakes, aiming to higher dispersion and interaction between the polymer matrix and the filler. Indeed, Wang *et al*. [104] prepared PMMA based nanocomposites containing functionalized FLG and measured electrical conductivity up to 1700 S m^{-1} with about 5.6 vol.% FLG content, which was higher than results obtained for nanocomposites containing 10 wt.% of the same FLG slightly oxidized but not functionalized (~ 80 S m^{-1}). This was explained by the higher affinity of functionalized FLG with the matrix, and the formation of covalent bonding, which led to high dispersion degree, *i.e.* in a higher separation of the nanoflakes, thus leading to a less dense percolation

network. Yang *et al.* [103] prepared PLA/RGO nanocomposites using thermally reduced GO as initiator for PLA polymerization and obtained an electrical conductivity value $\sigma \approx 1.6 \cdot 10^{-2}$ S m^{-1} at 1,1 vol.% RGO content.

Nanoparticle aspect ratio and defectiveness were reported to affect the electrical conductivity of polymer nanocomposites in terms of both percolation threshold and maximum electrical conductivity value. Indeed, high aspect ratio and less defective nanoflakes resulted in lower percolation threshold and higher electrical conductivity maximum, respectively, in both thermoset and thermoplastic materials [93, 110]. The exploitation of low defective and large FLG and MLG is, thus, mandatory for the preparation of high electrically conductive polymer/GRM nanocomposites.

Table 3. Electrical conductivity of some polymer/GRM nanocomposites

Matrix	Filler	Preparation	Properties			Ref.
			φ (vol.%)	σ (S m^{-1})	φ_c (vol.%)	
Epoxy	GNP	Three-roll mill	0.5	$2 \cdot 10^{-3}$	0.3	[109]
		Sonication + High speed shear mixing	0.5	$1 \cdot 10^{-6}$	-	
PI	Functionalized FLG	Solution intercalation	2.0	$3 \cdot 10^{-2}$	1.3	[111]
Polyester	GO	Solution mixing + transesterification	1.0	0.3	0.2	[112]
PLA	large-GNP	Melt mixing	9.0	0.1	5	[93]
	small-GNP		9.0	0.1	8	
PU	MLG	Melt mixing	3.0	$6 \cdot 10^{-2}$	0.6	[113]
PMMA	Oxidized FLG	In-situ polymerization, solvent	5.6	80		[104]
	Functionalized FLG		0.8	$1.6 \cdot 10^{-2}$		
			5.6	1700		
PLA	rGO	In-situ polymerization, melt	1.1	$1.6 \cdot 10^{-2}$	0.7	[103]
Epoxy	GNP	Three-roll mill	2.6	$2 \cdot 10^{-2}$	0.5	[110]

Thermal conductivity

Thermally conductive polymer nanocomposites are of great interest for those applications where corrosion resistance, ease of processability and lightweight are required. Graphene, owing to its outstanding thermal conductivity, is one of the main candidates for this purpose. The graph reported in Figure 1 shows the normalized thermal conductivity, *i.e.* the ratio between the thermal conductivity of the nanocomposite and that of the pristine polymer, for some works, reported in literature, on nanocomposites containing CNT or GRM. Compared to polymer nanocomposites based on carbon nanotubes [1], the use of graphene-related materials appears to be more efficient in terms of thermal conductivity increase, as summarized in Figure 1, thus proving the high interest of exploiting GRM for thermal applications. Indeed, to double the thermal conductivity of the polymer matrix are required on average ~ 5 and 1 vol.% of CNT and GRM, respectively. Furthermore, for a given nanoparticle content GRM demonstrated to lead to higher thermal conductivity than CNT, *e.g.* at 10 vol.% content thermal conductivity values, for nanocomposites containing CNT and GRM, are on average three and ten times, respectively, higher than that of the polymer matrix.

For both CNT- and GRM-based nanocomposites, an obvious scatter of data is observed, due to the different preparation procedure, GRM and CNT types, polymer type, measuring technique, etc. Furthermore, many parameters are recognized to play a crucial role in the improvement of thermal conductivity, including interfacial thermal resistance, nanoparticle quality, organization and alignment [10, 11, 99, 114], thus explaining the limited thermal conductivity enhancement, despite the nominal intrinsically high thermal conductivity of graphene related materials, and the large scattering of values at a given nanoparticle content, as observed in Figure 1.

Shahil *et al.* [115], exploited the liquid phase exfoliation method to prepare different GRM mixtures, constituted mainly by few-layer and multi-layer graphene. Later they added these mixture to epoxy resin (GRM content ~ 0.2 – 10 vol.%), which was subsequently cured and heated in vacuum, and measured a large increase in the thermal conductivity of these materials, with $\lambda/\lambda_{matrix} \approx 23$, with 10 vol.% of the optimal GRM mixture (~ 10-15 % FLG with number of layers, n, ≤ 2, ~ 50 % MLG with $n \leq 5$). This huge enhancement was assigned to (a) the high intrinsic thermal conductivity of GRM, (b) the low Kapitza resistance at the graphene/matrix interface, (c) the geometrical shape of GRM, *i.e.* their aspect ratio, (d) the flexibility of flakes with $n \leq 2$ and (e) the optimum mix of

graphene and MLG with different thicknesses and lateral size. The need of GRM mixture was explained by the high flexibility of graphene and bi-layer graphene, which act as thermal links, and the lower degradation, due to phonon-boundary scattering, characteristic of the thicker nanoflakes. Furthermore, in their work, their observed that thermal conductivity increased linearly with GRM mix content up to 10 vol.%, without any percolation threshold, whereas further increasing the amount of nanoparticles resulted in the formation of inhomogeneous inclusions. Similar enhancements were observed by Teng *et al.* [116] for epoxy nanocomposites containing multi-layer graphene, prepared by a modified hummers method, and the same MLG non-covalently functionalized. In their work, MLG was functionalized with modified pyrene molecules (exploiting π-π interactions) able to improve the MLG dispersion and, at the same time, to covalently bond the functional group of pyrene to the epoxy matrix, thus providing a more efficient heat transfer. The functionalization, with the higher dispersion and the bonding of pyrene with the epoxy matrix, resulted in high thermal conductivity enhancement, with ~ 9.5- and 8-times improvement when functionalized and pristine MLG, respectively, were used. The two works above described, demonstrated that it is possible to achieve high thermal conductivity by selecting the proper filler and by optimizing dispersion and interaction between polymer and nanoparticles. However, both the works were related to thermoset nanocomposites, whereas lower values were obtained with thermoplastic matrices for which typically lower enhancements were reported, *e.g.* Ding *et al.* [117] reported a doubling in the thermal conductivity of PA6 nanocomposites with about 10 vol.% RGO content.

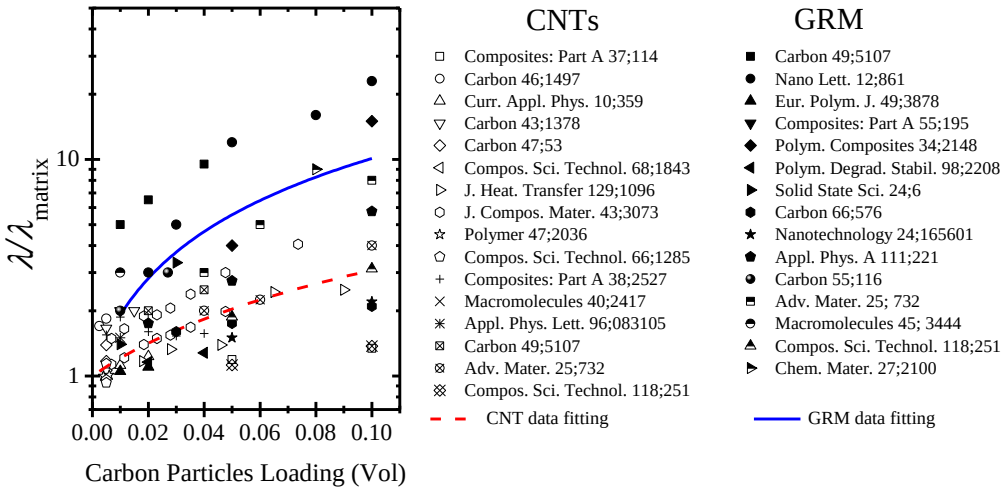

Figure 1. Normalized thermal conductivity (λ) data for CNT or GRM polymer nanocomposites as function of volume carbon particle loading. Data fitting, reported as a guide for the eye, was performed by calculating the average value at every loading then applying a linear fit. Data derived from cited references: for GRM [109, 111, 112, 115-126]

The interfacial thermal resistance, also referred to as Kapitza resistance [127] from the name of the researcher who discovered a temperature discontinuity at the metal/liquid interface, is known to play a key role in the thermal conductivity of polymer nanocomposites [1, 114]. The interfacial thermal resistance between polymer and GRM, in nanocomposites, is ascribed to the phonon scattering at the interface, owed to the mismatch in the vibrational spectra of polymer and graphene. Despite the different shape between GRM and carbon nanotubes, Kapitza resistance for polymer/graphene interfaces was estimated ~ 10^{-8} m^2 K W^{-1} by different simulations [114, 128, 129], as previously observed for polymer/CNT interfaces [1].

The main approach for the reduction of interfacial thermal resistance is the functionalization, either covalent or non-covalent, of graphene (and GRM), trying to increase the coupling between vibrational density of states of graphene and polymer. Wang *et al.* [128] used molecular dynamic simulations to study the thermal transport across graphene/polymer interfaces, where graphene was covalently functionalized with PE chains, and found that increasing the grafting density resulted in a decrease of the interfacial thermal resistance down to ~ 10^{-9} m^2 K W^{-1}. The authors also reported an increase in the thermal conductivity of the graphene/PE nanocomposites, but in their calculations they did not consider the

thermal conductivity reduction upon functionalization of graphene surface, as reported in section 1.4.2. In another work, Konatham and Striolo [130] studied the evolution on thermal transport, across the graphene/octane interfaces, by covalent functionalization of graphene edges, which is expected to have a less detrimental effect on the graphene thermal conductivity, with respect to surface functionalization. In their work, they found a decrease in the Kapitza resistance practically independent on the chain length but slightly dependent on the graphene size, being the lower reduction of the interface thermal resistance observed with bigger graphene sheets. The relationship between functionalization and graphene size was reported by Shen *et al.* [131], which showed that above a critical lateral size (~3 to 4 μm for 1 vol.% of filler, depending on functionalization and filler content) pristine graphene is more efficient in enhancing thermal conductivity of polymer nanocomposites respect to the relevant functionalized graphene. This effect was explained by the higher amount of interfaces when smaller nanoparticles were used, thus indicating an "interface dominant" effect on the thermal conductivity of polymer nanocomposites. On the other hand, non-covalent functionalization with alkyl-pyrene linker molecules [132] was reported to reduce the Kapitza resistance (~ 20 % reduction) in graphene/octane interfaces when C_8-pyrene linker molecules are used, whereas longer or shorter alkyl-pyrene molecules were reported to be ineffective. This behavior was related to the higher alignment of the C_8-pyrene, to the graphene surface, with respect to other alkyl-pyrene molecules.

The effect of graphene and GRM functionalization on the thermal conductivity of their relevant polymer nanocomposites was also evaluated experimentally [133-136]. Ganguli *et al.* [135] reported thermal conductivity values of 4.3 and 5.9 W m^{-1} K^{-1} for epoxy nanocomposites containing 20 wt.% of pristine and functionalized graphite nanoplatelets, respectively, with a lateral size of ~ 3.9 μm. Zhao *et al.* [133] functionalized MLG with epoxide groups for the preparation of epoxy based nanocomposites and obtained thermal conductivity values of 0.65 and 3.14 for nanocomposites containing 10 wt.% of pristine and functionalized MLG, respectively, with an estimated lateral size of ~ 2 μm. A similar trend was observed for Epoxy/GNP nanocomposites, where GNP were reported to have a large lateral size (~ 40 μm), but the thermal conductivity enhancement after GNP functionalization was less pronounced with respect to the previously reported data (1.3 and 1.7 W m^{-1} K^{-1} for nanocomposites containing 30 wt.% of pristine and functionalized GNP, respectively) [136]. Finally, the decoration of rGO with silver nanoparticles was reported to slightly improve the

thermal conductivity of PVA nanocomposites when the filler content was ~ 1 vol.% (~ 0.26 and 0.43 W m^{-1} K^{-1} for PVA/rGO and PVA/Ag-rGO nanocomposites, respectively) [134].

Nanoparticle quality is another parameter recognized to drastically affect the thermal conductivity of polymer/GRM nanocomposites [8, 10]. Nanoparticle quality is a generic term, which typically includes defectiveness and aspect ratio of graphene related materials. In practice, low defectiveness and high aspect ratio indicates high nanoflake quality. The defectiveness was above reported to drastically affect the thermal conductivity of graphene, which is reflected on the thermal conductivity of its relevant polymer nanocomposites. Furthermore, in a systematic study on different graphene nanoplates, Shtein *et al.* [126] reported that, at a given defectiveness, increasing the GNP aspect ratio resulted in a higher thermal conductivity of epoxy nanocomposite containing 0.15 vol.% of GNP (64 and 107 % enhancement in the thermal conductivity of epoxy resin when low and high aspect ratio nanoflakes, respectively, were used). The effect of aspect ratio was also reported by Kumar *et al*. [86] for PVDF-HFP/rGO nanocomposites, where the exploitation of high aspect ratio nanoflakes was reported to provide a higher enhancement on the thermal conductivity of nanocomposites containing ~ 27 wt.% of rGO (15 and 19.5 W m^{-1} K^{-1} when low and high aspect ratio rGO, respectively, were used).

Nanoparticle orientation and organization in the polymer matrix give an important contribution on the thermal conductivity of polymer nanocomposites [10, 11]. Renteria *et al*. [137] studied thermal interface materials and showed that by aligning graphene, in nanocomposites containing 1 wt.% graphene, the thermal conductivity was about 2 times that measured for nanocomposite containing randomly oriented graphene. Lian *et al*. [138] prepared vertically aligned graphene networks in epoxy resin by freeze casting graphene and obtained a thermal conductivity of 2.13 W m^{-1} K^{-1} with 0.92 vol.% content of graphene. The main drawback of orienting graphene is that the thermal conductivity is anisotropic, with the larger amount of heat dissipated in the direction parallel to graphene layer orientation. Furthermore, such nanocomposites cannot be prepared by standard melt processing. However, organization of graphene related materials, in the polymer matrix, in order to improve the contact between nanoflakes is mandatory for enhance thermal conductivity of polymer nanocomposites. Indeed, Eksik *et al*. [139] added chemically reduced graphene oxide (c-rGO) coated poly (methyl methacrylate) microspheres to epoxy resin (with a final content of c-rGO of 1 wt.%) and obtained a 7-fold increase in the thermal conductivity of pure

epoxy resin, whereas the increase was about 3-fold in a traditional epoxy + 1 wt.% c-rGO.

Crystallization

Crystallization of polymers in polymer/GRM nanocomposites is of interest in this thesis as the degree of crystallization as well as the organization of crystals may in principle affect the thermal conductivity of the nanocomposites. Therefore, literature reports describing the effect of GRM on polymer nucleation and growth are briefly discussed in this section.

The presence of graphene-related materials in semi-crystalline polymer matrix was reported to affect the crystallization behavior of polymer chains. In fact, Gao *et al*. [93] prepared PLA nanocomposites containing two GNP types with different aspect ratio and observed that high aspect ratio GNP were more efficient, respect to low aspect ratio GNP, in enhancing the crystallinity of PLA (22 and 14% with large and small GNP, respectively, from ~ 2% measured for pristine PLA) owed to the larger interfacial interaction between the nanofiller and the matrix. The presence of MLG was reported to affect the crystallization peak temperature of thermoplastic polyurethane, with an increase from 29 °C, for neat PU, up to 36 °C for PU + 4 wt.% MLG [113], further confirming the efficiency of GRM as nucleating agents. On the other hand, Ding *et al*. [117] exploited GO as initiator for the *in-situ* polymerization of caprolactame into PA6 and reported a decrease in the crystallization temperature of polyamide as the GO content increased. This can be related to the fact that (a) polymerizing directly onto GO surface could give less mobility to polyamide polymer chains or (b) the molecular weight strongly decreases with GO content. The exploitation of GRM was also reported to affect the nucleation and growth mechanism of polymeric materials evaluated by changes in the Avrami index values extrapolated from fitting of isothermal crystallization experiments on PU [113] and PLA [103] nanocomposites. In PU nanocomposites, the Avrami index decreased from $n \approx 3$ for neat PU, indicating the heterogeneous nucleation of spherulites, down to $n \approx 2$ for PU + 4 wt.% MLG, related to heterogeneous nucleation of axialites, which is an expectable behavior in presence of graphene-related materials.

Mechanical properties and others

The possible exploitation of graphene-related materials for mechanical reinforcement in polymer nanocomposites is suggested by the outstanding mechanical properties measured for pristine graphene. Some results on

mechanical tests on polymer/GRM nanocomposites are summarized in Table 4 where the effect of nanoparticle type and quality, mixing method and polymer matrix on the mechanical properties of some polymer/GRM nanocomposites are compared.

The addition of graphene-related materials in polymer matrices typically leads to an enhancement of the modulus, which has been measured by dynamic-mechanical thermal analysis, tensile or flexural tests. However, the modulus improvement is strongly dependent on both type of nanoparticle/polymer couple as well as loading and preparation method, leading to increases in the range from about 20% with 0.5 wt.% of GNP in epoxy nanocomposites [109] up to 300% with 10 wt.% functionalized FLG in PMMA matrix [104]. It is interesting to observe the enhancement provided by GRM often reaches a maximum (between 1 wt.% and 10 wt.%, depending on the nanoflake type, polymer matrix, etc.), then it stabilizes or it decreases with a further increase in the nanoflake content [93, 109, 110]. The maximum strength of polymer/GRM nanocomposites typically increases with the addition of nanoparticles [91, 93], with a trend similar to that observed for the elastic modulus. On the other hand, the elongation at break typically decreases with the GRM content (up to 90% decrease with 10 wt.% GNP content were reported, [93]). However, in some cases an increase in the elongation at break was observed (~ 110 % increase with 0.42 wt.% functionalized-rGO content), as reported by Maity *et al.* [91] which functionalized rGO with PMMA moieties able to enable the crystallization of the β-form of PVDF.

The scatter of mechanical properties reported evidences dependency of reinforcement on several parameters including nanoparticle dispersion, loanding and aspect ratio, interaction with the polymer matrix. In fact, the decrease in the elastic modulus and nanocomposite strength enhancement, with the nanoflake content, after reaching the maximum improvement, was related to the presence of aggregates, which behave as micro-inclusions. The larger efficiency of high aspect ratio GRM was related to the greater interfacial surface area, leading to an enhanced stress transfer between the polymer matrix and the nanofillers [93]. Obviously, the functionalization of GRM nanoparticles, followed by a covalent bonding with the chains of the polymer matrix, can maximize both the dispersion and the stress transfer at the polymer/GRM interface, resulting in polymer nanocomposites with outstanding mechanical properties [104]. However, the functionalization of GRM, including also the oxidized groups in graphene oxide,

has to be conformed to the polymer matrix in which GRM have to be exploiting, aiming to the maximization of the stress transfer at the interface.

Table 4. Mechanical properties of polymer/GRM nanocomposites

Matrix	Filler	Preparation	Properties			Ref.
			Test	Φ (wt.%)	Results	
Epoxy	GNP	Three-roll mill	DMTA	0.5	$E'/E'_{matrix} \approx 1.2$	[109]
				1	$K_{IC}/ K_{IC,matrix} \approx 1.4$	
PLA	Small-GNP	Melt-mixing	Tensile	10	$E/E_{matrix} \approx 1.3$	[93]
				10	$\varepsilon_b/\varepsilon_{b,matrix} \approx 0.3$	
				5	$\Sigma_{max}/\Sigma_{max,matrix} \approx 1.2$	
	Large-GNP			10	$E/E_{matrix} \approx 1.6$	
				10	$\varepsilon_b/\varepsilon_{b,matrix} \approx 0.1$	
				5	$\Sigma_{max}/\Sigma_{max,matrix} \approx 1.4$	
PMMA	Oxidized FLG	In-situ polymerization, solvent	DMTA	10	$E'/E'_{matrix} \approx 2.1$	[104]
	Functionalized FLG			10	$E'/E'_{matrix} \approx 4.0$	
	Functionalized GNP			10	$E'/E'_{matrix} \approx 1.8$	
PS	rGO	Melt mixing	DMTA	5.0	$E'/E'_{matrix} \approx 2$	[97]
Epoxy	GNP	Three-roll mill	Flexural tests	4.0	$E_{flex}/E_{flex,matrix} \approx 2.5$	[110]
PVDF	Functionalized RGO	Solution mixing	DMTA	0.7	$E'/E'_{matrix} \approx 1.6$	[91]
			Tensile	0.42	$E/E_{matrix} \approx 4.3$ $\varepsilon_b/\varepsilon_{b,matrix} \approx 2.1$ $\Sigma_{max}/\Sigma_{max,matrix} \approx 3.8$	

Beside the above-discussed properties, provided by GRM to polymer matrix, the exploitation of this nanoparticles was also carried out to modify other properties of polymeric materials, including thermal stability [97], combustion behavior [97, 140], gas permeability [141, 142], corrosion resistance [143], etc. As these properties are not relevant to the topic of this thesis, detailed discussion of such properties is beyond the scope of this text.

1.5 Scope and structure of this thesis

The preparation of high-quality polymer nanocomposites containing graphene-related materials is affected by the process used for the dispersion and distribution of nanoparticles in the polymer matrix. At the beginning of this PhD thesis, different processes for the preparation of polymer/GRM nanocomposites were investigated. Conventional melt-mixing in polypropylene matrix was considered as a first option but showed very poor dispersion of GNP and RGO even at 1wt. % nanoparticle loading, clearly owing to the lack of chemical affinity as well as high polymer viscosity. The enhancement of polymer *vs.* GRM affinity in in principle possible by the chemical functionalization of GRM and/or the synthesis of special polymers with chemical structure able to match surface tension or graphene. However, these approaches requires chemical syntheses and modifications which are beyond the scope of this thesis. On the other hand, playing on the viscosity of the media in which GRM are first dispersed may allow for some dispersion improvement while keeping processing simple and easily upscalable for industrial applications. Therefore, dispersion in low molecular weight compounds was addressed, particularly in liquid additives used in polymer compounding. Pre-dispersion into low viscosity media allows in principle to provide high power via sonication or high shear, which is typically not possible in highly viscous polymers. However, just a few polymers need liquid additive in concentration high enough to be used as a carrier for pre-dispersed GRM. As PVC is typically plasticized with 30 to 40 phr of phthalates or similar low molecular weight compounds as liquid plasticizers, this polymer was selected and a few attempts were carried out for dispersion of GNP into different plasticizers. Despite dispersion of GRM into the plasticizers appeared satisfactorily stable and the inclusion in PVC was demonstrated feasible [144], this approach is clearly limited in both the maximum amount of GRM which can be delivered into the final composition and, most importantly, in the type of polymer matrix. Based on these limitations, this approach was not further investigated and attention was focused on the pre-dispersion of GRM into selected polymer precursors (monomers or oligomers) suitable for the polymerization during a reactive melt mixing process. A few polyesters are well known to be polymerized during melt mixing via ring opening polymerization, including PLA from lactide [103, 145] and PBT from cyclic oligomers [146, 147]. While polymerization of lactide requires strict control of polymerization conditions, especially in terms of extremely low moisture content during ring opening polymerization [148], polymerization of

CBT is a quite well-known and robust technology, potentially suitable for large scale applications.

For these reason, the present thesis addressed the design, preparation and characterization of poly (butylene terephthalate) (pCBT) nanocomposites by ring-opening polymerization of cyclic butylene terephthalate in presence of a tin-based catalyst and GRM during melt mixing.

This thesis is structured into eight chapters, in order to clearly show the research developed on *in-situ* polymerized nanocomposites containing graphene-related materials.

In **Chapter 2** is briefly resumed the experimental section, including nanocomposites preparation, as well as nanoparticles and nanocomposites characterization methods.

Chapter 3 is focused on the synthesis and characterization of the graphene-related materials exploited in this thesis. Indeed, in Chapter 1 it was reported that the quality of nanoflakes is one of the main parameters affecting the properties of their relevant nanocomposites. Furthermore, a thoroughly characterization of GRM is mandatory for a better understanding of both nanoparticles intrinsic properties and nanoparticle interaction with the polymer matrix. Nanoflakes, in this chapter, are characterized by means of electron microscopy, Raman spectroscopy, X-ray photoelectron spectroscopy, X-ray diffraction and thermogravimetry. Part of the results about characterization of RGO and RGO_1700 was published in the paper: "Effect of thermal annealing on the heat transfer properties of reduced graphite oxide flakes: A nanoscale characterization via scanning thermal microscopy" *Carbon* 109 (2016) 390-401.

Chapter 4 investigates the effect of graphene-related materials, with different defectiveness and aspect ratio, on the properties of *in-situ* polymerized cyclic butylene terephthalate oligomers into poly (butylene terephthalate). In particular, in a first part the effect of different mixing method is addressed, in order to demonstrate the effectiveness of exploiting *in-situ* polymerization. In the second part, nanoparticle dispersion and distribution, mechanical electrical and thermal properties are studied as a function of the filler type and content. Part of the results reported in this chapter were published in the paper: "Effect of morphology and defectiveness of graphene-related materials on the electrical and thermal conductivity of their polymer nanocomposites" *Polymer* 102 (2016) 292-300.

Chapter 5 studies how the properties of poly (butylene terephthalate) nanocomposites, containing the same nanoparticles exploited in Chapter 4, evolve upon ring opening polymerization. Cyclic butylene terephthalate nanocomposites containing GRM, owed to their intrinsically low molecular weight, cannot be regarded as materials for real application owing to their low mechanical properties. However, studying how nanocomposite properties change upon the ring-opening polymerization, can help in developing and optimizing reactive extrusion processing of pCBT nanocomposites. Part of the results reported in this chapter were published in the paper: "Morphology and properties evolution upon ring-opening polymerization during extrusion of cyclic butylene terephthalate and graphene-related-materials into thermally conductive nanocomposites" *European Polymer Journal* 89 (2017) 57-66.

In **Chapter 6** is reported an in-depth study on the effect of reduced graphene oxide, and its defectiveness, on the crystallization of poly (butylene terephthalate). Crystallization is studied by means of differential scanning calorimetry and X-ray diffraction. A very strong nucleation activity by GRM on pCBT was proven, especially for low defectiveness nanoflakes. In particular, the presence of a highly stable crystalline population was found as a consequence of heterogeneous nucleation.

In **Chapter 7** the optimization of different processing parameters in the preparation of pCBT nanocomposites through ring-opening polymerization of CBT is addressed. In particular, the effect of processing temperature, mixing time and shear rate on electrical and thermal conductivity of nanocomposites are described in this chapter, aiming at a systematic study of processing conditions vs. material properties. Part of the results reported in this chapter were published in: "Effect of processing conditions on the thermal and electrical conductivity of poly (butylene terephthalate) nanocomposites prepared via ring-opening polymerization" *Materials and Design* 119 (2017) 124-132.

Finally, in **Chapter 8** are reported general conclusions.

Chapter 2

Experimental

2.1 Materials

Pellets of cyclic butylene terephthalate oligomers [CBT100, Mw = $(220)_n$ *g/mol*, *n* = 2-7, melting point= 130 ÷ 160°C] were purchased from IQ-Holding[1] (Germany). Butyltin chloride dihydroxide catalyst (96%, m_p = 150°C, CAS # 13355-96-9) was purchased from Sigma-Aldrich while acetone (99+%) was purchased from Alfa Aesar. Cyclic butylene terephthalate oligomers (CBT) are materials characterized by an extremely low viscosity (~ $2 \cdot 10^{-2}$ Pa s at 190 °C, *i.e.* close to the value measured for water at room temperature). In presence of a proper catalyst (in this case butyltin chloride dihydroxide), CBT can polymerize into poly (butylene terephthalate) (pCBT) [146, 147], through ring-opening polymerization.

Different types of nanoparticles with different surface area were used for this study. GNP (Surface Area = 22 ± 5 m^2 g^{-1}), GNP-2 (Surface Area ~ 240 m^2 g^{-1}) and RGO (Surface Area = 210 ± 12 m^2 g^{-1}) were research grades (see Chapter 3 for the preparation method) synthetized by AVANZARE (Navarrete, La Rioja, Spain). The second grade of RGO was EXG98 350R, from now named RGO-2, (Surface Area > 300 m^2/g) by Graphite Kropfmühl (Hauzenberg, Germany). It is worth noting that, based on the terminology defined by Bianco *et al.* [27] and above reported, all the GRM here used belong to GNP. However, the two

[1] Distributor of products previously commercialized by Cyclics Europe GmbH

materials referred as GNP were synthetized from graphite intercalated compounds, whereas the two RGO were synthetized only by oxidizing graphite. For this reason, and to more clearly distinguish the different graphene related materials, we decided to use different names.

Part of GNP, RGO and RGO-2 were thermally treated at 1700 °C. A more detailed description of treatment method is described in Chapter 3.

2.2 Nanocomposite preparation

Standard extrusion

Standard extrusion was designed as a simple melt blending:

- CBT was extruded for 10 minutes at 250°C and 100 rpm, in inert atmosphere, in presence of tin catalyst (0.5 wt.% with respect to the oligomers content), thus obtaining pCBT (see Figure 2 for the polymerization reaction);
- At this point screw rotation speed was reduced down to 30 rpm and the proper GRM (5 wt.% with respect to the pCBT content) was added directly into the extruder;
- Extrusion was carried out for further 10 minutes at 250°C and 100 rpm.

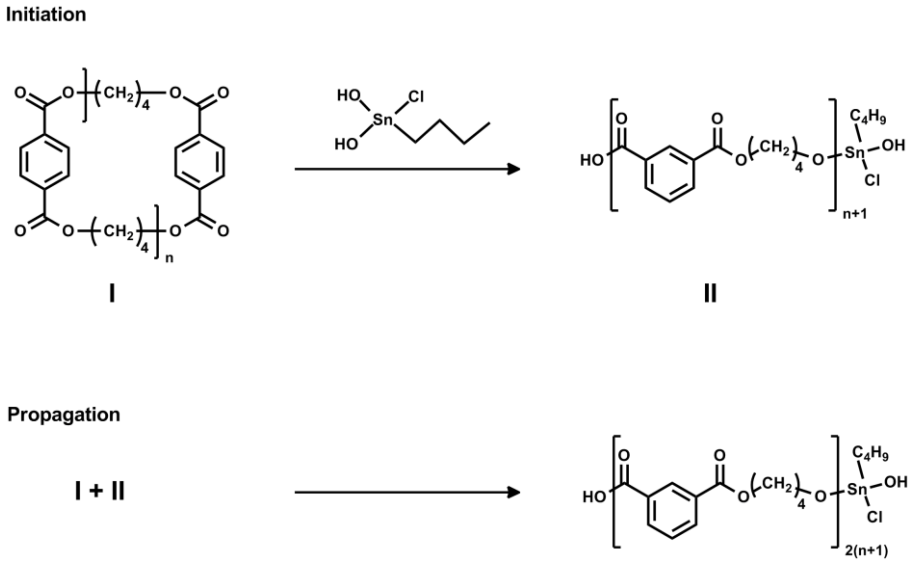

Figure 2. Scheme of the ring-opening polymerization of CBT into pCBT.

Solvent-assisted extrusion

This process was used aiming at a pre-dispersion of graphene-related materials, which could result in better dispersion and distribution of nanoflakes in the polymer matrix:

- CBT was extruded for 10 minutes at 250°C and 100 rpm in presence of butyltin chloride dihydroxide (0.5 wt.% with respect to the oligomers content), thus obtaining pCBT;
- pCBT was, then, completely dissolved under stirring pellets in Chloroform ($CHCl_3$)/1,1,1,3,3,3 Hexafluoroisopropanol (HFIP) (1/1 v/v) mixture ($CHCl_3$, ≥ 99.9%, Sigma-Aldrich; HFIP, ≥ 99%, Fluka); then, 5 wt.% of the proper GRM was added to the solution, manually mixed, and the solvent evaporated.
- The dried mixture was pulverized, added into the extruded and mixed for 10 minutes at 250°C and 100 rpm.

In-situ polymerization

This process was used aiming at a pre-dispersion of graphene-related materials, without changing any parameter other than the molecular weight, *i.e.* CBT *vs.* pCBT, respect to solvent-assisted extrusion.

Nanocomposites were prepared via a 2-step procedure:

1- About 17 g of CBT were partially dissolved in 120 ± 10 mL of acetone for 2 h under vigorous stirring. Then, the required amount of GNP or rGO was added to the solution and the system underwent a manual mixing for about 5 min. The obtained mixture was first dried in a chemical hood for 2 h, then in an oven at 80 °C for 8 h under vacuum (~10^1 mbar) to extract residual acetone and moisture, which could hinder CBT polymerization.

2- CBT nanocomposites were prepared by melt mixing the dried and pulverized CBT/GRM mixture into a co-rotating twin-screw micro-extruder (DSM Xplore 15, Netherlands) for 5 min at 100 rpm and 190 °C. pCBT nanocomposites were prepared by melt mixing the dried and pulverized CBT/GRM mixture for 5 min at 100 rpm and 250 °C; then, butyltin chloride dihydroxide catalyst (0.5 wt.% with respect to the oligomer content) was added and the process carried out for other 10 min (keeping screw speed and temperature constant) to complete CBT polymerization.

At the end of the extrusion process nanocomposites were collected and stored for further transformation and/or characterization.

2.3 Specimen preparation

For some tests, including rheological, mechanical, electrical and thermal characterization, the extruded materials required to be molded in order to prepare specimens with the proper sizes.

Compression molding was carried out through a laboratory platen press (Collin PT200, Dr. Collin GMBH, Germany) after drying the materials for ~ 8 h at 80 °C under vacuum (~10^1 mbar), to prevent hydrothermal degradation. Dried material was kept in the mold for 1 min at 190 °C and 250 °C for CBT and pCBT nanocomposites, respectively, then the plates of the press were closed and the pressure (~ 100 bar) was applied for about 30 seconds. After this period, the temperature was decreased down to ~ T_c-20 °C, (cooling rate ~ 60 °C min^{-1}), keeping the pressure constant. When the plates reached the extraction temperature, the pressure was released and the specimens were extracted from the mold. Specimens for thermal conductivity measurements were later polished to smooth and level surfaces.

2.4 Nanoparticle characterization

Scanning electron microscopy

Morphological characterization of graphene-related materials was carried out on a high resolution Field Emission Scanning Electron Microscope (FESEM, ZEISS MERLIN 4248). GNP and rGO, adhered on adhesive tape, were directly observed without any further preparation.

Raman spectroscopy

Raman spectra were collected on a Renishaw inVia Reflex (Renishaw PLC, United Kingdom) microRaman spectrophotometer equipped with a cooled charge-coupled device camera directly, on powder deposited on glass slide. Samples were excited with a diode laser source (514.5 nm, 2.41 eV), with a power of 10 mW. The spectral resolution and integration time were 3 cm^{-1} and 10 s, respectively. Four to five spectra were collected for each material, randomly selecting nanoflakes by means of an optical microscope coupled to the instrument. The deconvolution of D (~ 1350 cm^{-1}), G (~ 1580 cm^{-1}) and G' (~ 2700 cm^{-1}) peaks

was performed by fitting with Lorentzian functions. Raman spectroscopy is a powerful tool for the characterization of graphene and its related material, considering that it can provide information mainly on material defectiveness and thickness [149-154].

X-ray Photoelectron Spectroscopy

X-ray Photoelectron Spectroscopy (XPS) was implemented on a VersaProbe5000 Physical Electronics X-ray photoelectron spectrometer equipped with a monochromatic Al K-alpha X-ray source (15 kV voltage, 1486.6 eV energy and 1 mA anode current). Survey scans as well as high resolution spectra were recorded with a 100 μm spot size. Carbon nanoflakes were fixed on adhesive tape and kept under vacuum overnight to remove volatiles. Then, characterization was performed directly on nanoflakes, without any further preparation.

Deconvolution of XPS peaks was performed with a Voigt function (Gaussian/Lorentzian = 80/20) after Shirley background subtraction. For all the graphitic nanoflakes, the C_{1s} region shows an intense anisotropic peak with maximum centered at about 284.5 eV and a long tail, up to ~295 eV, related to overlapping of several peaks, whit a shape which is typical for reduced graphene oxide. The peak located at a binding energy (B.E.) ~ 284.5 eV is assigned to sp^2 C-C carbon while chemical shift of 0.5, 1.5, 2.5 and 4.0 eV are typically assigned to sp^3 C-C carbon, C-O, C=O and COOH functional groups, respectively[65, 67]. However, it is worth noting that in literature the assignment of the different peaks is often subjective and controversial[72, 155]. In this work, fitting of C_{1s} peaks was carried out positioning the peak related to sp^2 carbon at ~ 284.5 eV (depending on the material) and constraining the other peaks at + 0.5, + 1.5, + 2.5 and + 4.0 eV. A further peak related to π-π* shake-up transitions (~ 291.3 eV) was added without any constrain. Oxygen 1s assignment was reported to be less controversial in literature and various authors attributed binding energy values of ~ 533.0 and ~ 531.0 eV for single-bonded and double-bonded (C=O, O=C-OH) oxygen[67, 69, 156], respectively, even if some authors further distinguish between the B.E. of the different chemical bonds[67]. Moreover, it is worth noting that O_{1s} photoelectron kinetic energies are lower than those of C_{1s}, *i.e.* O_{1s} spectra are slightly more surface sensitive.

X-ray Diffraction

Wide-angle X-ray scattering (WAXS) patterns were obtained by an automatic Bruker D8 Advance diffractometer, in reflection, at 35 KV and 40 mA, using the nickel filtered Cu-Kα radiation (1.5418 Å). The instrumental broadening (β_{inst}) was determined by fitting of Lorentzian function to line profiles of a standard silicon powder 325 mesh (99%). For each observed reflection, the corrected integral breadths were determined by subtracting the instrumental broadening of the closest silicon reflection from the observed integral breadths, $\beta = \beta_{obs}{}^{-} \beta_{inst}$. The correlation lengths (D) were determined using Scherrer's equation.

$$D = \frac{K\lambda}{\beta \cos\theta} \quad (4)$$

where λ is the wavelength of the incident X-rays and θ the diffraction angle, assuming the Scherrer constant $K = 1$.

Thermogravimetric analysis

Thermogravimetric analysis (TGA) was performed by placing samples in open alumina pans on a Q500 (TA Instruments, USA), from 50 to 800 °C at the rate of 10 °C min^{-1} with a gas flow of 60 mL min^{-1}. The data collected were T_{max} (temperature at maximum rate of weight loss), T_{onset} (the temperature at which the mass lost is 3% of the initial weight) and final residue at 800 °C. TGA on graphene related materials was performed using about 2 mg samples under air flow (oxidative atmosphere). TGA in oxidative atmosphere can provide information on GRM quality [157].

2.5 Nanocomposite characterization

Scanning electron microscopy

Morphological characterization of CBT and pCBT nanocomposites was performed, to roughly evaluate dispersion and distribution of GRM in the polymer matrix. Analysis were carried out on a high resolution Field Emission Scanning Electron Microscope (FESEM, ZEISS MERLIN 4248). CBT and pCBT nanocomposites were fractured in liquid nitrogen to avoid plastic deformation, then coated with a thin layer (~5 nm) of Chromium before observation.

Differential scanning calorimetry

Differential scanning calorimetry (DSC) was carried out on a Q20 (TA Instruments, USA) with a heating rate of 10 °C min^{-1} (for 10 mg samples, 20 °C min^{-1} for 5 mg samples) in the temperature range 25 ÷ 190 °C and 25 ÷ 250 °C for CBT and pCBT nanocomposites, respectively. The method consisted on a first heating cycle, performed to erase the thermal history of the material, a cooling step, to study the crystallization of the nanocomposites and a last heating step to evaluate the melting temperature of materials. Crystallinity for pCBT nanocomposites was calculated as the ratio between the integrated value for heat of melting of the sample and the heat of melting of 100% crystalline poly (butylene terephthalate), *i.e.* 140 J g^{-1} [158], and normalized in nanocomposites taking into account of the effective polymer fraction in the sample.

In Chapter 6, different DSC experiments were performed. Standard scans, Self-Nucleation (SN) and Successive Self-Nucleation and Annealing (SSA) studies were performed in a DSC 8500 equipped with a Intracooler 3 cooling accessory (Perkin Elmer, USA). Isothermal crystallization experiments were carried out in a DSC Q20 equipped with a RCS 90 cooling system (TA Instruments, USA). Both instruments were calibrated with indium and zinc standards, and all the tests were performed with hermetically sealed aluminum pans under inert atmosphere (N_2) on dried samples (80 °C, ~ 100 Pa, overnight) to reduce hydrolysis of polymer.

Standard DSC experiments

Standard scans were carried out on 5.0 ± 0.5 mg samples in the range 25 ÷ 270 °C with a heating rate of 20 °C min^{-1}. The method consisted on an initial heating up to 270 °C, completed by an isothermal period of three minutes to erase the thermal history, followed by a cooling scan down to 50 °C and a last heating step up to 270 °C. The crystallinity degree was calculated by assuming 140 J g^{-1} for the heat of fusion of 100% crystalline PBT [158] and normalizing the enthalpy for the actual polymer content in nanocomposites.

Isothermal crystallization

Isothermal crystallization tests were carried out on 2.5 ± 0.3 mg samples thoroughly following the procedure recommended by Lorenzo *et al.* [159] Preliminary experiments were performed to ensure that no crystallization occurred during the rapid cooling to the selected T_c range (see details in Ref. [159]). Samples were heated up to 260 °C for 1 minute to erase their thermal history.

Then, samples were cooled at 40 °C min^{-1} to the selected isothermal crystallization temperature, T_c, and held at this temperature for 40 min. Fitting to the Avrami equation was performed by the Origin plug-in developed by Lorenzo *et al.* [159]

Self-Nucleation studies

The aim of self-nucleation (SN) is to produce self-nuclei by partial melting a "standard" crystalline state, taking into account that the ideal nucleating agent for any polymer should be its own crystal fragments or chain segment with residual crystal memory [160-162]. This technique was originally conceived for polymer solutions by Keller *et al*. [163], designed for DSC by Fillon *et al*. [160] and extensively exploited by Müller *et al*. [161]. Self-nucleation studies were carried out on 5.0 ± 0.5 mg samples, following this protocol:

(a) heating up to 260 °C (3 minutes isotherm at 260 °C) to erase thermal history and crystalline memory;
(b) cooling down to 25 °C at 20 °C min^{-1} (1 minute isotherm at 25 °C) to create a standard crystalline state;
(c) heating up to a self-nucleation temperature, T_s, at 20 °C min^{-1} and thermal conditioning at T_s for 3 minutes;
(d) cooling scan from T_s down to 25 °C at 20 °C min^{-1} (followed by 1 minute isotherm at 25 °C) to evaluate the effect of the thermal treatment on the crystallization behavior of pCBT;
(e) heating up to 260 °C at 20 °C min^{-1} to study the effect of the whole treatment on the melting of pCBT;
(f) repetition of step (b), (c), (d) and (e) at progressively lower T_s values to identify the different *Domains* [160]

At the end of self-nucleation experiments, three possible *Domains* can be observed, as a function of the T_s: *Domain I* when T_s is too high and complete melting of the sample occurs, *Domain II* when the melt retain some residual chain segmental orientation or crystalline memory (high temperature range) or some crystal fragments which cannot be annealed at the time spent at T_s (low temperature range) and *Domain III* when T_s is low enough to melt the material

only partially and, simultaneously, anneal unmolten crystals during the conditioning for 3 minutes at T_s. Furthermore, defining the different *Domains* during SN experiments is crucial to obtain the starting T_s for SSA tests.

Thermal fractionation by SSA

The aim of SSA technique is to perform an efficient thermal fractionation, *i.e.* to produce a distribution of lamellar crystals or thermal fractions by the application of a series of temperature steps, for different times, to a crystalline material. This technique is performed by a conventional differential scanning calorimeter and was developed and reviewed by Muller *et al.* [161, 162] Successive self-nucleation and annealing tests were performed on 2.5 ± 0.3 mg to compensate the heating rate increase. Hereby, the following experimental protocol was adopted:

(a) heating up to 260 °C (3 minutes isotherm at 260 °C) to erase thermal history and crystalline memory;

(b) cooling down to 25 °C at 20 °C min^{-1} (1 minute isotherm at 25 °C) to create a standard crystalline state;

(c) heating at 50 °C min^{-1} up to the ideal self-nucleation temperature ($T_{s,ideal}$), defined as the minimum T_s in *Domain II*, determined in SN experiments;

(d) holding at $T_{s,ideal}$ for 1 minute;

(e) cooling down to 25 °C at 50 °C min^{-1} to crystallize polymer after having been ideally self-nucleated;

(f) repetition of step (c), (d) and (e) at progressively lower T_s values to produce annealing of unmolten crystals (*i.e.* the thermal fractions) and self-nucleation of the molten polymer when the sample is cooled down. The fractionation windows, *i.e.* the difference in temperature between $T_{s,ideal}$ and T_s, was set at 5 °C and kept constant throughout the whole SSA experiment, determining the size of thermal fractions.

(g) Heating the sample up to 260 °C at 20 °C min^{-1} to reveal the consequence of SSA fractionation.

It is worth reporting that the short time spent at each T_s was necessarily required to limit the thermal degradation of the polymer matrix.

Intrinsic viscosity determination

The nanocomposites were dissolved in a mixture solvent of $CHCl_3$/HFIP (90/10 v/v) for ~ 1 h at room temperature, and filtered through a PTFE membrane (0.45 μm pore size) to separate GNP (efficiency of polymer extraction ~ 98 %, calculated by TGA). The polymer solution was concentrated under reduced pressure and dried at 80 °C overnight.

Intrinsic viscosity measurements [η] were performed with a Type II Ubbelohde capillary viscometer at 25 °C in a mixture of phenol/1,2-dichlorobenzene (50/50 w/w) (Phenol, ≥ 99.5%, Riedel-de Haën; 1,2-dichlorobenzene, ≥ 99%, Sigma-Aldrich), according to the ISO 1628-5. The pCBT samples were dissolved in the above mixture at 75 °C until complete solution was achieved (~ 1 h). The solution was then cooled to room temperature and the intrinsic viscosity of each sample was determined at concentrations ranging from 2 to 5 mg mL^{-1}, according to equation (5):

$$[\eta] = \lim_{C \to 0} (\eta_{rel} - 1) \cdot \frac{1}{C} \qquad (5)$$

where C is the concentration of the solution (g mL^{-1}) and η_{rel} is the relative viscosity calculated as

$$\eta_{rel} = \frac{\eta}{\eta_0} = \frac{t - \Delta t}{t_0 - \Delta t_0} \qquad (6)$$

where η and η_0 are the viscosity of the solution and of the solvent mixture, respectively, while t is the solution flow time and t_0 the solvent mixture flow time in the viscometer.

Five measurements were performed at each concentration for each pCBT sample to reduce the experimental error.

Molecular weight determination

The viscosity-average molecular weight, M_v, of the samples was calculated from the intrinsic viscosity [η] values, using the Mark-Houwink equation:

$$[\eta] = K \cdot M_v^{\alpha} \qquad (7)$$

where K and α are viscometric parameters which depends on polymer, solvent and temperature. For pCBT, K and α values of $1.17 \cdot 10^{-2}$ mL g^{-1} and 0.87, respectively [164, 165].

Wide angle X-ray scattering

Wide angle X-ray scattering (WAXS) measurements were performed on a Xeuss 2.0 SAXS/WAXS system (Xenocs SA, France). X-ray radiation (wavelength = 1.5418 Å) was produced by means of Cu-K_α radiation generator (GeniX3D Cu ULD) at 50 kV and 0.6 mA. Scattered signals were collected by a semiconductor detector (Pilatus 300 K, DECTRIS, Swiss) with a resolution of 487 x 619 pixels (pixel size 172 x 172 μm^2). Each room temperature WAXS pattern was obtained with 30 min exposure time. The one-dimensional intensity profiles were integrated from background corrected 2D WAXS patterns. Transmission geometry was adopted for *in-situ* measurements.

Temperature assisted WAXS were performed controlling the temperature by a Linkam TST 350 hot stage (Linkam Scientific Instruments, UK). Heating and cooling rates for the measurement were set at 20 °C min^{-1}. Specimens were hold for 1 min at the selected temperature to stabilize the temperature, then WAXS were obtained with 5 minutes exposure times. The thermal protocol consisted of 4 heating steps (200 °C, 215 °C, 235 °C and 260 °C) and 9 cooling steps (250 °C, 240 °C, 230 °C, 220 °C, 210 °C, 200 °C, 190 °C, 180 °C and 150 °C). WAXS patterns were collected at room temperature (~ 30 °C) before the beginning and after the completion of the thermal protocol to evaluate structural changes which could occur while keeping the material at high temperatures for long times.

Dynamic-mechanical thermal analysis

Dynamic-mechanical thermal analysis (DMTA) was implemented on a Q800 (TA Instruments, USA) with tension film clamp on ca. 30 x 5 x 1 mm^3 specimens. The experimental conditions were: temperature range from 30 to 190 °C, heating rate of 3 °C min^{-1}, frequency equals to 1 Hz and 0.05% of oscillation amplitude in strain-controlled mode.

Rheology

Rheological properties of CBT/GRM and pCBT/GRM nanocomposites were evaluated on a strain-controlled rheometer (ARES, TA Instruments, USA) with parallel-plate geometry on 25 mm diameter and 1 mm thickness disks. The test temperature was controlled by a convection oven, equipped with the instrument. Before each measurement, specimens were dried at 80 °C in vacuum for 8 h. Oscillatory frequency sweeps ranging from 0.1 to 100 rad/s with a fixed strain (set between 0.05 % and 0.1 %, depending on the nanocomposite, in order to perform experiments in the linear region, as determined by strain sweep tests) were performed in air at 190 and 250 °C (for CBT and pCBT, respectively), to investigate viscoelastic properties of nanocomposites. After sample loading, about 5 min equilibrium time was applied prior to each frequency sweep.

Electrical conductivity

Electrical conductivity (volumetric) was measured with a homemade apparatus on disk-shape specimens (1 mm thickness and 25 mm diameter). The apparatus for the measurement is constituted by:

- A tension and direct current regulated power supply (PR18-1.2A of Kenwood, Japan);
- A numeral table multimeter (8845A of Fluke, Everette/USA) furnished with a digital filter to reduce the noise of the measure;
- A palm-sized multimeter (87V of Fluke, Everette/USA);
- Two homemade brass electrodes: a cylinder (18,5 mm diameter, 55 mm height) and a plate (100 mm side, 3 mm thickness), indicated by a white arrow in Figure 3; every electrode has a hole for the connection and a wire (white circle in Figure 3) furnished with a 4mm banana plug.

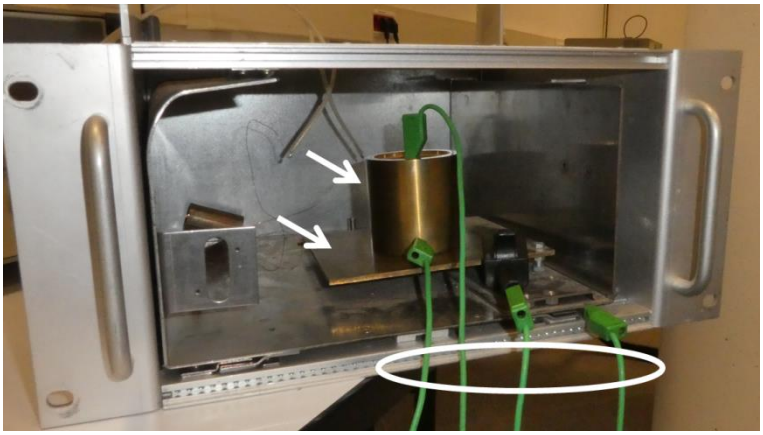

Figure 3. Cylinder and plate brass electrodes (indicated by arrow) for electrical conductivity measurements. The test specimen is placed in between the two electrodes.

The measurement system was based on the multimeter method. Power supply is time to time regulated in current or in voltage to have accurate measurement by both the multimeters, limiting the power dissipated on the specimen. The conductivity value was calculated with the following formula:

$$\sigma = \frac{1}{\rho} = \frac{1}{\frac{V}{I} \cdot \frac{S}{l}} \left[\frac{S}{m}\right] \qquad (8)$$

where S and l are the specimen surface and thickness, respectively; V is the voltage and I the electric current, both read by the apparatus.

Thermal conductivity

Isotropic thermal conductivity tests were carried out on a TPS 2500S by Hot Disk AB (Sweden) with a Kapton sensor (radius 3.189 mm) on disk-shaped specimens with thickness and diameter of about 4 and 15 mm, respectively. Before each measurements, specimens were stored in a constant climate chamber (Binder KBF 240, Germany) at 23.0 ± 0.1 °C and 50.0 ± 0.1 % R.H. for at least 48 h before tests. The test temperature (23.00 ± 0.01 °C) was controlled by a silicon oil bath (Haake A40, Thermo Scientific Inc., USA) equipped with a temperature controller (Haake AC200, Thermo Scientific Inc., USA).

Chapter 3

Nanoparticle synthesis and characterization

In this thesis, different types of graphene-related materials (GRM) were used, namely two graphite nanoplatelet grades (GNP and GNP-2) and two reduced graphene oxide (RGO, RGO-2). The properties of GRM strictly depend on the quality of such materials (especially in term of defectiveness, thickness, and lateral size) and directly affect the properties of the polymer matrix in nanocomposites. This implies that a careful characterization of GRM is mandatory for the understanding of nanocomposite properties. In this frame, the present chapter is aimed at nanoparticle characterization, as well as the description of GRM synthetic procedures.

3.1 Synthesis of graphene-related materials

A part of the graphene-related materials was provided by Avanzare Innovación Tecnólogica S.L (Spain) within the scientific collaboration in the frame of the project FET Flaghip n° 604391 "Graphene-Based Revolutions in ICT And Beyond" (2013-2016), also known as Graphene Flagship. Synthetic procedures for these materials, used in this thesis, are briefly described in the following.

For material purchased on the market, the limited info available on their synthetic procedures are also reported.

3.1.1 GNP

GNP were prepared using a rapid thermal expansion of graphite intercalated compounds, GIC. The intercalation of graphite with sulfuric acid to obtain graphite-sulphate is a well-known technology described for the first time by Hofmann and Rüdorff [63] . GIC were prepared starting from 500 g of natural graphite flakes (average lateral size ≈ 600 μm) and 5 kg of sulfuric acid, added in a 10 L glass jacket reactor under continuous stirring at T < 10 °C. Then, 200 g of $KMnO_4$ were added to the suspension, keeping the temperature below 10 °C. After the complete addition of permanganate, the system was heated up to 50 °C and kept at this temperature for 4 hours to allow the completion of the reaction (indicated by a change in the color of the suspension, from brown to black). At this point, the system was cooled to room temperature and the solution was added to about 50 L of refrigerated H_2O, by using a peristaltic pump, keeping the temperature lower than 70 °C. Hydrogen peroxide (400 g, 30 v.%) was slowly added, to remove the excess of MnO_4^-, and the suspension was maintained under stirring overnight at room temperature. The solution was then washed in 30 L of agitated 3.3 wt.% HCl solution for 1h. Finally, the solid was filtered, washed with osmotic water, until sulfate test gave a negative result (*i.e.* no turbidity observed when adding the solid to a 10 wt.% $BaCl_2$ water solution) and named GIC-1. GIC-1 was then introduced in a tubular furnace (N_2 atmosphere) at 1000°C for thermal expansion; a worm-like solid was obtained and mechanically milled (to separate nanoflakes) achieving GNP. GNP is characterized by a surface area of 22 ± 5 $m^2 g^{-1}$, and an average lateral size d_{50} = 53 μm. A schematic diagram of the various processing steps for GNP synthesis is reported in Figure 4.

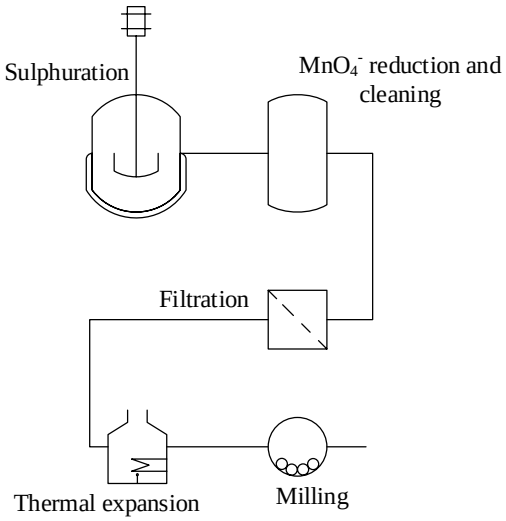

Figure 4. Sketch showing the steps involved in the preparation process of the graphite nanoplatelets, from now referred as GNP.

3.1.2 GNP-2

The GNP-2 was synthetized using a rapid thermal expansion of over oxidized-intercalated graphite (ox-GIC). In the present work, the synthesis of ox-GIC was made by adding 40 g of natural graphite flakes (average lateral size ≈ 1 mm) and 400 g of sulfuric acid (H_2SO_4) in a 5 liters refrigerated glass jacket reactor under continuous stirring at T < 10°C. Then, 5 g of nitric acid (HNO_3) were added drop by drop with a peristaltic pump, keeping the temperature constant. Later, 12.5 g of potassium permanganate ($KMnO_4$) were added to the suspension, keeping the temperature below 10°C. When $KMnO_4$ was completely added, the system was heated up to 50°C and stirred at this temperature for 1 hour to allow the completion of the reaction (indicated by a change on the color of the suspension, from brown to black). At this point the system was cooled to room temperature and the solution was pumped, with a peristaltic pump, into a tank of H_2O (≈ 2 L), keeping the temperature lower than 70°C. Hydrogen peroxide (H_2O_2, 30 g, 30 v.%) was slowly added to remove the excess of $MnO4^-$, and the suspension was maintained under stirring for about 30 min at room temperature. The solution was washed in 3 L of 3.3 wt.% HCl solution for 1h. Then, the solid was filtered, rinsed

with osmotic water (until the sulfate test gave a negative result), dried in air and then in an oven at 80°C. The resultant black powder was mechanically milled in a ball mill. The obtained solid, named ox-GIC, was then introduced in a tubular furnace under inert atmosphere (N_2) at 1000°C for thermal expansion, obtaining a worm-like solid; this was later mechanically milled, separating nanoflakes and obtaining GNP-2. GNP-2 is characterized by a surface area of ~ 240 m^2 g^{-1}, and an average lateral size $d_{50} \approx 70$ μm. A schematic diagram of the various processing steps for GNP-2 synthesis is reported in Figure 5.

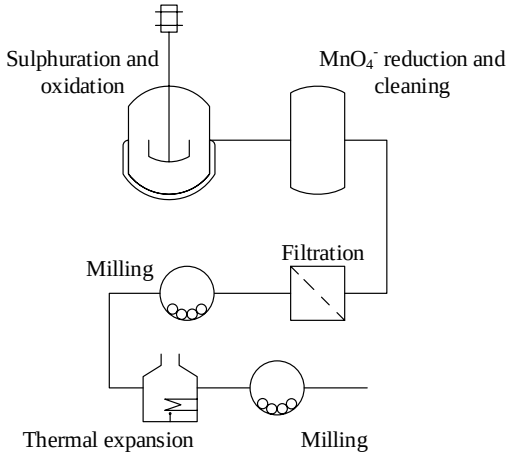

Figure 5. Sketch showing the steps involved in the preparation process of the graphite nanoplatelets, from now referred as GNP-2.

3.1.3 RGO

Reduced graphene oxide was produced by thermal reduction of graphene oxide, previously synthetized using a modified Hummers method [62] starting from 250 g of natural graphite (600 μm average lateral size). The reaction temperature inside the reactor was maintained between 0 and 4°C during oxidant addition (48h; H_2SO_4 98%, 15.6 Kg; $NaNO_3$, 190 g; $KMnO_4$ 1200 g). Then, the temperature was gradually increased to 20ºC and kept constant for 5 days. A H_2O_2 solution (50 L H_2O; 750 g H_2O_2 30 v.%) was used to remove the excess of MnO_4^- over a period of 24 hours. After sedimentation, the solution was washed in a mechanically stirred HCl 4 wt.% solution for 8 h (600:1 washing solution: graphite). The solid was filtered, washed with osmotic water and dried at 80ºC. 100 g of GO were ultrasonicated in isopropanol for two times and placed at reflux overnight. The solid was then removed, filtered and air-dried. This product was later treated in inert atmosphere (Ar) at 1000 °C for 30 sec for the thermal

expansion and, then, at 1150 °C for 20 min, leading to the obtainment of a black solid with an apparent density of ~ 0.002 g dm^{-3}, which is from now on referred to as RGO. RGO is characterized by a surface area of 210 ± 12 m^2 g^{-1}, and an average lateral size $d_{50} \approx 39$ μm. A schematic diagram of the various processing steps for RGO synthesis is reported in Figure 6.

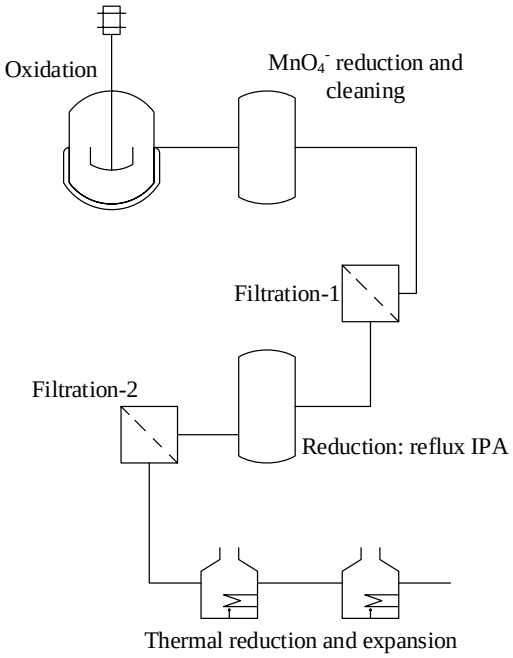

Figure 6. Sketch showing the steps involved in the preparation process of the reduced graphene oxide, from now referred as RGO.

3.1.4 RGO-2

RGO-2, commercial name EXG 98 350R, was purchased from Graphit Kropfmühl GmbH (Germany). It was synthetized by oxidation of graphite followed by thermal reduction at high temperature. It consists in a multi-layer graphene, characterized by a surface area > 350 m^2 g^{-1}, and an average lateral size $d_{50} = 11$ μm.

3.1.5 Thermal annealing of graphene-related materials

The possibility to reduce or restore structural defects in graphene-related materials by thermal annealing at high temperatures (at temperatures in the range 1000 ÷

2700 °C) is well known [69, 166, 167]. For this reason, some of the graphene-related materials used in the present work were treated at 1700 °C for 1 hour under vacuum (~ 50 Pa) in a Pro.Ba. vacuum oven, heated by graphite resistors. Graphite box containing about from 1 to several grams of graphene-related materials (depending on the apparent density) were heated up to the annealing temperature and cooling down to room temperature were carried out at 5 °C/min to limit thermal stresses in the graphite oven. The suffix "_1700" will be added to all the material thermally annealed to be distinguished from their relevant pristine GRM.

3.3 Graphene-related materials characterization

Nanoparticle characterization carried out in this thesis is described below for each material. Characterization of thermally treated nanoflakes will be reported in the same subsection as their pristine counterpart, in order to highlight the effect of thermal annealing on the nanoflake properties.

3.3.1 GNP and GNP_1700

Morphology

The analysis on GNP morphology, reported in Figure 7a, shows the presence of aggregated and folded flat nanosheets with lateral size ranging from few hundred nanometers to several micrometers and thickness estimated in the range of 10 ÷ 20 nm. The annealing at 1700 °C did not affect GNP morphology, as observable in Figure 7b.

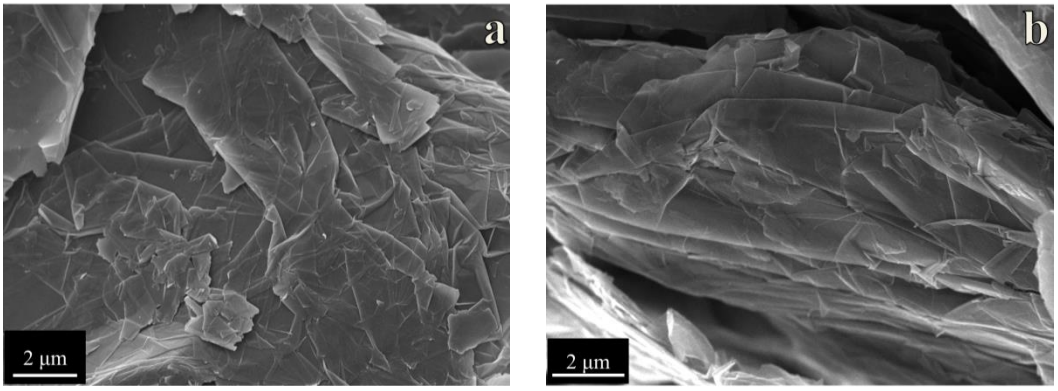

Figure 7. FESEM micrographs for (a) GNP and (b) GNP_1700

Raman spectroscopy

First- and second-order Raman spectra for GNP and GNP_1700 are reported, normalized with respect to the G peak (ca. 1580 cm^{-1}) in Figure 8. The first-order Raman spectrum for GNP exhibits a tiny signal at ~ 1350 cm^{-1} (defect-related D-band) and a strong band at ~ 1578 cm^{-1} (G-band). Thus, the I_D/I_G ratio is very small (~ 0.07), evidencing very limited defectiveness of this GNP. The second-order band at higher Raman shift is the convolution of two main peaks (G'_1 and G'_2) located at ~ 2690 cm^{-1} and ~ 2725 cm^{-1}, respectively, which are typical for graphitic materials constituted by more than 5 graphene layers [168]. After thermal annealing, the intensity of the D band slightly decreases, resulting in a decrease in the I_D/I_G ratio down to ~ 0.03. Furthermore, no clear differences before and after annealing were observed for G' band, which was deconvolved into two main peaks, as for pristine GNP. Despite the I_D/I_G ratio reduced after annealing, no dramatic changes in the structure of GNP can be claimed based on Raman spectroscopy results.

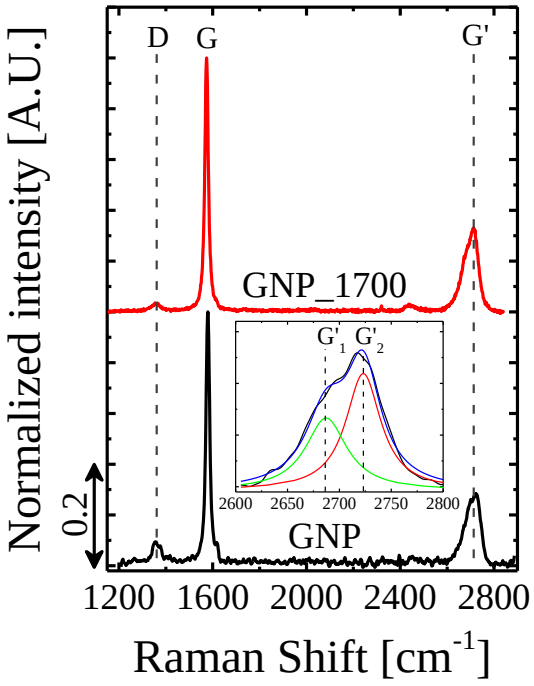

Figure 8. Representative Raman spectra for GNP and GNP_1700

XPS

XPS was used to study the chemical compositions of GNP before and after thermal annealing. The oxygen content for the different nanoflakes, calculated by integration of survey scan peaks, was measured at 1.8 and 0.8 at.% for GNP and GNP_1700, respectively, indicating a significant decrease of the oxygen content upon thermal treatment at high temperature.

For both GNP and GNP_1700, the C_{1s} region shows an intense anisotropic peak with maximum centered at about 284.3 eV and a long tail, up to ~295 eV, related to overlapping of several peaks. XPS C_{1s} results for GNP (Figure 9a) shows the presence of an intense and narrow sp^2 C-C signal coupled with a relatively intense signal due to π-π^* shake-up transition which reveal a good aromaticity degree of the graphitic structure. The fitting of the C_{1s} is completed by three weak peaks at 284.8, 285.8 and 288.3 eV which, accordingly with literature, were assigned to sp^3 C-C, C-O (C-OH and/or C-O-C) and O=C-OH chemical bonds, respectively. The amount of sp^2 C-C was estimated as ~ 70%. Deconvolution of O_{1s} band (Figure

9b) required the use of three peaks centered at 531.6 (double bonded oxygen), 532.4 (C-O-C) and 533.2 eV (C-OH) suggesting a higher content of double bonded respect to single bonded. After annealing at 1700 °C, no significant variation were observed in the C_{1s} deconvolution (sp^2 C-C ≈ 70%), while the intensity of the O_{1s} band was significantly reduced and a reasonable fitting was possible with a single peak centered at 532.4 eV (C-O-C). These results indicate that the used temperature was sufficiently high to remove all the C=O groups, whereas some C-O groups remain in the graphitic structure.

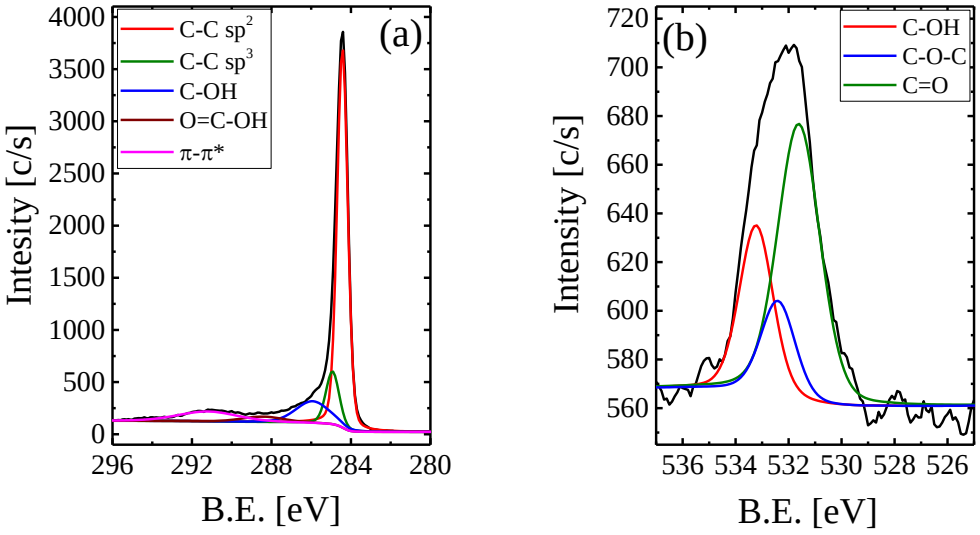

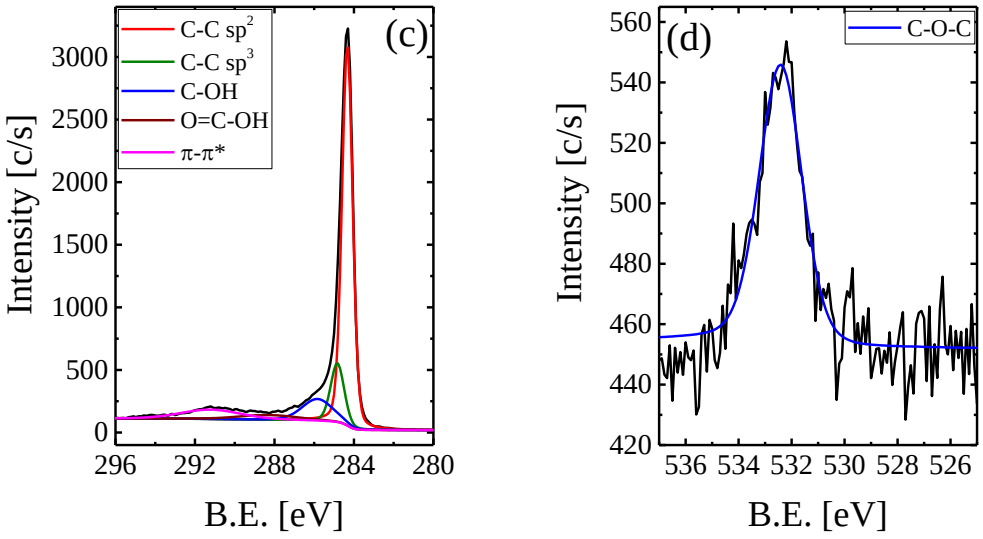

Figure 9. XPS curves with their deconvolution peaks for (a) C_{1s} and (b) O_{1s} of GNP and (c) C_{1s} and (d) O_{1s} of GNP_1700. For all the spectra, the black line indicates raw data.

TGA

Thermal stability of GNP, before and after the thermal treatment at 1700 °C, was evaluated by TGA in air (Figure 10) to indirectly investigate their structural features, knowing that the onset decomposition temperature can be qualitatively related to the size and the defectiveness of graphene-related materials [157]. T_{onset} for GNP was measured at ~ 630°C with the maximum mass loss rate centered at ~770 °C. After annealing, the T_{onset} shifts to ~ 783 °C, *i.e.* ~ 150 °C shift respect to pristine GNP, thus indicating higher thermal stability obtained with the thermal treatment, whereas it was not possible to measure the peak of mass loss rate in the selected temperature range. Considering the amount of sp^2 C, ~ 70% estimated by XPS, and based on Raman spectroscopy, such high thermal stability could be related on the removal of less thermally stable oxygen groups in the graphitic structure, during the annealing at 1700 °C [169]. The presence of groups could act as triggers for the degradation of GNP in the presence of oxygen, considering that typically oxygen is removed from graphene as CO or CO_2 [170].

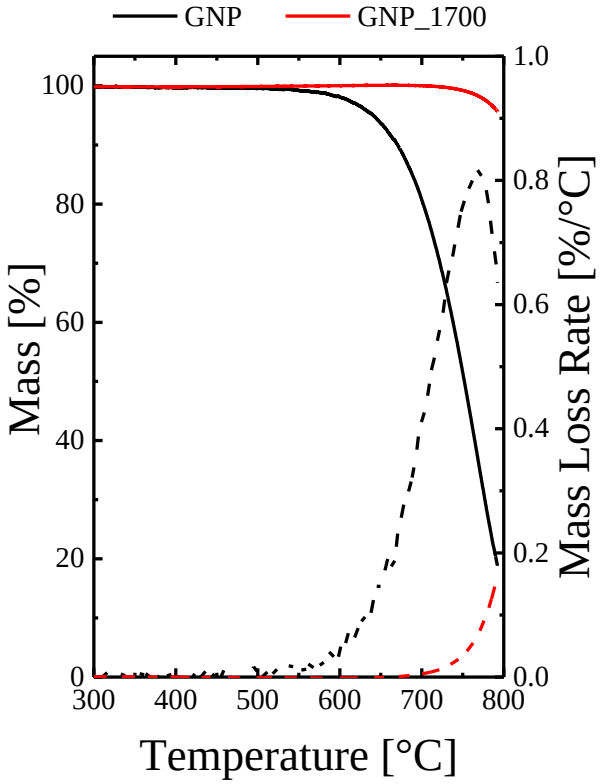

Figure 10. Mass vs. temperature (solid lines) and Mass loss rate vs. temperature (dashed lines) plots for GNP and GNP_1700.

3.3.2 GNP-2

Morphology

The morphology of the as received GNP-2, showed in Figure 11a, reveals few nanometer thick wrinkled layers, organized in accordion-like structures of some mm length and ~ 200 μm lateral size. However, high magnification micrographs show separated nanoflakes (Figure 11b) on the scale of some tens of micrometers and thickness estimated in few nanometers. It is worth considering that a similar expanded structure is typical of the thermal expansion process, as observed for thermally reduced graphene oxide [51].

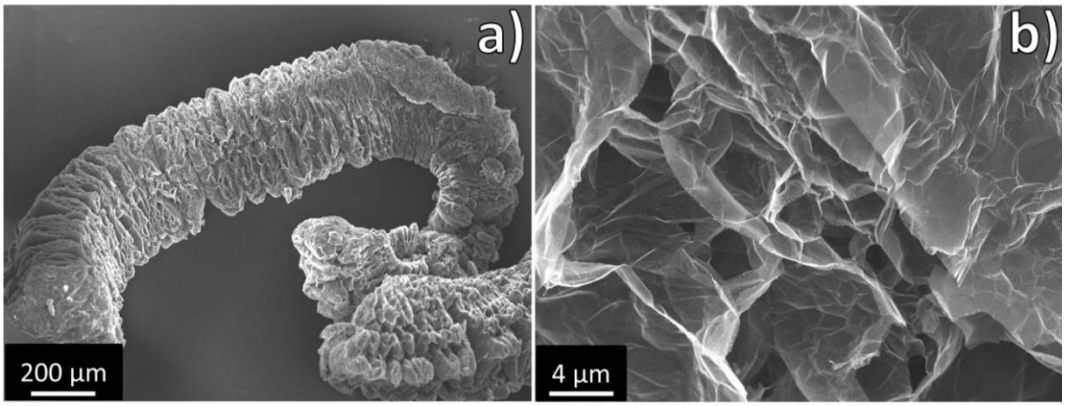

Figure 11. (a) Low and (b) high magnitude FESEM micrographs on GNP-2

Raman spectroscopy

Representative Raman spectrum for GNP, normalized with respect to the G peak (~ 1573 cm^{-1}), is displayed in Figure 12. First-order Raman spectrum shows a tiny D band at ~ 1358 cm^{-1} and a strong and narrow G band. This results in a low I_D/I_G ratio ($I_D/I_G \approx 0.06$, calculated from the intensities of fitting peaks), thus indicating low defectiveness of GNP [35]. The second-order spectrum shows the presence of an intense band located at about 2710 cm^{-1} (G' band), which is deconvolved into two main peaks located at ~ 2682 cm^{-1} (G'_1) and ~ 2715 cm^{-1} (G'_2), respectively. Both bands are characteristic of graphene-related materials constituted by more than five graphene layers [168].

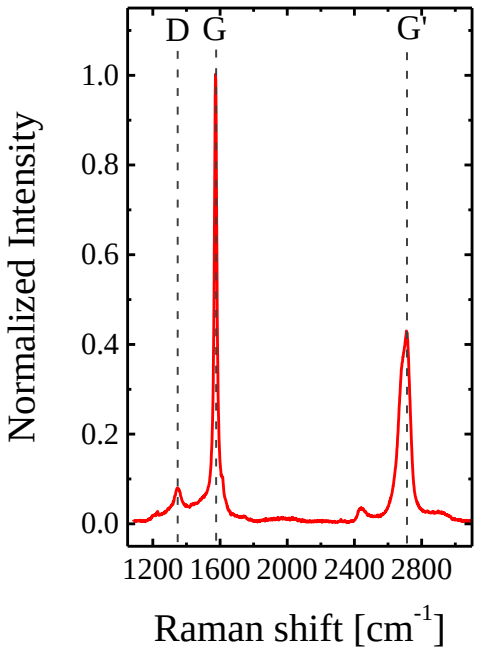

Figure 12. Representative Raman spectrum for GNP-2

XPS

Chemical composition of GNP-2 nanoflakes was evaluated by means of XPS. The oxygen content of GNP, calculated from the integration of survey scan peaks of XPS data, was ~ 5.0 at.%, thus indicating a C/O ratio of about 19/1. A deeper insight on the functional groups was performed by deconvolution of C_{1s} (B.E. ≈ 285 eV, Figure 13a) and O_{1s} (B.E. ≈ 530 eV, Figure 13b) peaks, collected by narrow scans. C_{1s} spectra (Figure 13a) show an intense peak located at ~ 284.2 eV, assigned to sp^2 C-C carbon (sp^2 C ≈ 72%), and a long tail which was deconvolved with five peaks centered at: ~ 284.7 eV (sp^3 C-C carbon), ~ 285.6 eV (C-OH, C-O-C), ~ 286.7 eV (C=O), ~ 287.7 eV (HO-C=O) and ~ 290.8 eV (π-π* shake-up of the aromatic carbon) [65, 67, 69]. It is worth noting that the relatively intense π-π* peak and a narrow sp^2 C-C peak (FWHM ≈ 0.69 eV) are typically related to the high aromaticity degree in the graphitic structure [35, 69]. Deconvolution of O_{1s} signal is reported in Figure 13b: a reliable fitting into two peaks was obtained, thus indicating the coexistence of single-bonded (~ 533.0 eV,

C-OH/C-O-C) and double-bonded oxygen (~ 531.4 eV, C=O/O=C-OH), in agreement with the deconvolution of C_{1s} signal.

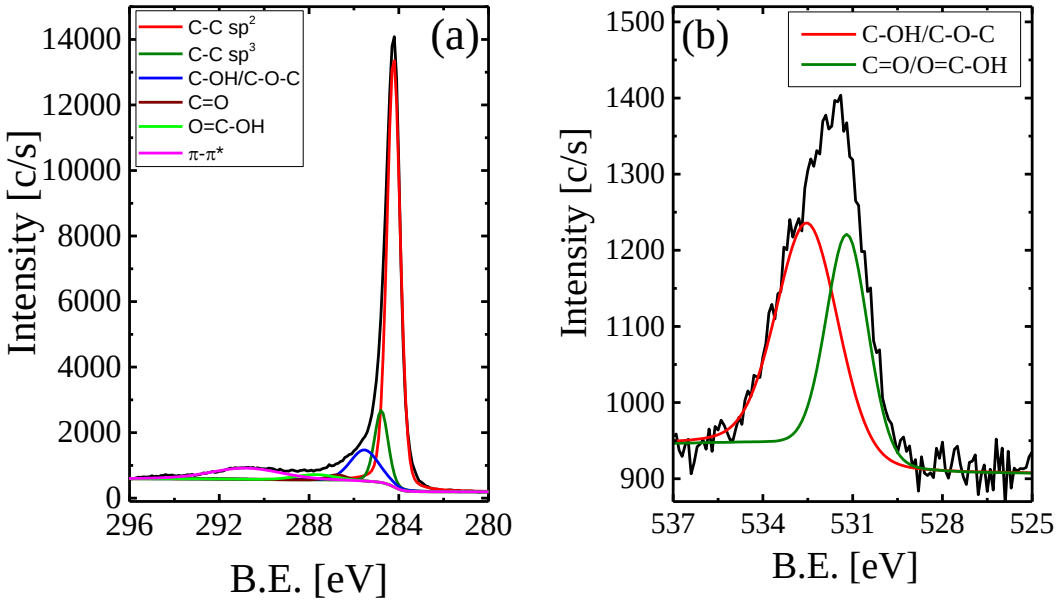

Figure 13. XPS curves with their deconvolution peaks for (a) C_{1s} and (b) O_{1s} of GNP-2. For all the spectra, the black line indicates raw data.

TGA

The thermal stability of GNP-2, and hence a further qualitative evaluation of its defectiveness, was studied by TGA in air (Figure 14). The thermogram of the GNP-2 exhibits two degradation steps: in the first, weight loss of about 6 wt.% occurred between ~ 450°C and 600°C, which could be related to smaller and highly defective nanoparticles. In the second step a further 80 wt.% loss is verified between ~ 600°C and 850°C, with the maximum of mass loss rate centered at ~ 762 °C, thus indicating an high content of large and low defective nanoflakes, according to the work of Shtein et al [157]. These results revealed a lower defectiveness of GNP-2 with respect to GNP, thus suggesting this material as a better candidate for the improvement of thermal conductivity of polymer nanocomposites.

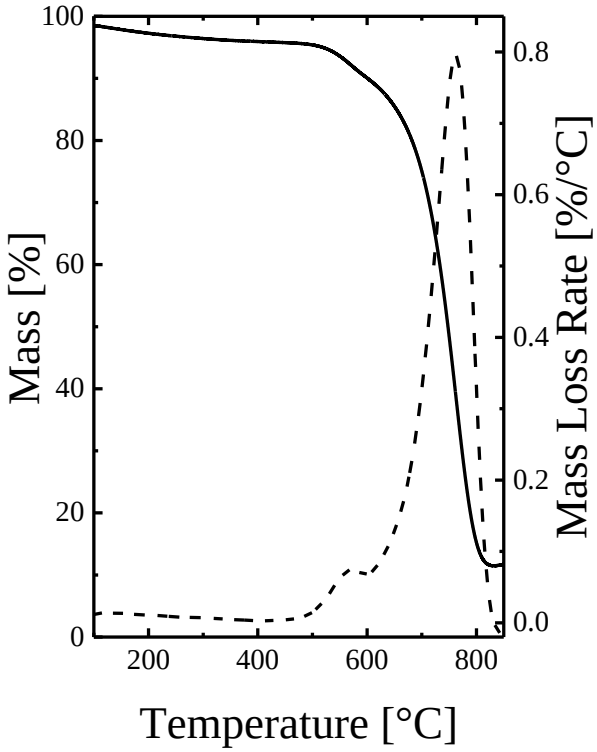

Figure 14. Mass vs. temperature (solid lines) and Mass loss rate vs. temperature (dashed lines) plots for GNP-2.

3.3.3 RGO and RGO_1700

Morphology

Scanning electron microscopy was used to characterize the RGO flakes before and after annealing. In untreated RGO, a highly expanded house-of-cards-like structure is visible (Figure 15a,b), consisting of randomly aggregated wrinkled and folded sheets in a three dimensional porous architecture. Despite accurate measurements of the thickness of the visible RGO are not possible in these conditions, flakes thickness is estimated to be in the range of a few nm. The annealing process at 1700°C does not significantly alter the morphology, structure or apparent thickness of the graphite plates, even if the structure appears slightly more expanded after the annealing treatment (Figure 15c,d).

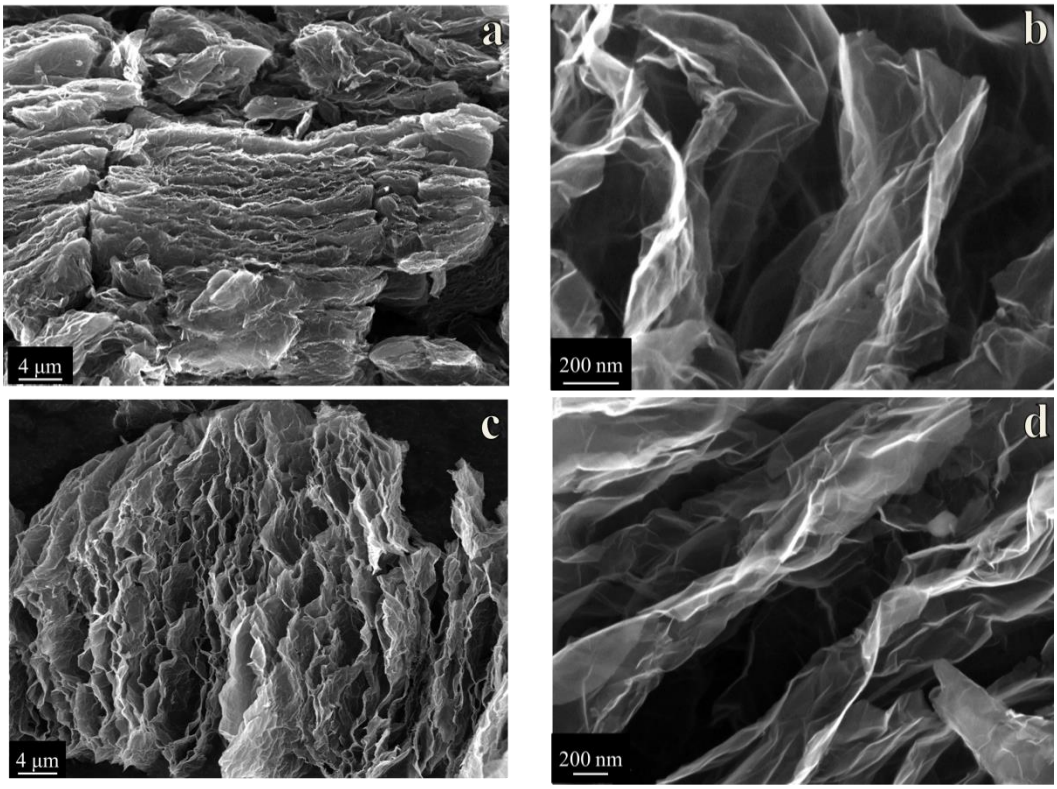

Figure 15. High magnification and low magnification FESEM micrographs for RGO (a and b) and RGO_1700 (c and d)

Raman spectroscopy

Raman spectroscopy has been performed on RGO and RGO_1700 in order to extract information about the samples microstructure. Figure 16 shows first- and

second-order Raman spectra of representative nanoflakes which present a noticeable variation after thermal annealing. The first-order RGO Raman spectrum is composed by two strong resonances at ~1350 cm^{-1} (defect-related D band) and at ~1583.5 cm^{-1} (G band); the last vibrational mode is convolved with a weaker feature at ~1615 cm^{-1} which can be ascribed to the disorder-induced D' band [153]. The second-order RGO spectrum shows three different bands (G´, D + G, and 2D´) typical of disordered graphitic materials and oxidized graphene [171]. The G' mode at ~2692 cm^{-1} is due to a double resonance intervalley Raman scattering process with two iTO phonons at the K point, whose intensity is sensitive to the presence of structural disorder. The D+G peak at ~2927 cm^{-1} is a combination mode and the 2D' peak at ~3194 cm^{-1} is the second-order mode of the D' band. After annealing, the Raman spectrum yields, as expected, a marked evolution towards a more ordered graphitic structure. Actually, the G band evidenced at ~1575 cm^{-1} is shrunk and much more intense, the D' mode disappears and the D peak, still present at ~1352 cm^{-1}, becomes very weak. In particular, the I_D/I_G ratio strongly decreases from ≈ 1.19 for the non-annealed sample (suggesting a high concentration of defects in the aromatic structure, including sp^3 carbons and possible residual oxidized groups [149, 172, 173]), to ≈ 0.023 for the thermally treated one. Coherently with the expected decrease of the structural disorder, the second-order spectrum of RGO_1700 shows a higher intensity for the G' peak located at ~2705 cm^{-1}. Such band shows a certain asymmetry, which can be justified with the interplanar stacking order of graphene layers. On one hand, graphitic materials with high stacking order such as highly oriented pyrolytic graphite (HOPG) exhibits an asymmetric lineshape that can be fitted with two Lorentzian components ($G´_{3DA}$ and $G´_{3DB}$) due to Bernal staking arrangement of individual graphene layers [153]. On the other hand, materials characterized by graphene layers randomly oriented (turbostratic stacking) are featured by a symmetric G' band that can be fitted with a single Lorentzian component (G'_{2D}) [69]. As can be noticed in the inset of Figure 16, the G' band of RGO_1700 specimen show the coexistence of G'_{2D}, $G´_{3DA}$ and $G´_{3DB}$ Raman peaks., yielding a fractional 3D graphitic volume experimentally found as $IG'_{3D}/(IG'_{3D} + IG'_{2D})$ ≈ 60%, giving a proof of a high degree of three-dimensional order.

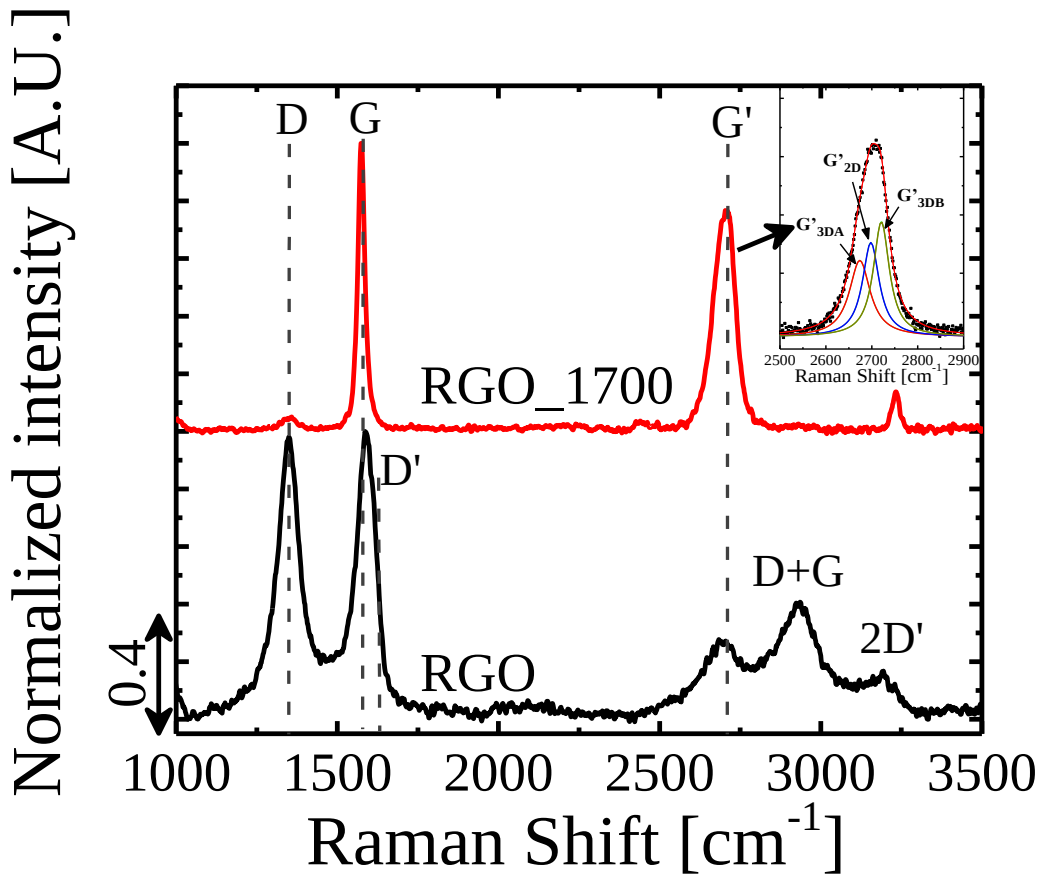

Figure 16. Representative Raman spectra for RGO and RGO_1700. The inset shows the deconvolution of G' peak of RGO_1700.

XPS

Composition of the flakes before and after annealing was studied by XPS analyses which evidenced the presence of 3.2 at.% oxygen in pristine RGO, while most of the oxidized groups were eliminated during the annealing, as the oxygen concentration has reduced to 0.4 at.% after annealing. However, it is worth noting that the treatment does not eliminate only the oxygen as the weight loss upon treatment was measured to be in the range of 10 wt.%. This is partially explained by the fact that oxygen is typically eliminated as CO or CO_2 [170], thus removing some carbon which contributes to the weight loss. Furthermore, elimination of other unstable carbon in proximity of the edges and/or next to surface defects is also possible, contributing to the total weight loss during the annealing. To further

investigate the materials chemical structure before and after the annealing, XPS spectra were carefully fit on both O_{1s} and C_{1s} signals, as shown in Figure 17.

For oxygen 1s in RGO, despite the relatively low intensity of the signal due to low oxygen content, two partially overlapping oxygen peaks were clearly observed, which obviously require at least two peaks for fitting. Deconvolution of this peak with two Gaussian-Lorentzian (80:20) after Shirley background subtraction delivered a satisfactory fitting with peaks at 533.2 and 531.0 eV, the higher binding energy showing a slightly higher intensity. The signal at 533.2 eV is generally assigned to single-bonded oxygen, C-O, whereas the peak at lower binding energy (531.0 eV) is typically assigned to double-bonded oxygen species, namely carbonyl group C=O or carboxylic groups O=C-OH [67, 69]. Some authors further distinguish different positions for C-O-H and C-O-C, as well as for C=O and O=C-OH. However, given the relatively low signal for O1s, reliable fitting with all these four signals seemed unrealistic and a simpler deconvolution was preferred. In fact, the existence of both single- and double-bonded oxygen species revealed the presence of different types of residual oxidized species on RGO, which is consistent with previously proposed thermal evolution of graphene oxide [155].

On the other hand, annealed RGO showed a very weak O_{1s} band which was fitted by a single Gaussian-Lorentzian with peak at 532.4 eV. The lower intensity clearly reflects the total amount of oxygen, which was strongly reduced during annealing at 1700 °C, whereas the position of the peak is quite close to the one assigned to single-bonded oxygen species. This suggests that carbonyl and carboxylic groups are mostly eliminated during annealing, whereas some C-O groups are still observed after the high temperature annealing, likely in the form of phenolic groups, as previously proposed by Ganguly at el. [155].

Carbon (C_{1s}) band for RGO showed a maximum at 284.5 eV and a strongly asymmetric shape extending to higher binding energies up to about 295 eV, clearly showing the overlapping of several different signals related to carbon atoms with different chemical environments. This binding energy distribution is typical for reduced graphene oxide and fits with several peaks have been reported by many different authors [67, 69, 70, 155, 174]. For this material, a reliable fitting was performed with five peaks, the main, related to sp^2 carbon located at 284.5 eV. The optimized fitting centered the other peaks at 285 eV (sp^3 carbon), 286 eV (single bonded oxygen), 288.5 eV (double bonded oxygen, in the form of

carboxylic group) and 291.1 eV (π- π* shake up). These results are in accordance with the fitting of the O_{1s} signal.

The same fitting procedure was applied to RGO_1700 and the optimized position for the other peaks turned out to be almost identical to the case of RGO described above. Comparing the deconvolved signals for RGO and RGO_1700, we can notice that, besides a slight decrease of intensities for the peaks of the oxidized species after annealing, some differences are present for the peaks related to graphitic C-C. In particular, a decrease from 0.78 to 0.63 for the full width at half maximum (FWHM) of sp^2 C was found upon annealing. The FWHM was previously reported to be sensitive to heterogeneity of both the chemical and the structural environment of carbon [69]. Furthermore, the intensity of the π-π* shake-up band was increased in intensity upon annealing, which was also previously assigned to a restoration of aromaticity in the structure after removal of oxygen [69].

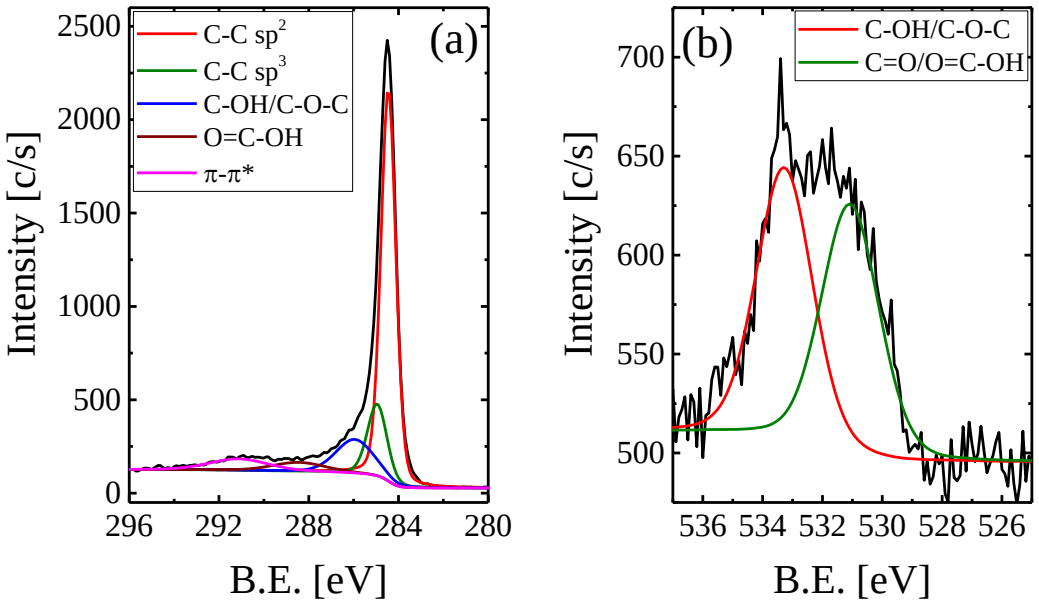

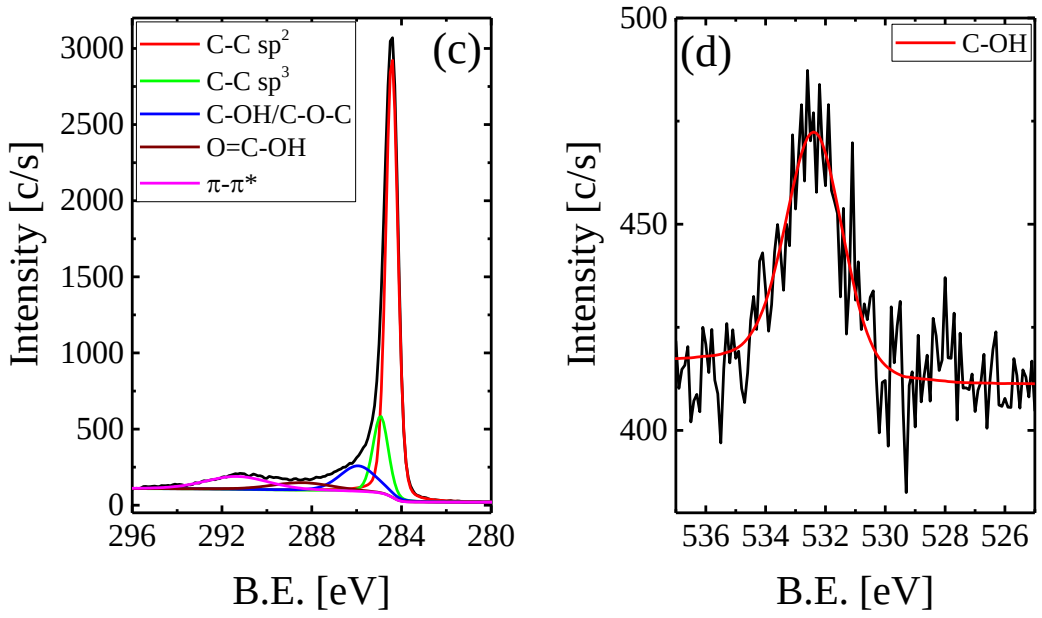

Figure 17. XPS curves with their deconvolution peaks for (a) C1s and (b) O1s of RGO and (c) C1s and (d) O1s of RGO_1700. For all the spectra, the black line indicates raw data.

XRD

X-ray diffraction was used to study the crystalline order of RGO and annealed RGO; WAXD patterns for both materials are reported in Figure 18.

For RGO, the 002 reflection at 2θ = 26.3°, corresponding to the spacing between graphitic layers (0.339 nm), exhibits a half height width β = 1.35°, giving an average correlation length perpendicular to the graphitic layers of D_{002} = 6.7 nm (Figure 18). This 002 reflection is overlapped to a significant amorphous halo, which is similar to the main diffraction halo of disordered graphitic materials, like *e.g.* calcined petroleum coke (Figure 18, curve A). A deconvolution of the 002 peak and of the amorphous halo in the 2θ range 18° ÷ 40° allows evaluating the amount of graphite nanoplatelets as close to 30 wt.% of the RGO sample. This confirms a significant disorder in the RGO structure, in agreement with Raman results. The WAXD pattern of RGO also shows a less intense amorphous halo, centered at 2θ = 43.5°, essentially similar to the second amorphous halo of petroleum coke (Figure 18, curve A). The WAXS pattern of RGO also shows weak reflections at 2θ = 54.4° and 77.5°, corresponding to 004 and 110 graphite

reflections. It is worth adding that the half height width of the isolated 110 reflection (β = 0.63°), allows evaluating an average correlation length parallel to the graphitic layers (more precisely perpendicular to the 110 planes) of D_{110} = 18 nm. Moreover, the absence of 101 and 112 reflections clearly indicate a complete absence of hexagonal order and hence the formation of a turbostratic structure.

After the high temperature thermal annealing, significant modification of the XRD pattern (Figure 18, Curve C), with all reflections becoming sharper and more intense, was observed. A narrowing of the 002 reflection was obtained after annealing, with half height width β = 0.98°, corresponding to an increase of the average correlation length perpendicular to the graphitic layers up to D_{002} = 9.3 nm. The peak deconvolution in the 2θ range 18° ÷ 40° indicates that the amount of graphite nanoplatelets increases up to 52 wt.% of the sample. At higher 2θ angles, the amorphous halo between 42 and 46° definitely changes with the appearance of the in-plane 100 reflection (2θ = 42.5°; d = 0.213 nm) but also with its centering at d = 0.205, corresponding to the position of the 101 reflection. This indicates that annealing also brings to some partial hexagonal order in the stacking of the graphitic layers. The half-height width of the isolated 110 reflection (β = 0.47°) indicates an increase of the average correlation length parallel to the graphitic layers up to D_{110} = 24 nm.

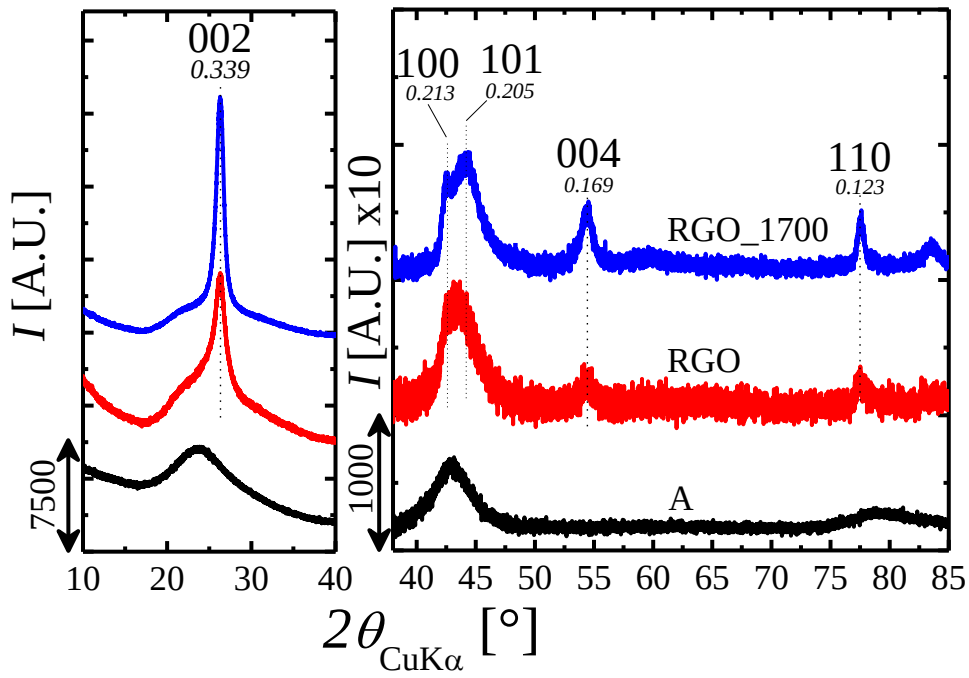

Figure 18. X-ray diffraction patterns (CuK*α*) of RGO and RGO_1700. The amorphous fraction of the samples presents diffraction halos similar to those of calcined petroleum coke (A).

TGA

Thermogravimetry was also used to indirectly assess the defectiveness of RGO. Indeed, large and well graphitized flakes are typically stable in air up to temperatures in the range of 700°C while the presence of sp^3 carbons, as defects on the surface or at the flake edges, may trigger the subsequent oxidation and volatilization of graphene-based materials [157]. Pristine RGO showed an onset of weight loss at 558°C, after which the volatilization process continues, leading to a stable residue of about 7% above 750°C (Figure 19), mainly corresponding to silicate impurities in the natural graphite used, as indicated by the energy dispersive spectroscopy analysis under SEM. It is worth noting that volatilization occurs in two partially overlapping steps, which can be explained by polydispersity of lateral flake size. On the other hand, annealed RGO showed significantly higher thermoxidative stability, as evidenced by the onset temperature at 748°C, further supporting the reduction of sp^3 carbons upon annealing, similar to results observed for annealed GNP.

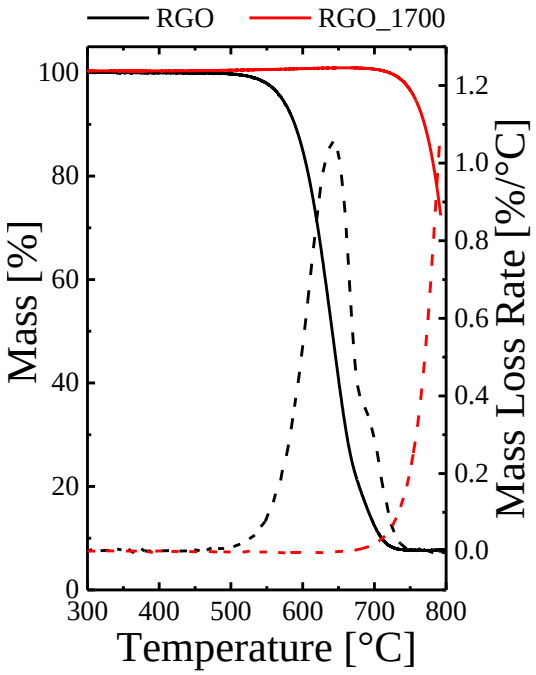

Figure 19. Mass vs. temperature (solid lines) and Mass loss rate vs. temperature (dashed lines) plots for RGO and RGO_1700

Based on the characterization results, we can conclude that a dramatic evolution of the RGO chemical structure and morphology was obtained during the annealing at 1700 °C. In particular, a strong reduction of oxygen content was evidenced by XPS analysis, especially by elimination of carboxylic and carbonyl groups, as the few remaining oxygenated groups can be assigned to phenols. Elimination of oxygen from RGO was reported to introduce vacancies in the graphene flakes, for which extensive annealing was reported to require temperatures higher than 1700°C [23]. This suggests that a full aromatization cannot be expected by the treatment applied in this paper. However, a significant reduction of defectiveness was evidenced by Raman, together with an evolution towards a more ordered stacking of grafene layers, as confirmed, also, by XRD.

3.3.4 RGO-2 and RGO-2_1700

The data displayed for RGO-2 and RGO-2_1700 were published on polymer [51].

Morphology

In untreated RGO-2, a highly expanded accordion-like structure is visible (Figure 20a,b), consisting of randomly aggregated wrinkled and folded sheets in a three dimensional porous architecture. As for RGO, an accurate measurement of the thickness of the visible RGO-2 is not possible in these conditions. Therefore, flakes thickness was only estimated to be in the range of a few nm. As observed for RGO, the annealing process at 1700°C did not significantly alter the morphology, structure or apparent thickness of the graphite nanoplatelets (Figure 20c,d).

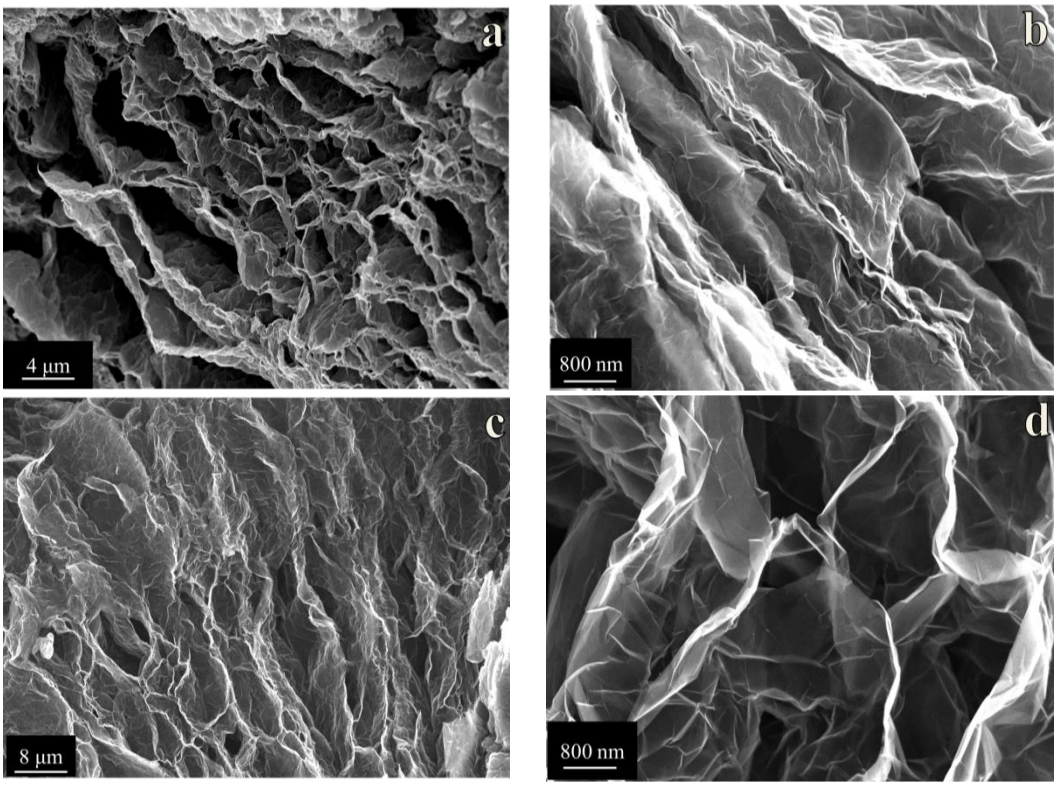

Figure 20. High magnification and low magnification FESEM micrographs for RGO-2 (a and b) and RGO-2_1700 (c and d)

Raman spectroscopy

Similarly to what observed for RGO (Figure 16), Raman spectrum of pristine RGO-2 (Figure 21) shows an intense D band at ~1345 cm^{-1}, with intensity comparable to the G band. Indeed, an I_D/I_G ratio of ~ 0.8 was calculated. It is

worth noting that deconvolution of the first-order Raman fingerprint for RGO-2 requires the addition of a further band located at ~1521 cm^{-1} which was previously ascribed to highly disordered areas [175] or to amorphous carbon [150]. The second-order Raman spectrum was characterized by a very weak G' mode, consisting of a wide band at ~2700 cm^{-1} and a reliable fitting with multiple peaks was not feasible. In conclusion, based on the I_D/I_G ratio and the overall features of the Raman spectra, a high concentration of defects was clearly evidenced in the sp^2 structure for RGO-2 [149, 150]. After thermal annealing at high temperature dramatic changes in Raman spectrum were observed. The G band shrinks and increases its intensity upon high temperature treatment, while the D band becomes very weak. Indeed, RGO-2_1700 the ID/IG ratio was calculated as ~0.11, *i.e.* 7 times lower than I_D/I_G calculated for pristine RGO-2. Furthermore, the second-order spectrum of annealed RGO-2 shows a narrower and more intense G' peak at ~2705 cm^{-1}, similar to G' observer for RGO_1700 (Figure 16).

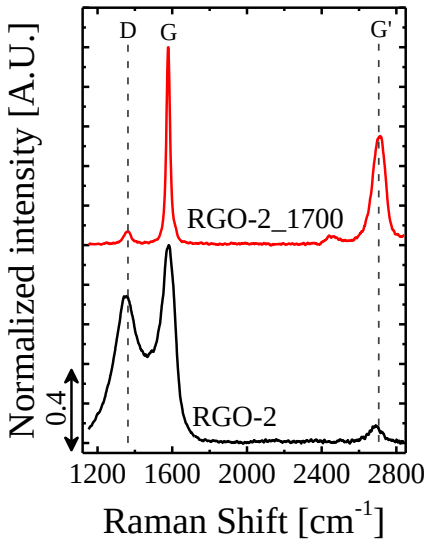

Figure 21. Representative Raman spectra for RGO-2 and RGO-2_1700.

XPS

XPS analysis was used to study the chemical composition of the flakes before and after annealing. Indeed, from integration of survey scan peaks, in pristine RGO-2, the oxygen content was calculated ~ 7.0 at.%. To further analyze the

chemical composition of RGO-2, narrow scans on C_{1s} (B.E. ≈ 285 eV) and O_{1s} (B.E. ≈ 530 eV) signals were collected and deconvolved (Figure 22a,b). Reliable fitting of C_{1s} band for RGO-2 was performed with six peaks: 284.5 eV (sp^2 C-C carbon), 285.0 eV (sp^3 C-C carbon), 286.0 eV (C-OH/C-O-C), 287.0 eV (C=O), 288.5 eV (O=C-OH) and 291.1 eV (π-π^* shake-up). Based on the deconvolution carried out, a high content of sp^3 C-C carbon was estimated (~ 25% of C_{1s} peak area), in good agreement with the results obtained by Raman spectroscopy (Figure 21), further suggesting the presence of high content of disordered carbon [176]. The O_{1s} signal of RGO-2 exhibited two partially overlapping peaks: a simple deconvolution was preferred, with two peaks centered at 531.4 eV (double-bonded oxygen) and 533.6 eV (single-bonded oxygen), in accordance with fitting of C_{1s} peak.

The thermal treatment at 1700°C drastically modified RGO-2, leading to ~ 1.1 at.% oxygen content. The XPS C_{1s} and O_{1s} bands of RGO-2_1700 (Figure 22c,d) exhibit significantly changes respect to pristine RGO-2. In fact, it is clearly visible a decrease of the relative intensity of almost all the oxidized groups. Furthermore, the FWHM of sp^2 C-C was reduced from 0.77 eV down to 0.65 eV and the content of sp^2 carbon increased from ~ 52% up to ~64% upon thermal annealing. It is worth observing that the sp^3 carbon content was reduced down to ~ 17 % (respect to ~ 25% calculated for RGO-2). Analysis on O_{1s} band reveals a weak signal, which was fitted with only one Lorentzian-Gaussian centered at 532.3 eV, related to single bonded C-O mainly in the form of phenolic groups, as already observed for RGO_1700.

Based on these results, and on those reported for RGO (and RGO_1700), it appears that during annealing at 1700°C a dramatic evolution of RGO-2 structure occurred, especially with the recovery or elimination of highly defective regions on the nanoflakes.

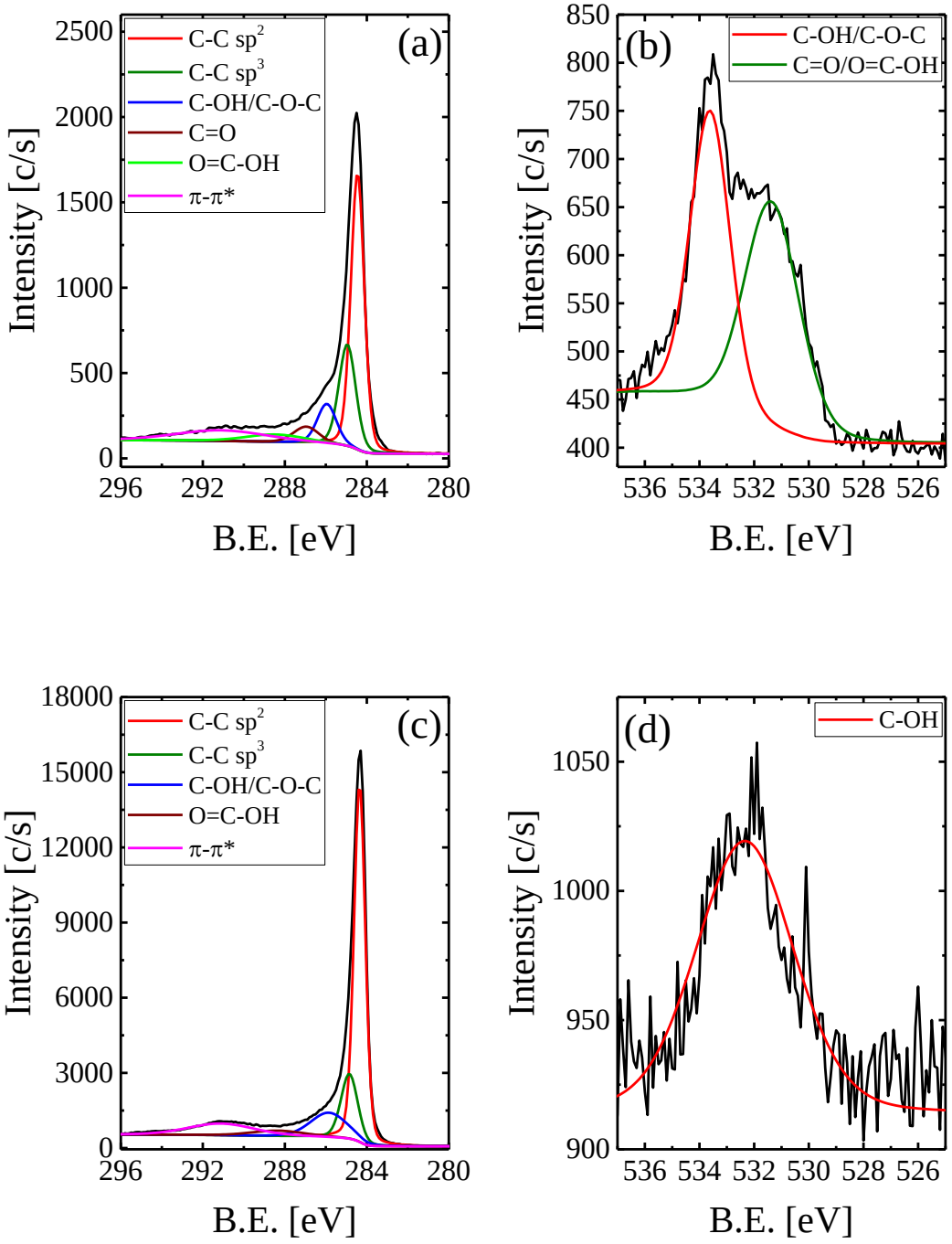

Figure 22. XPS curves with their deconvolution peaks for (a) C1s and (b) O1s of RGO-2 and (c) C1s and (d) O1s of RGO-2_1700. For all the spectra, the black line indicates raw data.

TGA

Thermal stability of RGO-2, before and after the thermal treatment at 1700 °C, was evaluated by TGA in air (Figure 23) to indirectly investigate their structural features. TGA thermogram for RGO reveals two degradation steps: in the first step, RGO-2 lose about 66 wt.% in the range 400 ÷ 620 °C with the maximum mass loss rate centered at ~ 550 °C. Such poor thermal stability could be related to small and highly defective nanoflakes with presence of partially amorphous carbon [177], as observed by Raman spectroscopy. The second degradation step occurred in the range 620 ÷ 800 °C, with a further mass loss of ~ 23 wt.% and the maximum centered at ~ 709°C, thus indicating a limited fraction of relatively stable flakes. After annealing, the T_{onset} shifts to ~ 671 °C and the maximum of mass loss rate at ~ 777 °C. This indicates a high thermal stability obtained with the thermal treatment, probably related to the elimination of the poorly thermal stable phase.

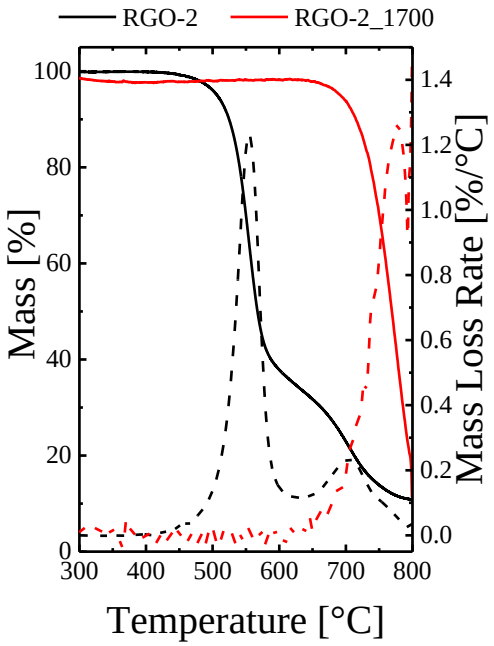

Figure 23. Mass vs. temperature (solid lines) and Mass loss rate vs. temperature (dashed lines) plots for RGO-2 and RGO-2_1700.

Chapter 4

Effect of morphology and defectiveness of graphene-related materials on the electrical and thermal conductivity of their polymer nanocomposites.

Despite the aim of this thesis is the exploitation of melt reactive processes for the polymerization of oligomers premixed with GRM into polymer/GRM nanocomposites, in the first part of the thesis comparison of the properties of pCBT/GRM nanocomposites prepared by simple melt mixing, solvent-assisted mixing and polymerization during melt-mixing was carried out. Results obtained in terms of nanocomposites dispersion and properties obtained with the different preparation methods are described in the first part of this chapter, demonstrating clear advantages from polymerization during melt mixing, compared to conventional nanocomposite processing.

In the second part, poly (butylene terephthalate) nanocomposites were prepared by polymerization during melt mixing, in presence of different types of graphene-related materials, to investigate the effect of nanoparticles feature on the properties of nanocomposites. One type of graphite nanoplatelets (GNP) and two

different grades of reduced graphene oxide (rGO) were used. Furthermore, high temperature annealing treatment under vacuum at 1700°C was carried out on both RGO to reduce their defectiveness and study the correlation between the electrical/thermal properties of the nanocomposites and the nanoflakes structure/defectiveness. Thermal, mechanical and electrical properties of the nanocomposites were investigated by means of rheology, dynamic mechanical thermal analysis, volumetric resistivity and thermal conductivity measurements. Physical properties of nanocomposites were correlated with the structure and defectiveness of nanoflakes, evidencing a strong dependence of properties on nanoflakes structure and defectiveness. In particular, a significant enhancement of both thermal and electrical conductivities was demonstrated upon the reduction of nanoflakes defectiveness.

4.1 Comparison between the different processing techniques

In this first part, a brief comparison on the properties of pCBT + 5 wt.% RGO nanocomposites prepared by simple melt mixing (labeled pCBT + RGO_MM), solvent-assisted mixing (labeled pCBT + RGO_SA) and in-situ polymerization (labeled pCBT + RGO_IS) is reported. Preparation methods are described in Chapter 2.

Morphology

The morphology of the different nanocomposites was investigated by means of scanning electron microscopy on cryofractured samples. Low magnification images (Figure 24a,c,e) showed interesting differences between the different preparation methods. Indeed, while for the nanocomposites prepared by solvent-assisted mixing and *in-situ* polymerization an almost uniform fractured surface was observed, in pCBT + RGO_MM (Figure 24e) nanoflake aggregates (~ 20 μm lateral size) were observed over the whole fractured surface, thus indicating the poor dispersion and distribution obtained through simple melt-mixing. High magnification micrographs showed homogenous distribution of nanoflakes, with a lateral size in the order of few micrometers, for both pCBT + RGO_IS (Figure 24b) and pCBT + RGO_SA (Figure 24d), whereas in pCBT + RGO_MM (Figure S3f) a very limited number of micro-sized nanoflakes is visible, likely due to the poor disaggregation of RGO nanoflakes. These results suggest that direct melt mixing is not able to disaggregate RGO expanded structure, leading to a limited dispersion and distribution of nanoflakes. On the other hand, pre-infiltration of

oligomers or polymer chains into the galleries of the expanded rGO structure was demonstrated to result in an efficient dispersion and distribution of rGO nanoflakes during reactive mixing.

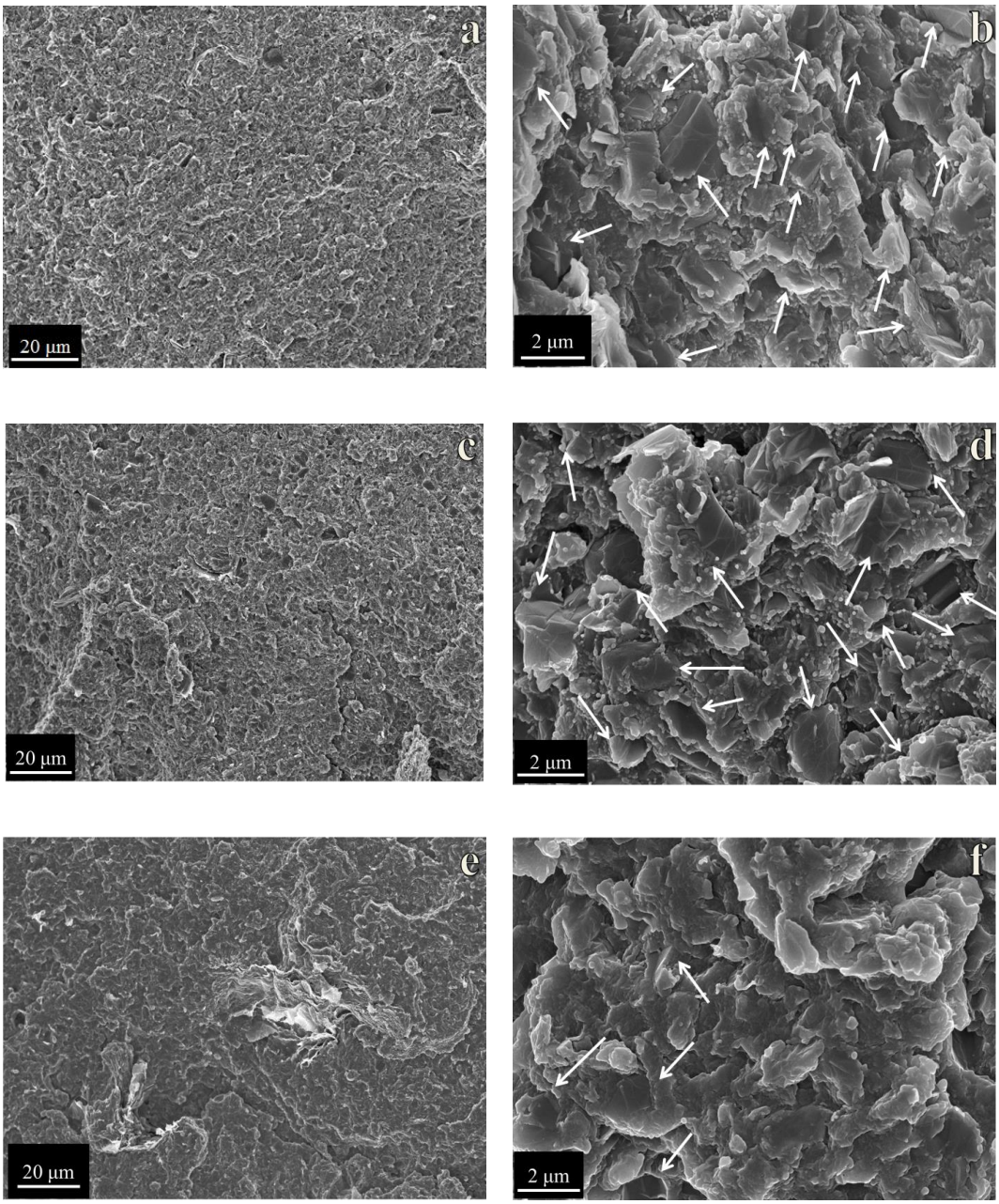

Figure 24. Electron microscopy micrographs at low and high magnification for (a,b) pCBT + RGO_IS, (c,d) pCBT + RGO_SA and (e,f) (PBT+RGO)_MM. White arrows in high magnification micrographs indicate nanoparticles.

Electrical and thermal conductivity results

To further evaluate the effect of the different mixing methods on the nanocomposite properties, electrical and thermal conductivity were measured (Table 5) on the nanocomposites prepared by the different methods. Both pCBT nanocomposites prepared by pre-infiltration of oligomers or polymer chains into the galleries of the expanded rGO structure exhibit electrical conductivity values in the order of ~ 10^{-4} S m^{-1}. On the other hand, melt mixing led to nanocomposite with an electrical conductivity value about one order of magnitude lower respect to those measured for the other pCBT + RGO nanocomposites. Furthermore, pCBT + RGO_MM exhibits the lowest enhancement in the thermal conductivity (~ 50% increase respect to the value measured for pristine pCBT, *i.e.* 0.24 W m^{-1} K^{-1}), whereas ~ 90 and 114% thermal conductivity enhancement were measured for pCBT + RGO_SA and pCBT + RGO_IS, respectively.

Table 5. Electrical and thermal conductivity for pCBT + 5wt.% RGO prepared through different mixing procedures.

Material	σ [S m^{-1}]	λ [W m^{-1} K^{-1}]
pCBT + RGO_IS	(1.5 ± 0.4) E-4	0.515 ± 0.004
pCBT + RGO_SA	(3.2 ± 1.1) E-4	0.454 ± 0.004
pCBT + RGO_MM	(2.4 ± 0.2) E-5	0.367 ± 0.001

SEM observation and thermal/electrical conductivities are therefore consistent in demonstrating the need to infiltrate oligomers or polymers, via solvent processing, to allow a proper dispersion of nanoflakes, which in turn results in higher conduction performance. However, nanocomposites prepared through ring opening polymerization exhibited slightly higher thermal conductivity respect to that prepared by solvent assisted mixing. This could be ascribed to a further separation of nanoflakes occurring during polymerization of CBT into pCBT, which is one of the goals of chapter 5. In both cases, the need to pre-infiltrate oligomers or polymers requires solvent to be used. However, these solvents are clearly different between pCBT (Chloroform/HFIP 1/1 vol/vol) and CBT (Acetone): from the sustainability point of view, the use of non-halogenated solvents is clearly preferable, thus further supporting for the preference in using

pre-infiltration of CBT followed by polymerization during melt compounding. Furthermore, processing of graphene-related materials with oligomers may allow for the preparation of unpolymerized masterbatches, which can be further compounded with PBT and polycarbonate through transesterification reaction, thus indicating a higher flexibility in the exploitation of CBT oligomers rather than PBT.

4.2 Melt reactive mixing

In this section, the effect of exploiting one GNP, two types of rGO and the same rGO annealed, at 1700°C for 1h in vacuum, on mechanical, thermal and electrical properties is addressed.

Differential scanning calorimetry

The polymerization of CBT into pCBT was monitored by differential scanning calorimetry. DSC plots for CBT, pCBT and pCBT nanocomposites are reported in Figure 25. Pure CBT exhibits an exothermic peak at about 80°C, which corresponds to a cold crystallization, and three separated endothermic peaks at about 125, 155, and 188°C due to the melting of CBT oligomers with different chain lengths. After extrusion of oligomers in presence of the tin catalyst, no traces of the characteristic melting peaks of CBT were observed, thus indicating conversion of CBT into pCBT. It is noteworthy that the absence of CBT melting peaks is not sufficient to prove 100% conversion of CBT; however, conversion up to 97% were reported in literature when CBT were polymerized in similar conditions (205°C, 3 min, in presence of the same catalyst used in this work) [146]. After polymerization, pure pCBT exhibits two partially overlapping endothermic peaks at 218.8 and 226.4°C, respectively, during heating. This is a well-known behavior for pCBT and the peak at lower temperatures is related to thin crystals which melt and recrystallize, forming thicker crystals that re-melt again at higher temperatures [178]. The degree of crystallinity of pristine pCBT was calculated equal to 41.7%. As observed for other polymer/GRM nanocomposites [93, 113, 117], the addition of the different GRM affected pCBT crystallization, with the formation of thicker crystals which exhibited only one melting peak in second heating scans. The addition of 5 wt.% of nanoflakes induced a slight reduction in the crystallinity degree of pCBT with values ranging between 34.4% and 40.9% (Table 6).

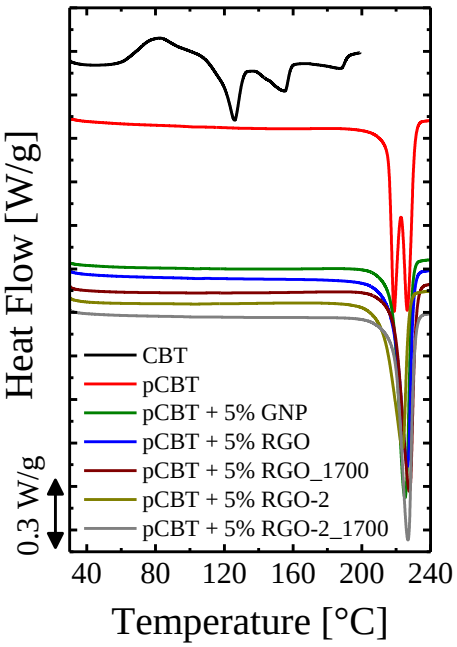

Figure 25. DSC curves on heating (10°C/min) for CBT, pCBT and its nanocomposites

Table 6. Crystallinity degree of pCBT and its nanocomposites

Material	Crystallinity degree [%]
pCBT	41.7
pCBT + 5% GNP	40.0
pCBT + 5% RGO	38.0
pCBT + 5% RGO_1700	39.4
pCBT + 5% RGO-2	34.4
pCBT + 5% RGO-2_1700	40.9

4.2.1 Nanoparticle organization

Morphology

The morphologies of pCBT nanocomposites were studied by electron microscopy: representative micrographs of pCBT + 5 wt.% nanoflakes are reported in Figure 26. Both nanocomposites containing GNP and rGO exhibit a good distribution of nanoflakes with some differences in the morphology. In pCBT + 5% GNP (Figure 26a) relatively large and thick nanoflakes are observed, reflecting the morphology of the starting graphite nanoplatelets (Figure 7a). In nanocomposites containing RGO (Figure 26b) and RGO-2 (Figure 26d) smaller and thinner flakes are observed, suggesting separation and dispersion of the nanometric layers from accordion-like structure. Distribution and dispersion of nanoflakes do not seem to be affected by the thermal treatment as no significant differences are observed between the morphologies of nanocomposites containing pristine (Figure 26b,d) and annealed rGO (Figure 26c,e).

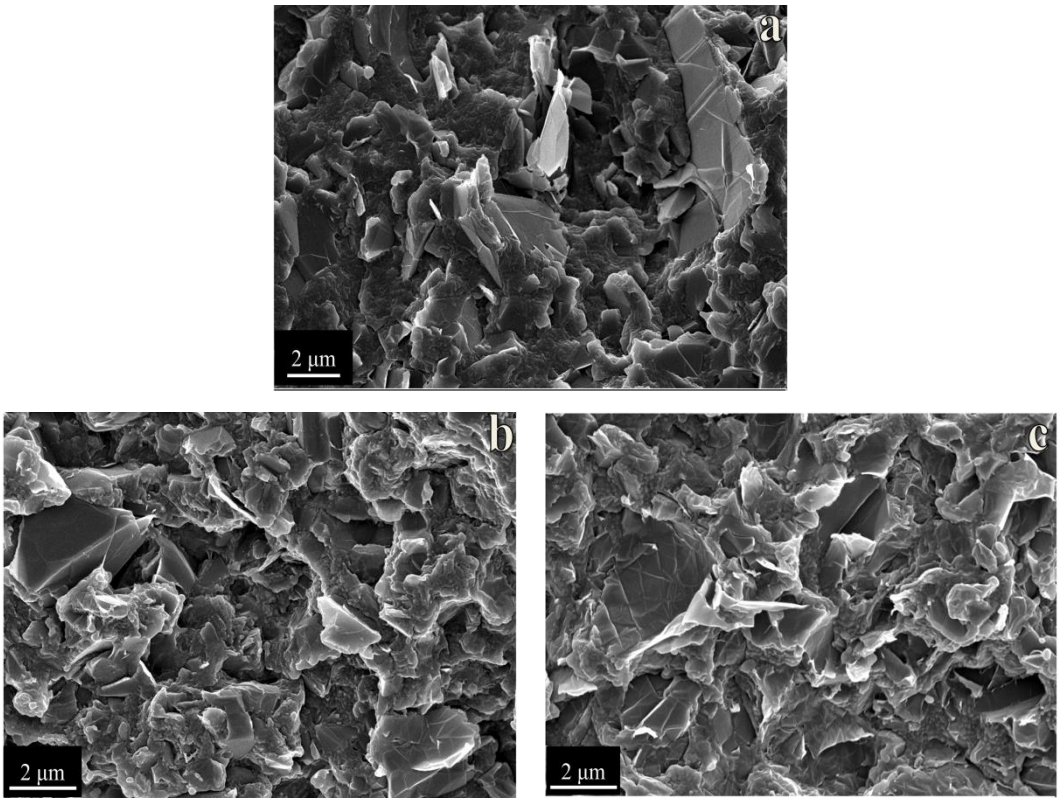

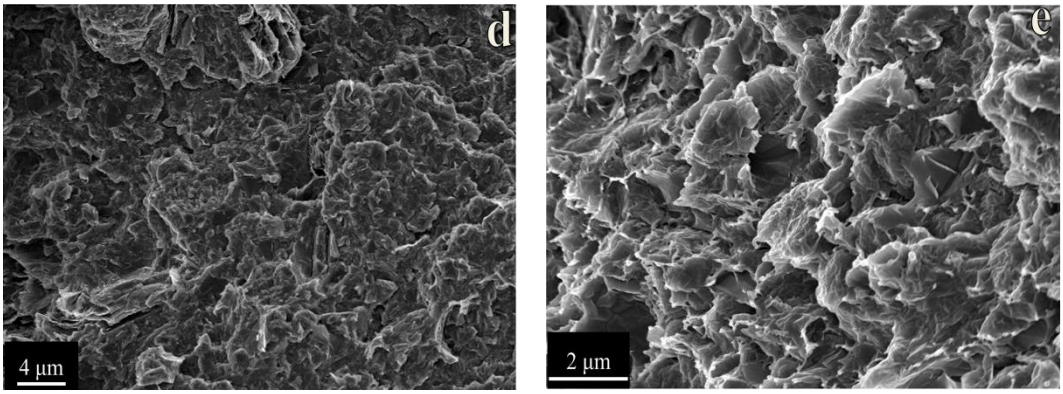

Figure 26. FESEM pictures for pCBT nanocomposites containing 5 wt.% of a) GNP, b) RGO, c) RGO_1700, d) RGO-2 and e) RGO-2_1700.

Rheology

To further evaluate the dispersion of nanoflakes in the polymer and their organization into a percolating network, linear viscoelasticity in the molten state was studied performing dynamic frequency sweep tests. Indeed, elastic modulus (G') and complex viscosity η* are well known to be sensitive to the filler content and dispersion [179], thus providing indirect information on the nanoparticles organization in the polymer bulk. G' and η* plots for pCBT + 5% nanoflakes are reported in Figure 27 as a function of deformation frequency. Pure pCBT exhibits the classical behavior of polymers in linear regime, showing G' decrease as the frequency decreases while η* is approximately constant (~ 10^2 Pa s) in the whole frequency range (Figure 27b). On the contrary, for all the nanocomposites, G' exhibits a weak dependency on the frequency in the whole range, evidencing the formation of a solid-like network [99, 180], *i.e.* a well-organized percolated structure of the nanoflakes. A further evidence for the high percolation degree of nanoflakes in the nanocomposites is provided by the strong dependence of the complex viscosity with frequency [179], extending over four decades (Figure 27b). Comparing the elastic modulus and viscosity plots for the different nanocomposites, significant differences can be observed. In the case of GNP, clearly lower values for both G' and η* were observed compared with rGO. This reflects the different size of dispersed particles, evidencing for a relatively loose yet percolating network structure. Among nanocomposites containing reduced graphene oxides, differences are clearly visible between pCBT + 5% RGO and pCBT + 5% RGO-2, the latter evidencing a significantly more organized percolation network. However, when using annealed rGO, both nanocomposites exhibited very similar modulus and viscosity plots.

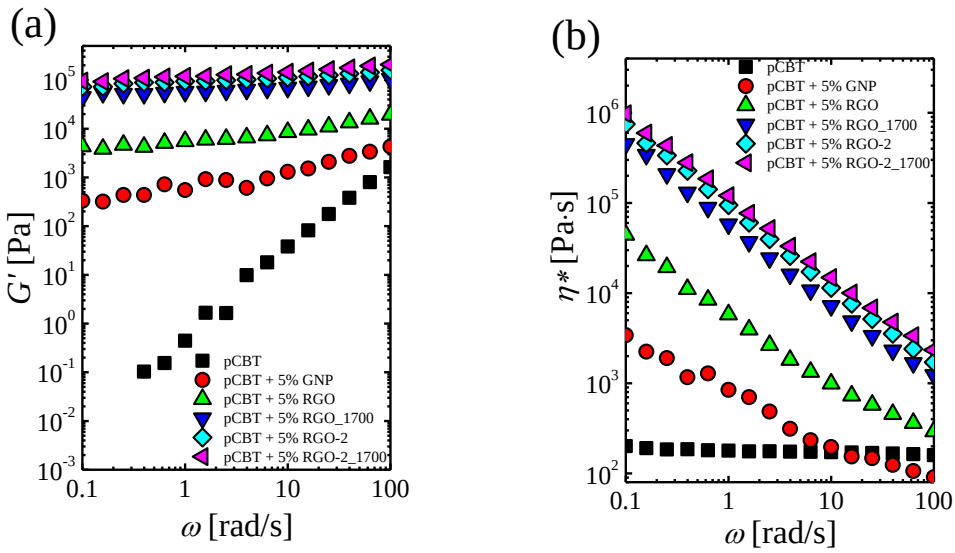

Figure 27. Dynamic frequency sweep test at 250°C for pCBT and its nanocomposites. (a) G' and (b) complex viscosity as a function of the angular frequency

4.2.2 Mechanical properties

DMTA

The organization of nanoflake into a percolated network and its effect on viscoelastic properties of the nanocomposites was further studied in the solid state by dynamo-mechanic analysis. DMTA was used to evaluate the effect of the different nanoflakes on either storage modulus and glass transition temperature of pCBT and its nanocomposites (Figure 28). The inclusion of nanoflakes was found to strongly increase the storage modulus over the whole temperature range explored, which is consistent with the formation of a stiff network of nanoflakes, with limited differences between GNP and the different rGO. The temperature for the main relaxation of the polymer, measured as the peak of Tanδ plot, is generally increased and /or broadened (Table 7) by the presence of GNP or rGO, compared to the reference pCBT, suggesting confinement of the polymer chains induced by the presence of dispersed nanoflakes.

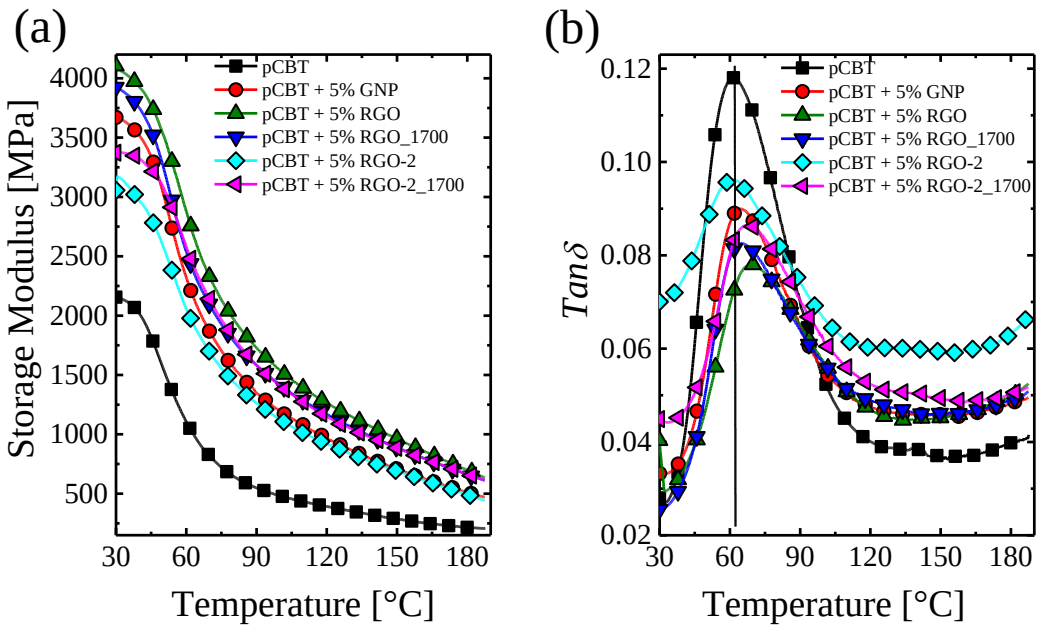

Figure 28. (a) Storage modulus and (b) tan delta plots measured by DMTA

Table 7. Tanδ peak and FWHM for pCBT and its nanocomposites

Material	T_{peak} [°C]	FWHM [°C]
pCBT	61.5	41.6
pCBT + 5% GNP	64.5	41.8
pCBT + 5% RGO	68.4	52.6
pCBT + 5% RGO_1700	64.9	53.8
pCBT + 5% RGO-2	61.3	42.2
pCBT + 5% RGO-2_1700	67.5	42.0

4.2.3 Electrical conductivity

While pure pCBT shows a very low electrical conductivity, in the range of 10^{-13} S m^{-1} which is typical for insulating materials [105, 181], the formation of a percolation network with conductive nanoflakes is clearly expected to result in an electrically conductive material. Indeed, graphene and graphene related materials are good candidates for the improvement of electrical properties of polymeric materials, provided a good dispersion is obtained and the quality of the nanoflakes is sufficient to maintain a high charge mobility [182]. A sharp transition from insulating to conductive materials is typically associated to the percolation threshold, which clearly depends on both the dispersion degree and the nanoflakes aspect ratio: for pCBT mixed with RGO and GNP values ranging between 1.6 wt.% [181] and 5 wt.% [105] were measured, respectively.

Electrical conductivity results for pCBT nanocomposites in this chapter (Figure 29, Table 8) clearly confirmed that all nanocomposites prepared at 5 wt.% loading are above the percolation threshold, with conductivity values in the range of 10^{-5} S m^{-1} for GNP and between 10^{-4} S m^{-1} and 10^{-2} S m^{-1} with the different rGO. The difference between GNP and rGO has to be ascribed to the lower density of the percolation network obtained with graphite nanoplatelets, in agreement with rheology results discussed above, and to the higher aspect ratio of rGO, which was reported to affect the electrical conductivity of polymer/GRM nanocomposites [93, 110]. Furthermore, large differences were observed between nanocomposites containing different grades of rGO. In particular, both RGO-1700 and RGO-2_1700 are more effective in improving electrical properties, compared to the corresponding nanocomposites containing pristine RGO and RGO-2. Taking into account the minor differences in dispersion of annealed *vs.* pristine rGO, described above on the basis of electron microscopy, rheology and viscoelastic properties, the electrical conductivity results here reported evidence the strong effect of the reduction of nanoflake defectiveness on their intrinsic electrical conductivity and, in turn, on the electrical conductivity of their relevant polymer nanocomposites.

Further enhanced electrical conductivity was progressively obtained with increasing the nanoflake loading, as summarized in Figure 29. However, it is worth mentioning that the loading of nanoflakes which can be included in pCBT by melt blending is limited by the viscosity of the nanocomposite obtained. While in the case of GNP the increase of viscosity was limited and loading up to 30 wt.% did not cause processing problems, extremely high viscosities were obtained

during polymerization at 10 wt.% loading of the different rGO and preparation of pCBT + 10% RGO-2 was not possible in the conditions used for the other preparations. Even with these limitations, the analysis of conductivity results at higher loading clearly confirms that efficiency in electrical conductivity enhancement is maximum for thermally annealed RGO and minimum for GNP. Electrical conductivity values in the range of 10^{-1} S m^{-1} were obtained for pCBT + 10% RGO_1700 (0.09 ± 0.01 S m^{-1}) as well as for pCBT + 30% GNP (0.19 ± 0.004 S m^{-1}), the different loading to obtain similar electrical performance evidencing for superior properties of low defectiveness RGO.

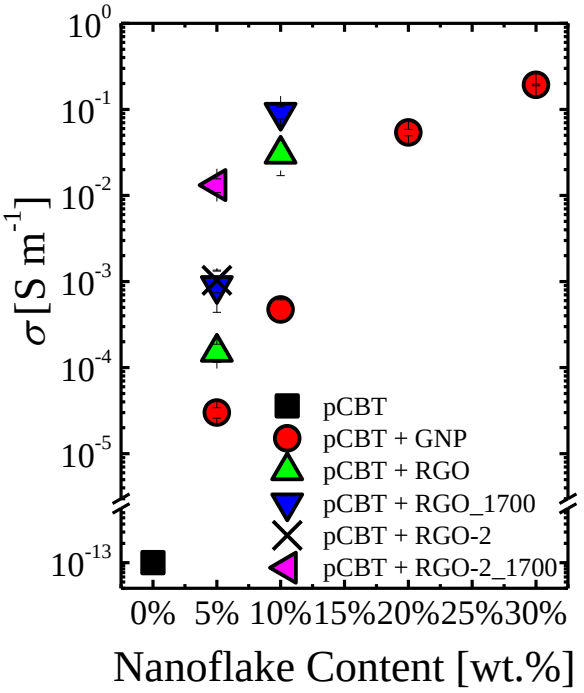

Figure 29. Electrical conductivity vs. nanoflake content. The value here reported for pure pCBT was taken from ref. [105]

Table 8. Electrical conductivity data for pCBT nanocomposites

	Electrical conductivity [S m^{-1}]			
Material	5 wt.%	10 wt.%	20 wt.%	30 wt.%
pCBT + GNP	(3.0 ± 0.4) E-5	(4.7 ± 1.4) E-4	(5.4 ± 0.5) E-2	(1.9 ± 0.1) E-1
pCBT + RGO	(1.5 ± 0.4) E-4	(3.0 ± 1.3) E-2	-	-
pCBT + RGO_1700	(9.0 ± 4.6) E-4	(9.2 ± 1.5) E-2	-	-
pCBT + RGO-2	(1.0 ± 0.3) E-3	-	-	-
pCBT + RGO-2_1700	(1.3 ± 0.2) E-2	-	-	-

4.2.4 Thermal conductivity

Bulk thermal conductivity results for pCBT and its nanocomposites with GNP and rGO as a function of filler content are reported in Figure 30 and Table 9. Addition of 5 wt.% of GNP or pristine rGO led to thermal conductivity values, in the range of 0.5 W m^{-1} K^{-1}, that is corresponding to about twice the conductivity of pCBT, 0.240 ± 0.003 W m^{-1} K^{-1}. It is well known that this increase is clearly not comparable with the jump in electrical conductivity associated to the percolation threshold. Two different reasons are generally agreed upon as an explanation for this feature. On the one hand, the thermal conductivity ratio between carbon nanoflakes and polymers is in the range of 10^3-10^4, thus much lower than for electrical conductivity (ratio of 10^{12}-10^{15}). On the other hand, the simple physical contact between two particles (mechanical percolation) may be sufficient to allow an electron to hop between particles close enough, but it is indeed insufficient to allow efficient phonon transfer [1]. It is worth noting that thermal conductivity of pCBT + 5% GNP is slightly higher than for both pCBT + 5% RGO and pCBT + 5% RGO-2. This result may appear surprising based on the particles dispersion and electrical conductivities described above, but it can be explained taking into account the high degree of defectiveness in rGO, which was previously demonstrated to strongly affect their intrinsic thermal conductivity [35]. Indeed, when annealed nanoflakes were used, the value of thermal conductivity obtained

were 0.890 ± 0.009 and 0.995 ± 0.003 W m^{-1} K^{-1} for pCBT + 5% RGO_1700 and pCBT + 5% RGO-2_1700, respectively, *i.e.* about twice the value obtained for untreated rGO at the same loading. This dramatic increase is clearly related to the rGO structural evolution upon high temperature annealing, described in chapter 3, and evidences experimentally for the first time the correlation between the defectiveness of the rGO nanoflakes and the thermal conductivity of the relevant nanocomposites. Nanocomposites with 10 wt.% of nanoflakes exhibit higher thermal conductivities with a maximum value of 1.772 ± 0.003 W m^{-1} K^{-1} for RGO_1700, *i.e.* about three times the conductivity of pCBT + 10% RGO, thus further confirming the effect of rGO thermal annealing on nanocomposites conductivity. At 10% loading, nanocomposites containing GNP displayed a thermal conductivity between that of RGO and RGO_1700 at the same loading. However, while maximum rGO content is limited by its difficult processability, nanocomposites with higher loading of GNP can be prepared, taking advantage of its moderate effect on melt viscosity, leading to further thermal conductivity increase with the amount of GNP, up to 2.49 ± 0.02 W m^{-1} K^{-1} at 30 wt.% loading. About equivalent thermal properties were found for pCBT + 10% RGO_1700 and pCBT + 20% GNP, [1.772 W m^{-1} K^{-1} and 1.827 W m^{-1} K^{-1} respectively], which would suggest the two materials can be considered alternatives in thermal management applications. However, from a practical point of view, the choice between nanocomposites embedding of GNP at high loading or rGO at lower loading is a matter of other properties beyond the bare values of thermal or electrical conductivities, including for instance density of the material, brittleness and impact resistance as well as processability, recyclability and cost. Furthermore, despite the clear advantages associated with rGO annealing at high temperature, the additional energy input for the additional process has to be taken into account when considering the transfer of the present results to an industrial application. Therefore, while thermal annealing remains a powerful method to boost thermal properties, further efforts remain necessary for the development of efficient large-scale production of low defectiveness carbon nanoflakes.

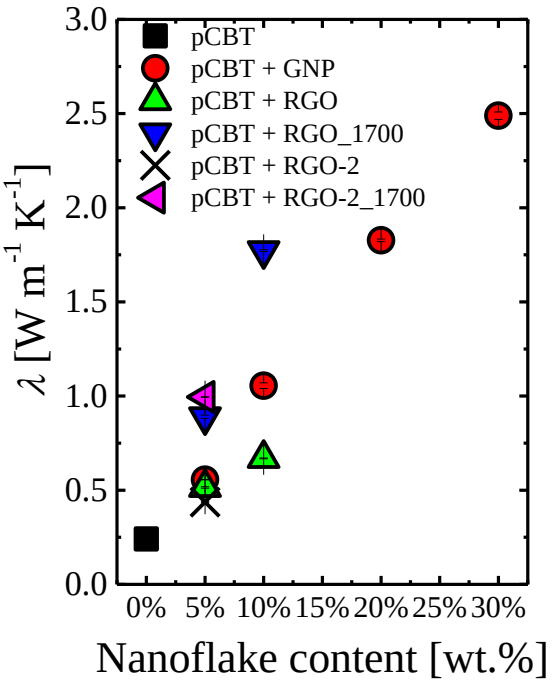

Figure 30. Thermal conductivity vs. nanoflake content

Table 9. Thermal conductivity data for pCBT nanocomposites. The experimental error in the measured values is below 1% for all the nanocomposites

	Thermal conductivity [W m^{-1} K^{-1})]			
Material	5 wt.%	10 wt.%	20 wt.%	30 wt.%
pCBT + GNP	λ ≈ 0.556	λ ≈ 1.005	λ ≈ 1.827	λ ≈ 2.489
pCBT + RGO	λ ≈ 0.515	λ ≈ 0.669	-	-
pCBT + RGO_1700	λ ≈ 0.890	λ ≈ 1.772	-	-
pCBT + RGO-2	λ ≈ 0.437	-	-	-
pCBT + RGO-2_1700	λ ≈ 0.995	-	-	-

Summarizing electrical and thermal conductivity results for pCBT nanocomposites containing 5 wt.% of the different GRM (Figure 31) helps recognizing how the properties of nanoflakes directly affect thermal and electrical conductivity, with the higher enhancement in thermal and electrical conductivity provided by low defective and high aspect ratio nanoparticles. Furthermore, these results show that it is possible to tune the properties of the as prepared nanocomposites by selecting the proper nanoparticle. Indeed, exploiting GNP rather than one of the two pristine rGO leads to nanocomposites with a thermal conductivity in the order of 0.5 W m-1 K-1 but with differences of about two order of magnitude in the electrical conductivity, depending on the selected material property.

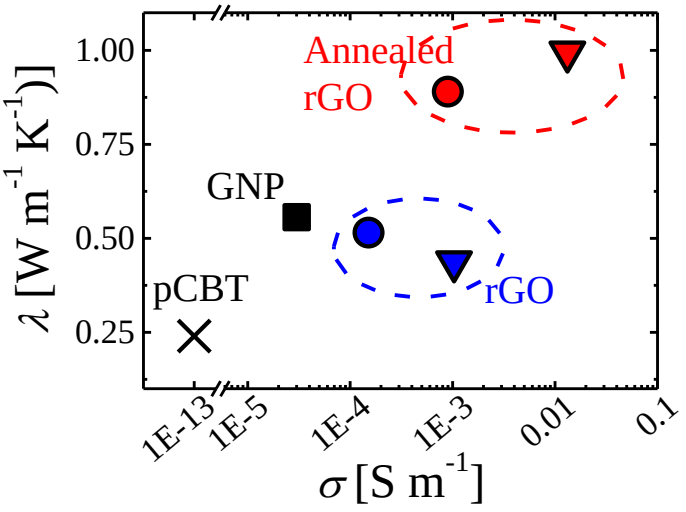

Figure 31. Thermal and electrical conductivity for pCBT + 5 wt.% GRM

4.3 Conclusions

pCBT + 5 wt.% RGO nanocomposites were prepared by exploiting different mixing methods: in-situ ring opening polymerization of CBT, solvent-assisted extrusion and simple melt mixing. Results showed limited dispersion and distribution of nanoflakes, reflected on poor electrical and thermal conductivity results, for pCBT + RGO prepared by simple melt mixing. On the other hand, nanocomposites prepared by pre-infiltration of oligomers or polymers, via solvent processing, into the expanded structure of RGO led to similar nanoparticle dispersion and distribution, and consequently similar electrical and thermal

conductivities. However, the dissolution of pCBT required the exploitation of low environmentally friendly solvents (Chloroform and HFIP), respect to CBT oligomers (Acetone), makes these lasts more interesting, especially for a future industrial exploitation. Furthermore the preparation of CBT/GRM masterbatches result in a more flexible process, considering the possibility to further mixing this masterbatch with PBT or PC, linking the oligomer chains directly on polymer chains through transesterification reaction.

Once the polymerization during melt mixing was assessed as the most promising method, CBT oligomers were *in-situ* polymerized into pCBT in the presence of graphite nanoplatelets or reduced graphene oxide. rGO obtained from different sources were used, both as received and after high temperature annealing to investigate correlation between the morphological/chemical features of carbon nanoflakes and the physical properties of their nanocomposites.

Melt mixing process in low viscosity CBT and subsequent polymerization in extrusion allowed homogeneous dispersion of nanoflakes in the polymer, as proven by electron microscopy and rheological analysis, which clearly provided evidences for a highly percolated structure. Significant differences were observed between nanocomposites containing GNP and rGO, in terms of denser percolation network (*i.e.* higher viscosity) obtained with thinner and smaller rGO nanoflakes compared to larger graphite nanoplatelets.

Electrical and thermal conductivity results showed interesting differences between nanocomposites with GNP and those embedding rGO, as well as between pristine and annealed rGO. The electrical conductivity results directly reflect the properties of the percolation network extrapolated by rheological analysis, the conductivity with rGO being significantly higher (up to two order of magnitude for RGO-2) compared to GNP. High temperature annealing of rGO further enhanced the electrical conductivity, leading to best result in the range of 10^{-1} S m^{-1} at 10 wt.%, which appears to be related to an improvement in charge mobility on the rGO rather than to differences in the percolation network obtained. Thermal conductivity enhancement was also found very different in the presence of GNP, rGO or annealed rGO. Comparison between nanocomposites with GNP and pristine rGO showed better thermal conductivity for GNP, which is in contrast with the electrical and rheological behavior. This result clearly evidence that the bare presence of a well-organized percolating network is not sufficient to obtain a high thermal conductivity of the composite and can only be explained taking into account the strong dependency of the thermal conductivity of the

carbon nanoflakes as a function of defectiveness. In nanocomposites containing rGO, nanoflakes defectiveness (oxidized carbons and other defects in the sp^2 structure) leads to a drop in their conductivity and, despite a well-organized percolation network was proved, the thermal conductivity performance is lower than for GNP-based nanocomposite, in which the percolation network is looser but nanoplatelets are significantly less defective. When comparing nanocomposites containing annealed vs. pristine rGO, a two- to three-fold increase in thermal conductivity was observed upon high temperature annealing of the rGO. This dramatic increase is clearly related to the reduction in rGO defectiveness rather than to differences in the percolation network. These results provide for the first time, to the best of the author's knowledge, experimental evidences of the correlation between the defectiveness of the rGO and the thermal conductivity of the relevant nanocomposites.

Chapter 5

Evolution of nanocomposite morphology and properties upon polymerization

In this chapter, the study of electrical and thermal conductivity before and after in-situ ring-opening polymerization of cyclic butylene terephthalate into poly (butylene terephthalate) in presence of graphene-related materials (GRM) is addressed, to gain insight in the modification of nanocomposites morphology upon polymerization. Nanocomposites are prepared with the same GRM used in the previous chapter. The aim of this chapter is to evaluate the properties of CBT and pCBT nanocomposites, in order to be able to develop and optimize reactive extrusion processing of pCBT nanocomposites, which may lead to enhanced properties.

5.1 Characterization

Differential scanning calorimetry

Differential scanning calorimetry was employed to monitor polymerization of CBT into pCBT and the effect of nanoparticles on melting/crystallization behavior of the polymer matrix. Melting signals of CBT/GRM nanocomposites (Figure 32a) reveal that nanoparticles do not have influence on CBT melting, with the presence of a small exothermic peak at about 80°C and three endothermic peaks

located at ~126, ~153 and ~186 °C which are typical for CBT [33]. Furthermore, this indicates that graphene related materials are not able to trigger ring opening polymerization of CBT and a catalyst is crucial to promote oligomer polymerization into pCBT; indeed 2nd heating curves on pCBT and pCBT/GRM (Figure 32c) show no traces of melting peaks of CBT, whereas a new endothermic peak at about 226 °C, related to the melting of the poly (butylene terephthalate), appeared for all the nanocomposites. The absence of CBT melting peaks is not sufficient to prove 100% conversion of CBT; however, conversion up to 97% were reported in literature when CBT were polymerized in similar conditions (205°C, 3 min, in presence of the same catalyst used in this work) [34]. The presence of GRM, drastically changes the crystallization behavior of CBT nanocomposites (Figure 32_b): while pure CBT exhibits only one broad exothermic peak (~85°C) during cooling ramp, CBT + GNP crystallizes with two peaks (~80 and ~111°C). On the other hand, all CBT/rGO nanocomposites are characterized by three crystallization peaks (with the three peaks in the range 66 ÷ 71°C, 87 ÷ 100°C and 115 ÷ 124°C) thus indicating splitting of the crystallization process into multiple peaks which is interpreted as the separated crystallization of the different oligomers, accordingly with their melting behavior described above. This suggests the nucleation activity of GRM is exerted preferentially on higher molecular weight fraction in the mixture of CBT. Nucleating effects by GRM were observed as well in pCBT nanocomposites, with a shift in the crystallization peak from ~199°C for pure pCBT to temperatures in the range 201°C to 211°C, depending on the GRM type (Figure 32_d).

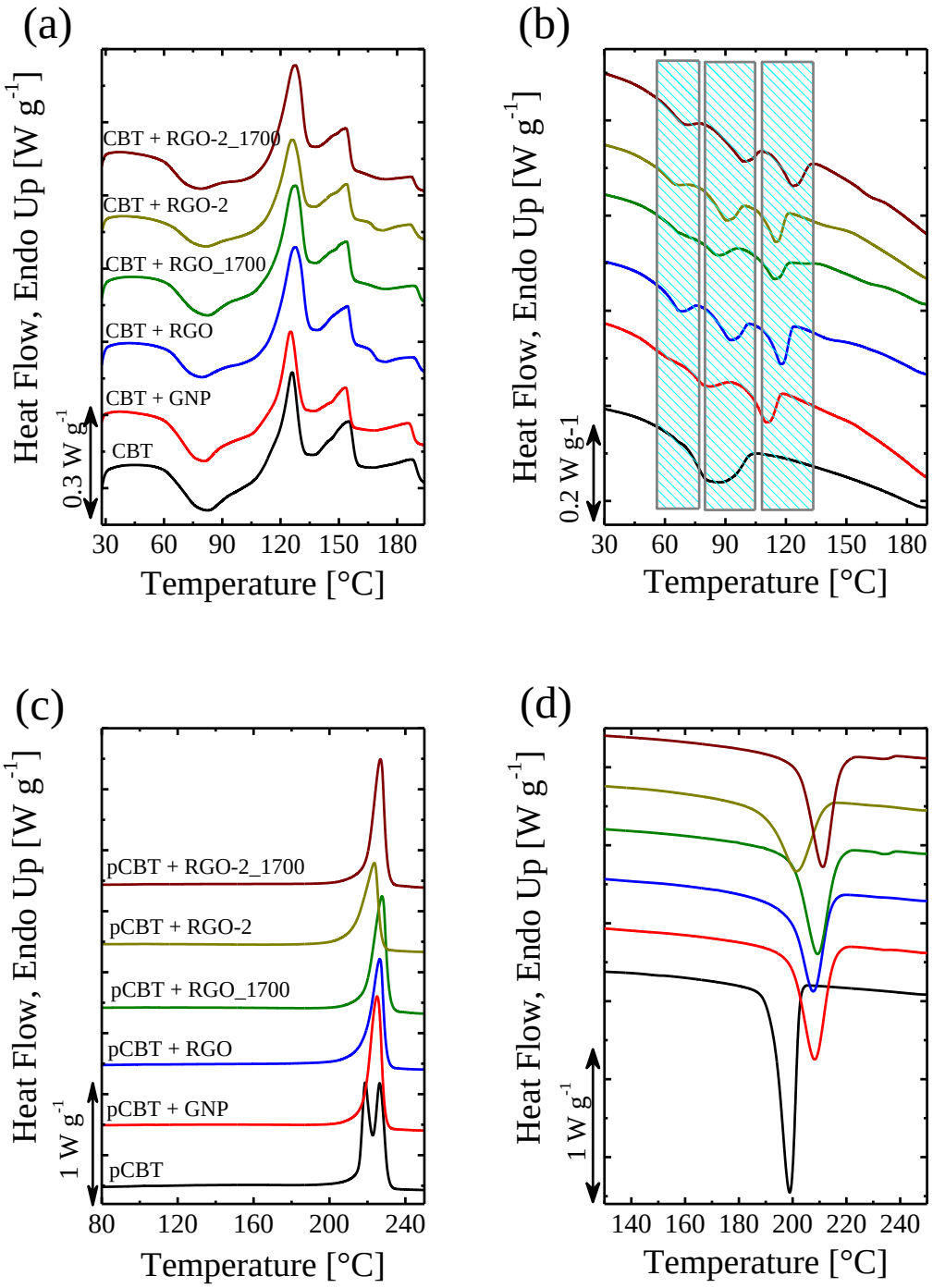

Figure 32. DSC results on CBT and pCBT nanocomposites: a) 2nd heating and b) cooling for CBT nanocomposites; c) 2nd heating and b) cooling for pCBT nanocomposites

5.1.1 Nanoparticle organization

Morphology

The morphologies of CBT and pCBT nanocomposites were investigated by electron microscopy: representative micrographs of CBT and pCBT nanocomposites containing GNP and rGO are reported in Figure 33. In CBT + 5% GNP (Figure 33a) it is possible to observe regions with large aggregates of nanoflakes, in the range of tens of microns, as well as other areas with a low or negligible content of nanoparticles. This is indeed expected for melt blending of aggregated nanoflakes into low molecular weight liquids, as the extremely low viscosity of CBT did not allow to apply sufficiently high shear forces during mixing to obtain optimal dispersion and distribution degree of nanoparticles. CBT/rGO nanocomposites at low magnification exhibit a better distribution of RGO aggregates (with average lateral size of few dozens of micrometers and average thickness ranging from few to ~ 20 μm) which could not be further separated due to the low viscosity of CBT. However, it is worth noting that low viscosity allows CBT to infiltrate the accordion-like structure of RGO (Figure 33c,e,g,i). While no clear differences were observed for GNP distribution and dispersion in pCBT (Figure 33b) and CBT (Figure 33a) nanocomposites, in pCBT + rGO nanoflakes (Figure 33d,f,h,j), aggregates were strongly reduced in number and size as compared to CBT + rGO, suggesting a dispersion effect obtained during the polymerization of CBT infiltrated into the accordion-like structure. This can be explained by the progressively increasing applied shear during melt mixing, owed to the viscosity increase during polymerization of CBT into pCBT [183], leading to a significant improvement in dispersion and distribution of nanoparticles. Further insight in the mechanisms of infiltration between nanoflakes and their separation during melt mixing were obtained comparing the above-described polymerization in the presence of rGO with the infiltration of pre-polymerized pCBT as well as with the direct melt blending of pCBT with rGO powder, as in the first part of Chapter 4.

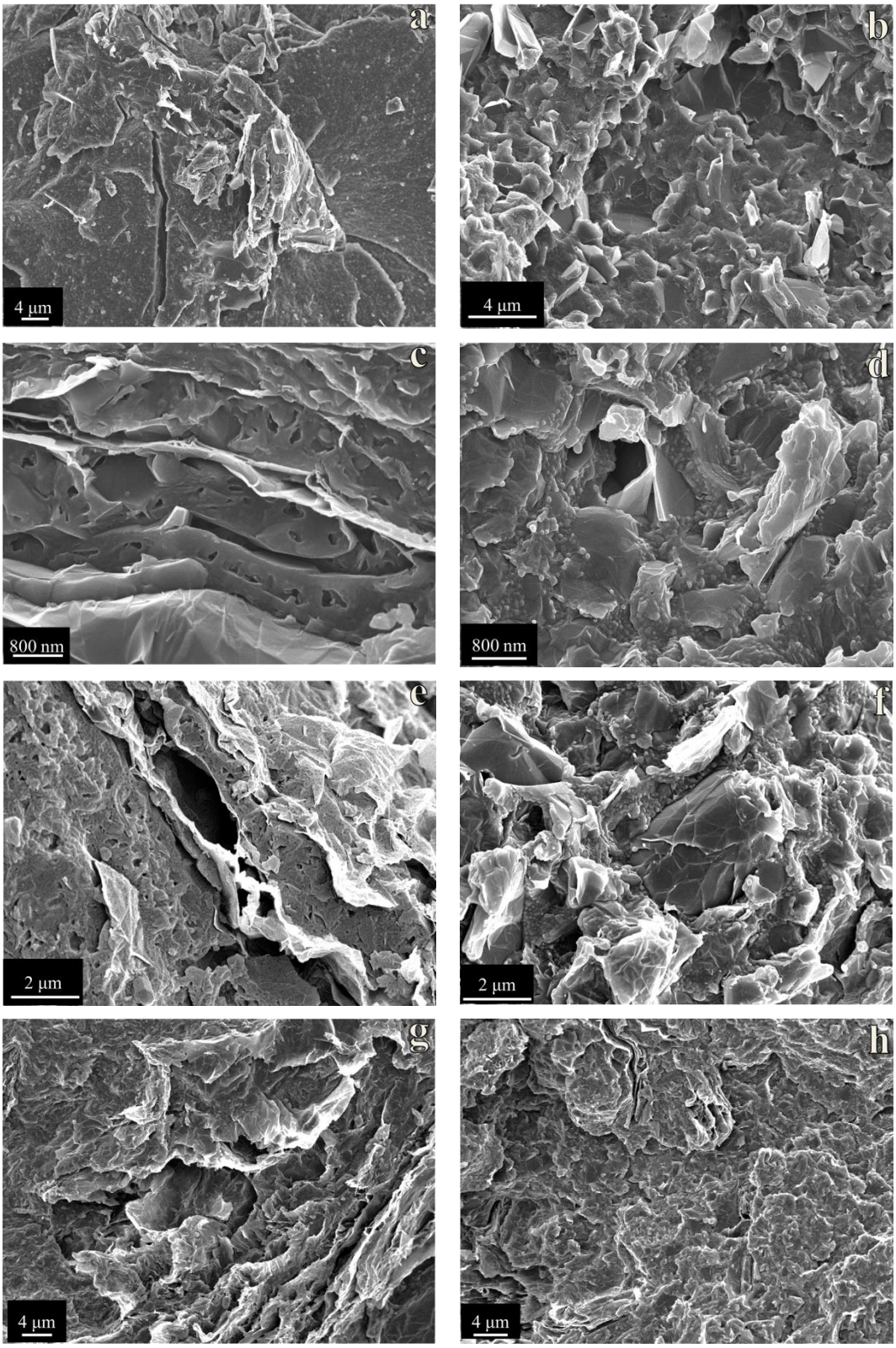
a
4 µm
b
4 µm
c
800 nm
d
800 nm
e
2 µm
f
2 µm
g
4 µm
h
4 µm

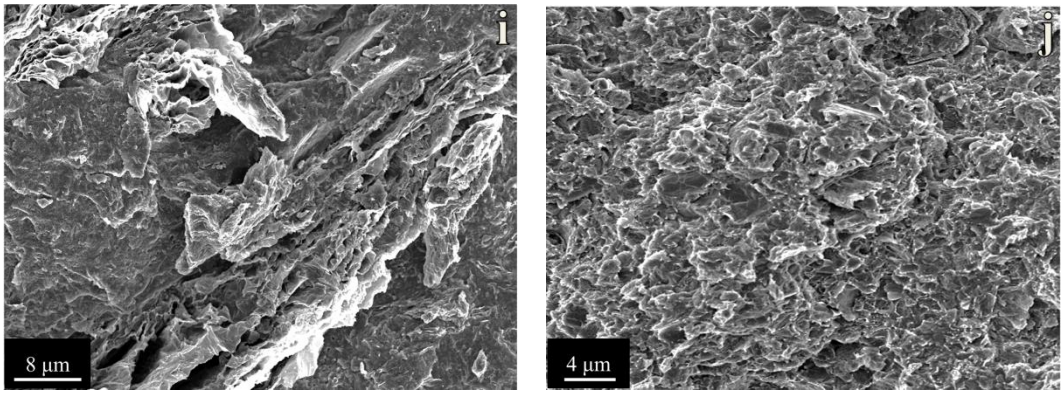

Figure 33. FESEM micrographs of (a) CBT + GNP and (b) pCBT + GNP, (c) CBT + RGO and (d) pCBT + RGO, (e) CBT + RGO_1700 and (f) pCBT + RGO_1700, (g) CBT + RGO-2 and (h) pCBT + RGO-2, (i) CBT + RGO-2_1700 and (j) pCBT + RGO-2_1700

Rheology

Despite electron microscopy is widely used to obtain direct view of composite morphology, it has to be noted that it is clearly a local technique and prone to material homogeneity, nanoparticle orientation and sample preparation method, thus requiring the use of at least another complementary technique to properly assess dispersion and distribution of particles in polymer nanocomposites [184, 185]. For this reason, the study of nanoparticle dispersion and organization in the oligomer and polymer matrices was completed carrying out dynamic frequency sweep tests in the molten state, as the elastic modulus (G') and complex viscosity (η*) of a nanocomposite are strongly affected by nanoflake dispersion and content [179].

η* and G' as a function of deformation frequency plots for pCBT and CBT containing 5 wt.% of GRM are presented in Figure 34: rheological data (G' and η*) related to pCBT and its nanocomposites were previously reported in chapter 4 and recalled here for comparison with CBT-based nanocomposites. CBT/rGO nanocomposites exhibit a marked dependence of the complex viscosity with frequency [179], with viscosity values several decades higher than those of pure CBT (0.02 Pa s at 190°C [183, 186]), thus indicating a very strong effect of nanoparticles on the rheology of the oligomers. Furthermore, the weak dependence of G' on the frequency in the whole frequency range used in this work evidences for the formation of a solid-like network of nanoparticles within the molten CBT. It is worth observing that, for a selected type of rGO (RGO or RGO-2), weak differences in η* and G' values (at 190°C) are observed in the

whole frequency range when comparing high temperature treated *vs.* untreated particles. In fact, viscosity and G' values (Table 10) of ~ $1 \cdot 10^5$ Pa s and ~ $1 \cdot 10^5$ Pa (at 1 rad s^{-1}) were measured for CBT + RGO and CBT + RGO_1700, respectively, while η* and storage modulus values of ~ $7 \cdot 10^4$ Pa s and ~ $7 \cdot 10^4$ Pa (at ω = 1 rad s^{-1}) were evaluated for CBT + RGO-2 and CBT + RGO-2_1700, respectively, thus suggesting no effect of nanoflake defectiveness on the rheological properties of their nanocomposites with CBT. On the other hand, the lower viscosity values measured for CBT/RGO-2 with respect to CBT/RGO nanocomposites could suggest a slightly lower dispersion degree when RGO-2 was used. For CBT/GNP nanocomposites, G' and η* values (~ 10^1 Pa and ~ 10^1 Pa s, respectively) as a function of deformation frequency are about 3 to 4 orders of magnitude lower than those measured for CBT + rGO. Despite a significant scattering of data points was observed for both G' and η*, owing to the low absolute instrumental readings for a low viscosity material tested in this conditions, complex viscosity is still dependent on the deformation frequency whereas elastic modulus plots appear to be constant within the significant data scattering, thus suggesting a weak percolation network, accordingly with the poor dispersion of nanoflakes observed by electron microscopy.

Linear viscoelasticity in the molten state for pCBT/GRM nanocomposites was studied at 250 °C due to the higher melting temperature of pCBT (~ 226 °C) with respect to that of CBT (the highest melting peak is located at ~ 186 °C). For all the pCBT/GRM nanocomposites, η* strongly depends on the deformation frequency, while the dependence of G' is weak, especially at low deformation frequencies, thus indicating the formation of a solid-like network for all the nanocomposites [99]. At low frequencies, the viscosity of pCBT + GNP exhibits a linear dependence with the frequency, with a η* value of ~ 10^3 Pa s (at 1 rad s^{-1}) which is one order of magnitude higher than that of pure pCBT. pCBT + RGO exhibits viscosity and G' values of ~ $6 \cdot 10^3$ Pa s and ~ $6 \cdot 10^3$ Pa (at 1 rad s^{-1}), respectively, while the use of annealed RGO leads to η* ~ $6 \cdot 10^4$ Pa s and G' ~ $6 \cdot 10^4$ Pa (at 1 rad s^{-1}), *i.e.* a factor of 10 increase for annealed nanoflakes. A much weaker increase of modulus and viscosity, in the range of 20%, was observed when comparing pCBT containing RGO-2 and RGO-2_1700. The increase of both G' and η* upon nanoflake annealing may be explained by an higher affinity of the polymer towards lower oxidized rGO, in agreement with data reported for PMMA/few layer graphene nanocomposites where higher impact on the viscoelastic properties were obtained with high C/O ratio nanoflakes [179]. However, such effect was not significant in CBT nanocomposites, in which

negligible differences between G' and η* of nanocomposites containing pristine or annealed nanoparticles were observed.

To better estimate the dispersion degree of the different nanoflakes, fitting of viscosity data, for both CBT and pCBT nanocomposites, was carried out at the lower shear rates (ω = 0.1 ÷ 1 rad s^{-1}) with the aim of calculating the shear thinning exponent factor, n, of the equation

$$\eta = A \cdot \omega^n \quad (9)$$

where η is the viscosity, A is a sample specific pre-exponential factor and ω is the oscillation frequency of the rheometer; the value of n is supposed to be a semi-quantitative measure of the dispersion degree of the sample, as reported by Wagener and Reisinger [187]. Fitting results are plotted as straight lines in Figure 34a, and n values calculated for all the nanocomposites are reported in Table 10. Neat pCBT exhibits perfect Newtonian behavior at the employed shear rates, with a shear thinning exponent n = -0.05, in agreement with n calculated by Wagener and Reisinger for pure PBT [187]. The addition of GNP results in n = -0.74 and n = -0.68 for CBT and pCBT nanocomposites, respectively. When rGO are included in CBT and pCBT, higher n were calculated with values ranging between n = -0.87 for pCBT + RGO and n = -0.97 for CBT + RGO-2: this clearly indicates a higher dispersion degree of all rGO respect to GNP, in agreement with the above-discussed results.

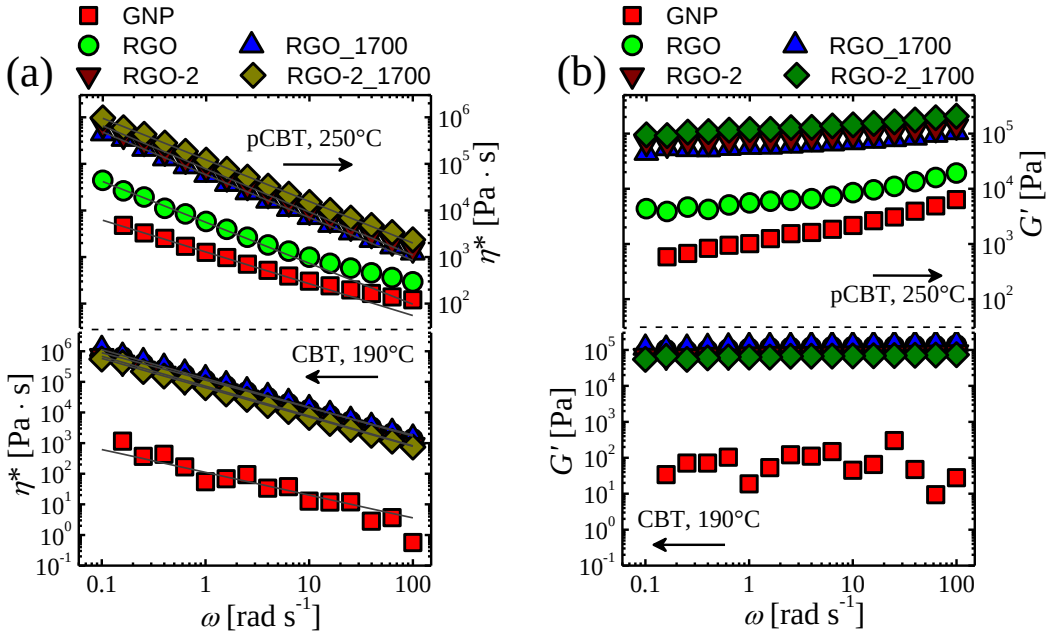

Figure 34. Dynamic frequency sweep test at 190°C and 250°C for CBT and pCBT nanocomposites, respectively. (a) Complex viscosity and (b) G' as a function of the angular frequency. The straight lines in the panel (a) represents the fitting of the different curves to calculate the shear thinning exponent factor, n, as suggested by Wagener and Reisinger [187]

Table 10. η* and G' values, for CBT and pCBT nanocomposites, measured at 1 rad s^{-1}. n represent the shear thinning exponent factor calculated by fitting of viscosity curves to the Wagener and Reisinger theory [187]

	η* [Pa · s] @ ω = 1 rad s^{-1} G' [Pa] @ ω = 1 rad s^{-1} n	
Nanoflake	CBT	pCBT
GNP	η* = 5.4 E1 G' = 1.9 E1 n = -0.74	η* = 1.25 E3 G' = 1.00 E3 n = -0.68
RGO	η* = 1.13 E5 G' = 1.11 E5 n = -0.90	η* = 5.80 E3 G' = 5.50 E3 n = -0.87
RGO_1700	η* = 1.30 E5 G' = 1.28 E5 n = -0.94	η* = 5.79 E4 G' = 5.74 E4 n = -0.91
RGO-2	η* = 7.58 E4 G' = 7.53 E4 n = -0.97	η* = 7.94 E4 G' = 7.89 E4 n = -0.92
RGO-2_1700	η* = 6.42 E4 G' = 6.31 E4 n = -0.95	η* = 1.20 E5 G' = 1.19 E5 n = -0.89

Particle size analysis

Particle size analysis of nanoflakes extracted form nanocomposites was performed analyzing RGO_1700 flakes, deposited on Si wafer, by means of scanning electron microscope. Granulated CBT + RGO_1700 and pCBT + RGO_1700 were dissolved in tetrahydrofuran (THF) and chloroform/hexafluoroisopropanol ($CHCl_3$/HFIP) mixture (90/10 v/v), respectively, for 2 hours under stirring; then, the suspension was vacuum filtered (0.45 μm pore size) to separate solubilized polymer from nanoflakes. Finally, after

drying the filter for two hours in oven at 80°C, nanoflakes were separated from the filter and collected in a glass vial.

Later ~ 0.1 mg of RGO_1700, for nanoflakes obtained from both CBT and pCBT nanocomposites, were dissolved in ~ 10 ml $CHCl_3$/HFIP mixture and sonicated in bath for 30 minutes to suspend nanoflakes; then, the suspensions were drop-casted on a silicon wafer and the solvent evaporated under a chemical hood. Deposited nanoflakes were observed without any further preparation. Particle size analysis was performed by means of image analysis software evaluating the projected area on more than 50 nanoflakes and nanoflake aggregates. Results for RGO_1700 obtained from CBT and pCBT are reported in Figure 35.

Distribution of projected area of RGO_1700 nanoflakes, extracted from CBT nanocomposites, display an approx. lorentzian curve with a maximum at 54 μm and 50% of nanoparticles showing an area below 16 μm^2, while for those extracted from pCBT nanocomposites a different distribution of projected area was observed, with a dramatic increase of the fraction of nanoflakes with small area, leading to 50% of nanoparticles showing an area smaller than 4 μm^2. It is worth noting that in both cases, the projected area is typically related to rGO aggregates, even if the smaller area observed. Smaller and thinner individual nanoflakes are difficult to be detected in these conditions and may be underestimated in this analysis. Nonetheless, significant differences are visible between size distribution in CBT and pCBT, suggesting higher disaggregation of nanoflake aggregates in pCBT, owing to its higher viscosity. A shearing effect on nanoparticle lateral size, with a reduction of lateral size upon melt mixing was also reported by Gao *et al.* [93] for PLA/GNP nanocomposites.

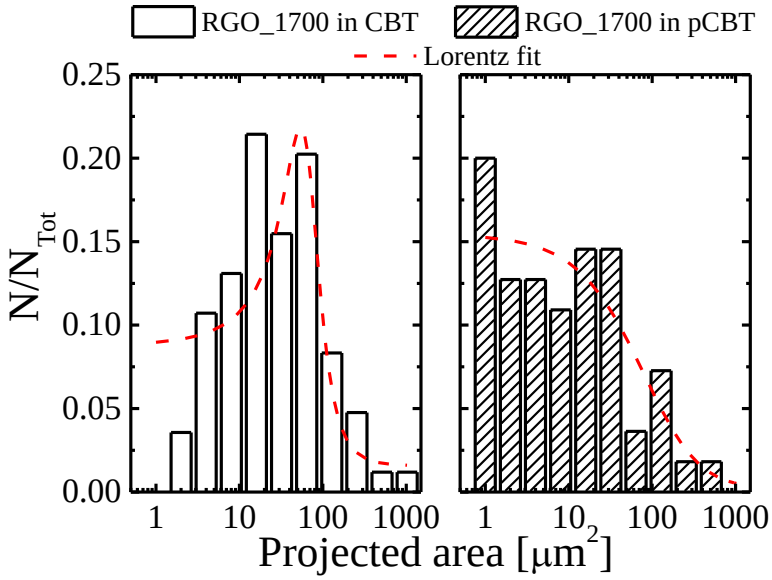

Figure 35. RGO_1700 projected area distribution before and after ring-opening polymerization of CBT into pCBT

5.1.2 Electrical conductivity

Electron microscopy and linear viscoelasticity in the molten state showed the presence of a percolation network for all the nanocomposites; this, coupled with the intrinsic conductivity of graphene related materials is expected to result in electrically conductive composites. Indeed, while polymers are well known insulating materials with an extremely low electrical conductivity ($\sigma \sim 10^{-13}$ S m^{-1} for pure pCBT [105]) a sharp increase in the electrical conductivity has been typically observed upon dispersion of conductive nanoparticles at loading above the percolation threshold, which value depends primarily on particle aspect ratio and dispersion degree [105, 181].

Electrical conductivity results on CBT and pCBT nanocomposites, containing 5 wt.% of different graphene-related materials, are reported in Figure 36 and Table 11. Despite in literature no conductivity values were previously reported for CBT, an electrical conductivity of ~ 10^{-13} S m^{-1}, *i.e.* equal to pCBT, can be taken as a realistic figure for CBT. Conductivity results for all the prepared composites evidence for nanoflake percolation: pCBT nanocomposites range from 10^{-5} S m^{-}1 for pCBT + GNP up to $1.3 \cdot 10^{-2}$ S m^{-1} for pCBT + RGO-2_1700. It is worth noting

that electrical conductivity results are consistent with the rheological data above reported: indeed, rGO (~ $1.5 \cdot 10^{-4}$ and ~ $1.0 \cdot 10^{-3}$ S m^{-1} when RGO and RGO-2, respectively, are used) are more efficient than GNP, pCBT + RGO-2 exhibits an higher electrical conductivity respect to pCBT + RGO, while the electrical conductivities of pCBT + RGO_1700 (~ $9.0 \cdot 10^{-4}$ S m^{-1}) and pCBT + RGO-2 display similar values; however, the use of annealed rGO, compared to their pristine counterparts, leads to electrical conductivity values of about one order of magnitude higher, reflecting both the higher dispersion degree and the lower defectiveness of thermally treated nanoflakes. Comparing nanocomposites based on CBT and pCBT, similar trends on the electrical conductivity values were clearly obtained for the different GRM. CBT + GNP is the nanocomposite with the lowest electrical conductivity (~ $4.9 \cdot 10^{-3}$ S m^{-1}), whereas the use of annealed rGO leads to higher values respect to their pristine counterparts (~ $1.7 \cdot 10^{-2}$ and ~ $4.7 \cdot 10^{-2}$ S m^{-1} when RGO and RGO_1700, respectively, were added to CBT, while for RGO-2 values of ~ $5.4 \cdot 10^{-3}$ and ~ $1.5 \cdot 10^{-1}$ S m^{-1} were measured for CBT + RGO-2 and CBT + RGO-2_1700, respectively). However, from the direct comparison of conductivities of CBT/GRM *vs.* pCBT/GRM, unpolymerized nanocomposites are systematically more electrically conductive than their pCBT/GRM counterparts, due to a reduction of nanoflake aspect ratio [93, 188] upon longer melt blending time and viscosity increase occurring during polymerization, as demonstrated by the electron image analysis on RGO_1700 nanoflakes extracted from their relevant CBT and pCBT nanocomposites (Figure 35).

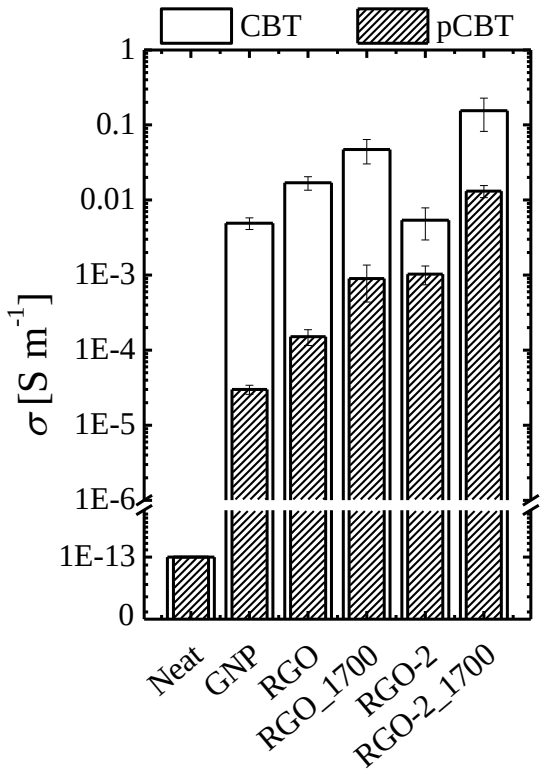

Figure 36. Electrical conductivity vs. nanoparticle and matrix type. The filler content is set constant at 5 wt.%. The value here reported for pure pCBT was taken from ref. [105] while value for pure CBT was supposed to be equal to that of pure pCBT.

Table 11. Electrical conductivity data for CBT and pCBT nanocomposites

	Electrical conductivity [S m^{-1}]	
Nanoflake	CBT	pCBT
	σ ~ 1.0 E-13	σ ~ 1.0 E-13
GNP	σ = (4.9 ± 0.1) E-3	σ = (3.0 ± 0.4) E-5
RGO	σ = (1.7 ± 0.3) E-2	σ = (1.5 ± 0.4) E-4
RGO_1700	σ = (4.7 ± 1.7) E-2	σ = (9.0 ± 4.6) E-4

RGO-2	σ = (5.4 ± 2.5) E-3	σ = (1.0 ± 0.3) E-3
RGO-2_1700	σ = (1.5 ± 0.7) E-1	σ = (1.3 ± 0.2) E-2

5.1.3 Thermal conductivity

Polymers are well known thermally insulating materials, with typical thermal conductivity values in the range 0.1 ÷ 0.4 W m^{-1} K^{-1} [1] and the addition of thermally conductive nanoparticles is known to have a positive effect for the improvement of this property. Thermal conductivity (λ) results for CBT and pCBT nanocomposites containing 5 wt.% of different graphene related materials are reported in Table 12 while the relative increase in conductivity ($\lambda_{nanocomposite}/\lambda_{matrix}$) are shown in Figure 37. Pure CBT and pCBT have thermal conductivities of ~ 0.22 and ~ 0.24 W m^{-1} K^{-1}, respectively, which is consistent with typical values measured for semi-crystalline polymers [1]. The addition of 5 wt.% of GNP, RGO and RGO-2 has a limited effect on thermal conductivity of either CBT and pCBT with values in the range of ~ 0.4 ÷ 0.5 W m^{-1} K^{-1}, *i.e.* about twice those of pure oligomer/polymer. On the other hand, the use of annealed nanoparticles dramatically increases the thermal conductivity of nanocomposites up to ~ 1.48 ± 0.02 W m^{-1} K^{-1} for CBT + RGO_1700, which is about 7 times the value measured for pure CBT. This high thermal conductivity for nanocomposites containing annealed rGO was correlated to the lower defectiveness of annealed rGO, combined with their high aspect ratio, in the previous chapter of this thesis. The novel aspect from this thesis is that thermal conductivity values obtained for CBT/rGO_1700 nanocomposites are ~ 20 ÷ 65 % higher than for the correspondent formulations based on pCBT. This is likely related to the higher aspect ratio of nanoflakes in CBT nanocomposites, as the effect of aspect ratio reduction was previously recognized to be detrimental in polymer nanocomposites [93, 189]. In fact, the progressively increasing applied shear during melt mixing, owed to the viscosity increase during ring-opening polymerization of CBT into pCBT, is responsible for the reduction of nanoflake aggregate size, as demonstrated in the case of RGO_1700 nanoflakes extracted from their relevant CBT and pCBT nanocomposites (Figure 35).

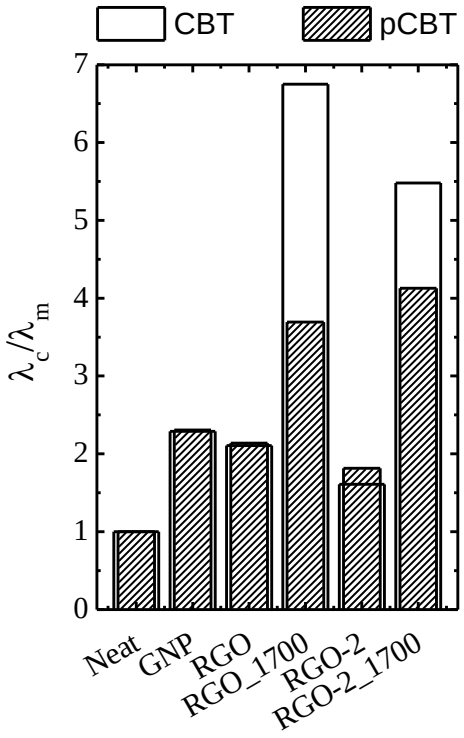

Figure 37. Normalized thermal conductivity vs. nanoparticle and matrix type. The filler content is constant at 5 wt.%.

Table 12. Thermal conductivity data for CBT and pCBT nanocomposites

Thermal Conductivity [W m^{-1} K^{-1}]		
Nanoparticle	CBT	pCBT
	$\lambda = 0.219 \pm 0.005$	$\lambda = 0.241 \pm 0.001$
GNP	$\lambda = 0.501 \pm 0.002$	$\lambda = 0.556 \pm 0.001$
RGO	$\lambda = 0.461 \pm 0.001$	$\lambda = 0.515 \pm 0.004$
RGO_1700	$\lambda = 1.478 \pm 0.020$	$\lambda = 0.890 \pm 0.009$
RGO-2	$\lambda = 0.352 \pm 0.001$	$\lambda = 0.437 \pm 0.003$
RGO-2_1700	$\lambda = 1.200 \pm 0.007$	$\lambda = 0.995 \pm 0.001$

The use of high aspect ratio and low defective rGO turned out to be the best combination for the preparation of highly thermally and electrically conductive polymer nanocomposites, both in CBT and pCBT. Finally, it is worth mentioning that the low molecular weight of CBT oligomers (and the associated low mechanical properties) prevents the use of unpolymerized CBT nanocomposites in most practical applications. However, CBT nanocomposites may find applications as intermediates in polymer processing, *e.g.* as masterbatches in the preparation of nanocomposites with low nanoparticle content.

5.2 Conclusions

The present chapter is focused on morphology and conductivity properties evolution upon ring-opening polymerization during extrusion for the production of poly butylene terephthalate nanocomposites containing graphene-related materials, including GNP, rGO and thermally-annealed rGO. Despite unpolymerized CBT nanocomposites cannot be regarded as materials for real application, owed to their low mechanical properties and low melting temperature range, this work was aimed at elucidating how nanocomposite properties change upon the ring-opening polymerization. This can help to develop and optimize reactive extrusion processing of pCBT nanocomposites in order to improve the desired properties.

The extremely low viscosity of CBT during compounding did not allow to apply sufficiently high shear forces during melt mixing, resulting in poor dispersion and distribution degree of nanoparticles. However, the low viscosity allowed the infiltration of oligomers into the accordion-like structure of rGO aggregates. Viscosity increase during polymerization of CBT into pCBT, resulting in a rise of the applied shear during melt mixing, led to a higher dispersion and distribution degree of rGO nanoflakes, as well as their lateral size reduction. Linear viscoelasticity in the molten state showed the presence of a percolation network for all the nanocomposites. However, clear differences are observed between nanocomposites containing rGO and GNP, in terms of higher density of the percolation network obtained for rGO nanoflakes.

Electrical conductivity results for CBT and pCBT nanocomposites were consistent with the rheological data, the conductivity with rGO being typically significantly higher compared to GNP. Furthermore, the conductivity with annealed rGO being greater compared to pristine rGO for both CBT and pCBT nanocomposites (the highest values $\sigma \approx 0.2$ S m^{-1} and $\sigma \approx 0.01$ S m^{-1} for CBT and

pCBT nanocomposites, respectively, containing annealed RGO-2) evidencing the importance of the exploitation of nanoflakes with low defectiveness. Electrical conductivities of CBT based materials are systematically higher (up to two order of magnitude for GNP, RGO and RGO_1700) respect to pCBT nanocomposites. This is related to the reduction of aspect ratio of nanoflakes upon polymerization, owing to the longer processing time and the rising applied shear as a consequence of viscosity increase during polymerization of CBT into pCBT.

The thermal conductivity of nanocomposites was strongly affected by the quality of nanoflakes. The use of as obtained/s received GNP and rGO resulted in nanocomposites with limited thermal conductivity improvements (~ 2-fold increase) independently on the matrix, while the higher values (ranging between 3.5 and 7-fold increase) were obtained with annealed rGO, further confirming the importance of exploitation of high quality graphene-related materials. Comparison between CBT and pCBT nanocomposites, containing annealed rGO, showed better thermal conductivities for CBT nanocomposites (the highest values ~ 1.5 W m^{-1} K^{-1} and ~ 1.0 W m^{-1} K^{-1} for CBT and pCBT nanocomposites, respectively), which is consistent with electrical conductivities and related to the mentioned reduction in aspect ratio of nanoflakes upon polymerization.

Chapter 6

Effect of reduced graphene oxide on the nanocomposite crystallization

In the previous chapters, GNP and RGO were reported to affect the melting and crystallization behavior of pCBT, leading to the formation of crystals with homogeneous thickness distribution and shifting the crystallization temperature to higher temperatures, as observed also by Balogh *et al.* [190].

In the present chapter a deep insight on the crystallization behavior of pCBT and its nanocomposites containing 10 wt.% of RGO and RGO_1700 is addressed. The interest in study the crystallization of pCBT/RGO nanocomposite is related to the appearance of a new melting/crystallization peak at high temperatures in pCBT nanocomposites containing annealed rGO, with enhanced signal when low defective high aspect ratio nanoparticles are used. In particular, the exploitation of a large amount of annealed nanoflakes resulted in higher intensity of this peak, making this material interesting to gain insight into the nature of this new peak. Characterization of pCBT and its nanocomposites was carried out by means of advanced scanning procedures in differential scanning calorimetry (DSC) as well as by wide angle X-ray scattering (WAXS).

6.1 Crystallization

6.1.1 Standard DSC experiments

Non-isothermal DSC cooling scans, after erasing the thermal history, and following heating scans are showed in Figure 38, whereas the significant thermal parameter collected from these measurements are listed in Table 13and Table 14.

After extrusion in presence of the tin catalyst, none of the three materials exhibits traces of crystallization and melting typical for CBT oligomers, reported in chapter 5, thus suggesting a high conversion of CBT into pCBT. In the presence of nanoflakes, the crystallization peak temperature shifts from ~ 190°C for pure pCBT up to ~ 201 °C and ~ 208 °C for pCBT + 10% RGO and pCBT + 10% RGO_1700, respectively, evidencing for a strong nucleating effect of nanoflakes, which is typical for GRM in pCBT [51, 147, 190]. This nucleating effect is reflected on the melting behavior of pCBT: neat pCBT exhibits two partially overlapping endothermic peaks, the first, at lower temperature (~ 217 °C), related to melting and re-crystallization of thinner crystals, which subsequently re-melt at higher temperatures (~ 223 °C), *i.e.* in the second peak [178]. On the other hand, in nanocomposites only the high temperature melting peak is observed; this is related to the formation of thicker crystals during cooling scans in presence of rGO nanoflakes, in agreement with Balogh *et al.*[190] Comparing the effect of the different rGO, both crystallization and melting peaks are located at higher temperature, and appears to be narrower when RGO_1700 was used, thus indicating an efficient nucleation leading to thicker crystals in the presence of annealed rGO. The narrower and higher intensity peak observed for pCBT + 10% RGO_1700, compared with pCBT + 10% RGO, indicates that the structure of the nanoflakes (in terms of low defectiveness and high aromaticity of graphitic planes) plays a key role. Furthermore, it is worth observing that in pCBT + 10% RGO_1700 a new peak appears, which is not present in pure pCBT, located at ~ 233 °C and ~ 250 °C during cooling and heating scans, respectively, with a calculated enthalpy of about 4 J g^{-1}. When carefully analyzing the DSC plots for pCBT + 10% RGO, similar peaks can also be detected. However, in presence of RGO, the peaks were located at slightly lower temperatures (~ 227 °C for crystallization and 247 °C for melting) and with a calculated enthalpy of about 1 J g^{-1}, further supporting the differences in pCBT crystallization in the presence of pristine *vs.* annealed rGO. To the best of the author's knowledge, such high temperature crystallization and melting peaks were not reported in pCBT

literature during non-isothermal DSC scans. This peak could be related to the formation of a thick stack of chain crystals, knowing that for pCBT the equilibrium melting temperature, *i.e.* an infinite stack of extended chain crystals, was reported to be 255.8 °C by Samsudin *et al.* [191] and 257.8 °C by Wu *et al.* [192].

The degree of crystallinity, calculated on both low and high temperature peaks for nanocomposites, is slightly affected by the presence of rGO, with a slight increase from 37% for neat pCBT up to 41% and 45% for pCBT + 10% RGO and pCBT + 10% RGO_1700, respectively.

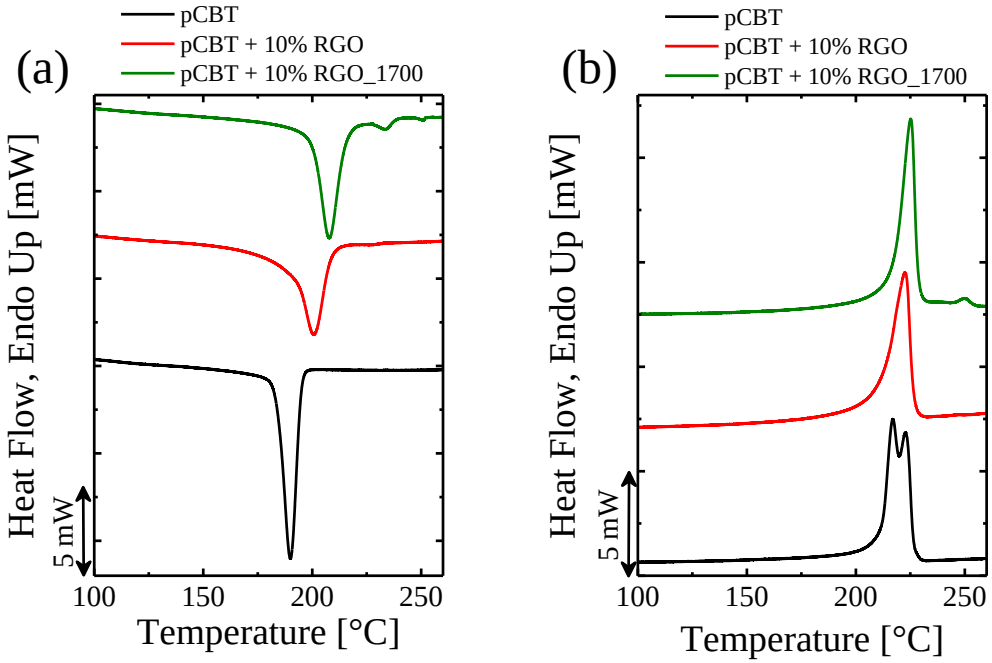

Figure 38. Standard DSC (a) cooling and (b) heating scans

Table 13. Standard DSC results for cooling scans on pCBT and its nanocomposites

Material	Cooling scans				
	T_c [°C]		ΔH_c [J g^{-1}]		X_c [%]
	T_c^1	T_c^2	ΔH_c^1	ΔH_c^2	
pCBT	189.9	-	52	-	37
pCBT + 10%RGO	200.7	227.0	56	1	41
pCBT + 10%RGO_1700	207.7	233.3	59	4	45

Table 14. Standard DSC results for cooling scans on pCBT and its nanocomposites

Material	Heating scans					
	T_m [°C]			ΔH_m [J g^{-1}]		X_c [%]
	Tm^1	T_m^2	Tm^3	ΔH_m^1	ΔH_m^2	
pCBT	216.9	222.6	-	52	-	37
pCBT+10%RGO	-	222.5	246.6	56	1	41
pCBT+10%RGO_1700	-	225.1	249.7	59	4	45

To investigate the formation of the high stability crystals, increase of the amount of this crystalline population was attempted via solution mixing, which allowed preparing a pCBT composite containing 50 wt.% of RGO_1700, which is clearly not feasible via melt compounding.

DSC heating and cooling scans for pCBT + 50% RGO_1700 after solvent evaporation are reported in Figure 39. In the first heating, the main melting peak of pCBT was characterized by a shoulder in the low temperature side indicating imperfect wide distribution of crystal size and/or defectiveness, obtained during

solvent evaporation. Furthermore, no clear signs of the highly stable crystals were observed. However, in cooling scans, and in the subsequent heating scans, the high temperature crystalline population becomes clearly visible, at slightly lower temperatures (crystallization at ~ 224 °C and melting at ~ 241 °C) compared to the melt-processed nanocomposite (containing a lower amount of nanoflakes). The crystallinity was ~ 60 %, whereas the enthalpy related to the highly stable crystal fraction was about 12 % of the main peak value, thus confirming an increase compared to pCBT + 10% RGO_1700, in which the high stability fraction corresponds to about 7 %. Clearly, the increase of this new crystalline population is non-linear with increasing the nanoflakes content, which may be due to different possible explanations. On the one hand, it is likely that the limit for the crystallization into a highly stable fraction is related to the dispersion of the nanoparticles, thus affecting the extent of interfacial surface area. With a nanoparticle loading of 50 wt.%, aggregation of nanoflakes certainly occurs. This leads to an effective interfacial area, with the polymer, which is expected to be far below the maximum theoretical value, limiting the influence of the nanoparticles on the crystallization of pCBT in proximity of the same nanoflakes. On the other hand, there may also be an effect of shearing: a relatively high shear rate is applied during extrusion and polymerization of CBT into pCBT, which may lead to an intimate contact between the polymer and the nanoflakes, as a consequence of chains orientation, while no significant shear is applied during solution mixing.

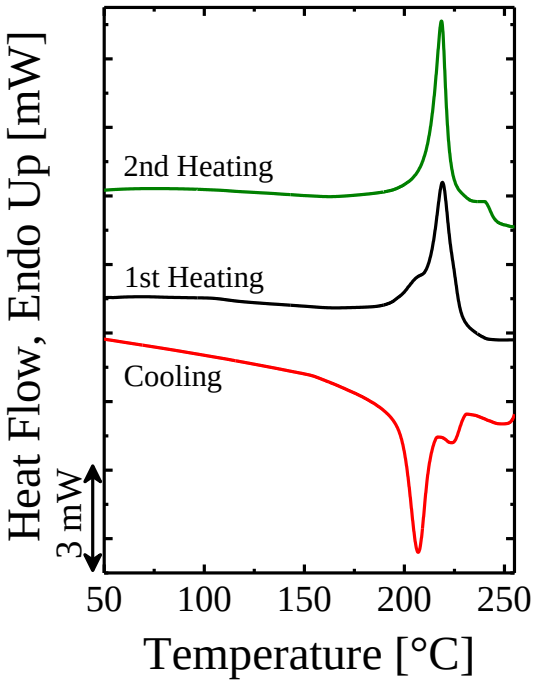

Figure 39. Standard DSC cooling, 1st and 2nd heating scans for pCBT + 50% RGO_1700 obtained by solvent mixing

As clear nucleation effects were suggested from the simple DSC cycles commented above, further studies were undertaken to elucidate the mechanisms of nucleation and growth induced by the different rGO nanoflakes on pCBT, including isothermal crystallization and self-nucleation studies.

Thermal stability

Non-isothermal DSC cooling scans were employed to study how the temperature selected to erase the thermal history of the sample (T_{max}), affects T_c. For this reason, samples were heated from 25 °C up to T_{max} (at 20 °C min^{-1}), held at T_{max} for 3 minutes, then cooled down to 25 °C (at 20 °C min^{-1}) and held at this temperature for 1 minute. This procedure was repeated for 26 times. Tests were carried out only on pure pCBT and new samples were used for each test. Experimental results for T_c *vs.* N, obtained after tests at the different T_{max}, are summarized in Figure 40.

T_c *vs.* N plots, reported in Figure 40, show that the crystallization peak temperature generally increases as the number of cycle increase, independently on T_{max}, thus indicating a degradation of the polymer matrix, with a reduction of the average pCBT chain lengths. Indeed, for entangled systems a decrease in the molecular weight can result in an initial increase in the crystallization temperature, owed to a higher mobility of polymer chains. It is noteworthy that the evolution of T_c against cycles is strictly connected to the set T_{max}. For T_{max} = 250 °C and T_{max} = 260 °C, the measured T_c started at about 189 ± 0.5 °C and monotonically increase with cycles, with a higher slope at the higher temperature. When heating at T_{max} = 280 °C, crystallization temperature on first cycle was measured at about 191 °C and rapidly increased with N, indicating a fast and extensive thermal degradation upon cycling. The limited thermal degradation observed when T_{max} = 250 °C made the use of this temperature interesting as upper limit for SN and SSA experiments. However, the presence of the high temperature melting phase (~ 250 °C) in pCBT nanocomposites would result in the presence of crystal fragments which could act as nucleating agent, affecting the experiments. For this reason, for SN and SSA tests was selected T_{max} = 260 °C as a good compromise between thermal degradation and erasure of the thermal history.

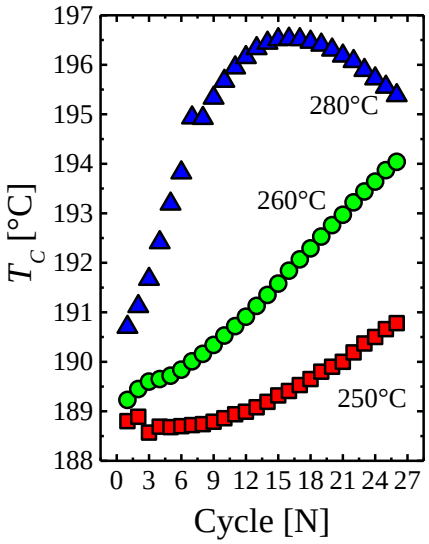

Figure 40. T_c measured in standard cooling scans after heating up to T_{max} (selected to erase the thermal history and reported in the graph) for N times

6.1.2 Isothermal crystallization experiments

Isothermal crystallization tests allow evaluating the overall crystallization rate of the polymer (including both nucleation and growth). Both pCBT nanocomposites exhibited crystallization temperature ranges at higher values respect to neat pCBT, thus indicating that lower supercooling are required, in agreement with results obtained by standard DSC experiments. However, the large difference in crystallization temperature range between composites containing RGO_1700 and RGO has to be highlighted. In fact, crystallization kinetics were found to be so different to make superposition of crystallization temperature ranges impossible. The increase of the crystallization rate for nanocomposites could be related to both the nucleating effect of rGO and the increase in growth rate expected upon a reduction of molecular weight (M_w), which has been observed for nanocomposites prepared via ring-opening polymerization in presence of nanoflakes in similar pCBT nanocomposites [193]. Indeed it is well known that M_w affects the crystallization rate of polymers, although the correlation is quite complex [194, 195], and, to the best of author's knowledge, no studies on the isothermal crystallization of pCBT with different M_w are reported in literature. It is worth observing that for pCBT + 10% RGO_1700 only a limited amount of points allowed a reliable calculation of crystallization rate. In fact, at temperatures higher than 219°C no crystallization peaks were observed, whereas below 218°C incomplete curves were recorded, indicating that crystallization started during cooling from the melt to the isothermal crystallization temperature, leading to large errors in fitting [159].

The data collected, at the different isothermal crystallization temperatures for the different materials, allowed for the calculation of crystallization rate of the polymer (including both nucleation and growth) in terms of half-crystallization time, determined as a function of isothermal crystallization temperature, after fitting experimental results with Avrami model. Crystallization rates are reported in Figure 41a as the inverse of the experimentally measured half-crystallization time *vs.* crystallization temperature (refer to Table 15 for parameters obtained by fitting to the Avrami theory), showing that nanocomposites reached a defined crystallization rate at temperatures significantly higher than for the pristine pCBT. Furthermore, the average Avrami index *n* (Figure 41b and Table 15) calculated for pure pCBT crystallization is about 2, which indicates the nucleation of instantaneous axialites [196]. In nanocomposites were calculated *n* values between 1.5 and 1.8, suggesting that rGO does not alter the overall phenomenology of pCBT crystallization.

Experimental data reported in Figure 41a were fit with Lauritzen and Hoffman theory [197, 198], evidencing very good agreement between experimental and theoretical results for both pristine pCBT and pCBT nanocomposites (Fitting parameters are listed in Table 16), despite the limited available amount for pCBT + 10% RGO_1700. However, Lauritzen and Hoffman fitting reveals that the presence of rGO leads to a reduction in the energy barrier required for nucleation and growth (K_g values), a decrease on fold surface free energy (σ_e) and on the work required to fold chains (q), the greater effect when annealed RGO were used. This is a further proof of the strong effect of these carbon nanoflakes on the crystallization, including both nucleation and growth, of pCBT.

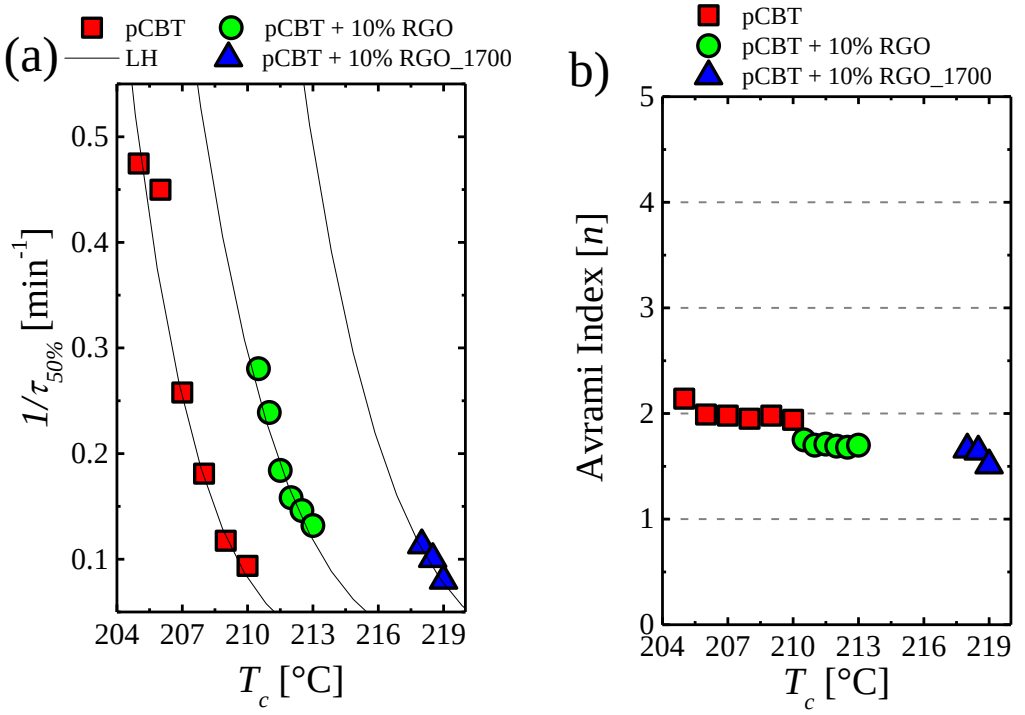

Figure 41. (a) Overall crystallization rate ($1/\tau_{50\%}$) as a function of isothermal crystallization temperature and (b) Avrami index values for pCBT and pCBT/rGO nanocomposites.

Table 15. Parameters obtained by fitting with Avrami theory the data obtained from isothermal crystallization tests

sample	T_c [°C]	n	K x 10^3 [min^{-n}]	$\tau_{1/2t}$ [min]	$\tau_{1/2e}$ [min]	R^2
pCBT	205	2.1	269.0	1.56	2.11	0.9995
	206	2.0	174.0	2.01	2.22	0.9995
	207	2.0	60.7	3.43	3.88	0.9998
	208	2.0	28.2	5.17	5.53	1
	209	2.0	11.2	8.03	8.52	0.9999
	210	1.9	7.2	10.50	10.69	0.9999
pCBT + 10% RGO	210.5	1.8	91.5	3.18	3.57	0.9998
	211	1.7	78.0	3.61	4.19	0.9997
	211.5	1.7	52.6	4.51	5.43	0.9994
	212	1.7	39.8	5.44	6.32	0.9998
	212.5	1.7	34.4	5.95	6.85	0.9993
	213	1.7	25.0	7.01	7.59	0.9999
pCBT + 10% RGO_1700	218	1.7	23.5	7.70	8.83	0.9994
	218.5	1.6	18.4	9.18	9.97	0.9990
	219	1.5	17.2	11.52	12.54	0.9993

Table 16. Parameters obtained from fitting the Lauritzen and Hoffman to the data of Figure 41

sample	K_g^{τ} [K^2]	σ [erg cm^{-2}]	σ_e [erg cm^{-2}]	q x 10^{13} [erg]	R^2
pCBT	476000	10.60	193.2	11.2	0.9778
pCBT + 10% RGO	342000	10.60	139.0	8.1	0.9617
pCBT + 10% RGO_1700	276000	10.60	111.8	6.5	0.9753

6.1.3 Self-nucleation and nucleation efficiency

Standard and isothermal DSC experiments revealed the strong nucleation effect of rGO on the crystallization behavior of pCBT. Self-nucleation (SN) can allow to quantitatively assess the nucleation efficiency (NE) of rGO, comparing the effects of these nanoparticles on pCBT crystallization against that of self-nuclei.

Self-nucleation of pCBT was first studied to investigate the three *Domains* related to the absence of nuclei, to the formation of self-nuclei and to the annealing of unmolten pCBT crystals, respectively. Figure 42a displays DSC cooling plots following the heating ramp to a selected T_s temperature, while in Figure 42b are reported the subsequent heating runs. For T_s temperatures equal or higher than 231 °C, T_c temperature were independent on T_s (Figure 42a), indicating that the crystalline memory of pCBT was erased and crystals were completely molten. Furthermore, no clear alterations of melting profile (Figure 42b) were observed in the same temperature range. These indicates that neat pCBT is in *Domain I*, as defined by Fillon *et al.* [160].

In the T_s temperature range 230 ÷ 227 °C, the crystallization temperature gradually shifted to higher values (Figure 42a) upon decrease of T_s. Furthermore, changes in the melting behavior of pCBT (Figure 42b) were observed after treatment at T_s 230-227 °C: indeed, the peak at lower temperature, related to melting and recrystallization of thinner crystals formed during cooling from T_{max} [178], slightly moved to higher temperatures, whereas the peak related to the main melting of pCBT remained unaltered. When T_s = 227 °C only one melting peak was observed, thus indicating that nuclei, formed at that temperature, allowed the formation of thicker pCBT crystals. The behavior observed in this T_s range is characteristic of *Domain II*, where pCBT is nucleated by its own self-seed, *i.e.* self-nucleation occurs. Indeed a T_c shift to higher values is an indication of an increase in the nucleation density of pCBT. T_s = 227 °C was therefore found as the ideal SN temperature since it maximizes the nucleation density without altering the polymer melting behavior.

Finally, for T_s equal or lower than 226°C a further shift of the crystallization peak to higher temperatures was observed (Figure 42a), whereas in melting scans a tiny peak at temperatures slightly higher than that of melting appeared (indicated by the arrow in Figure 42b). The presence of this peak is related to the melting of annealed crystal fractions surviving at T_s and annealed during the isothermal at T_s, thus evidencing the behavior typical of *Domain III*. A schematic representation of

T_c *vs.* T_s, for neat pCBT, and the location of the different *Domains* is reported in Figure 43.

The efficiency of rGO as nucleating agents for pCBT was calculated by the following equation proposed by Fillon *et al.* [199]:

$$N.E. = \frac{T_{c,NA} - T_{c,pCBT}}{T_{c,max} - T_{c,pCBT}} \times 100 \qquad (10)$$

where $T_{c,NA}$ is the peak crystallization temperature of the polymer containing the nucleating agent (200.7 °C and 207.7 °C for pCBT + 10% RGO and pCBT + 10% RGO_1700, respectively), $T_{c,pCBT}$ is the peak crystallization temperature of neat pCBT after erasure of its crystalline memory (189.9 °C) and $T_{c,max}$ is the peak crystallization temperature obtained (196.5 °C) after pCBT was nucleated at 227 °C, identified as the ideal self-nucleation temperature.

Based on the temperature values above reported, the nucleation efficiency was calculated as N.E. = 164% and 270% for RGO and RGO_1700, respectively, thus indicating that rGO are significantly more efficient in nucleating pCBT respect to its own self-nuclei. This effect was termed as super-nucleation [200] and, to the best of author's knowledge, was never reported in literature for graphene related materials. Actually, Dai *et al*. [201] reported a nucleating efficiency between 10 and 20 % for polypropylene nanocomposites containing 0.5 wt.% of GNP. Furthermore, the annealing of rGO nanoflakes demonstrated a dramatic effect on nucleation, leading to much higher nucleation efficiency when nanoflakes with low defectiveness are used.

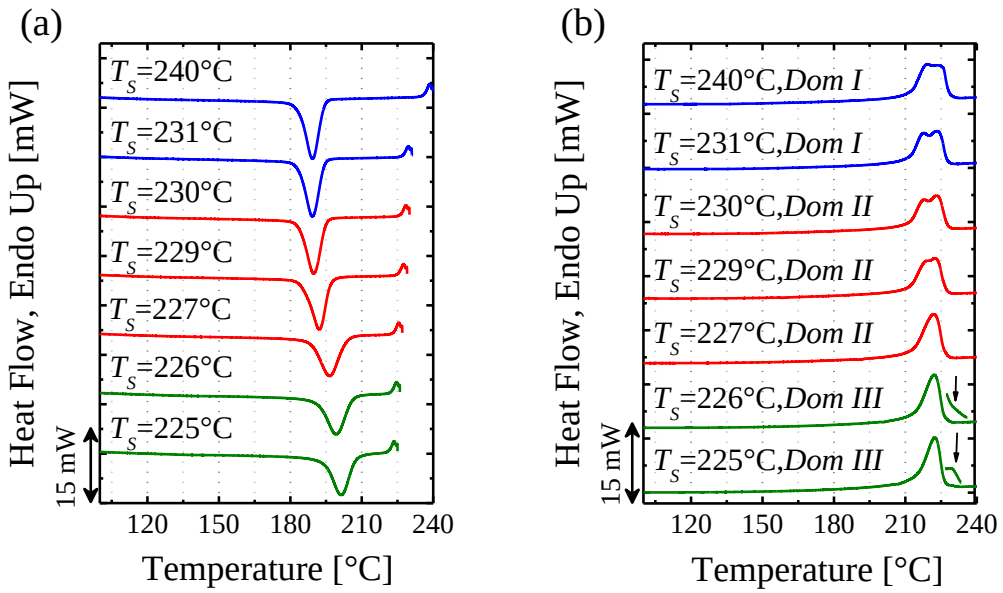

Figure 42. DSC (a) cooling scans from the indicated T_s and (b) heating scans after cooling from the indicated T_s for neat pCBT.

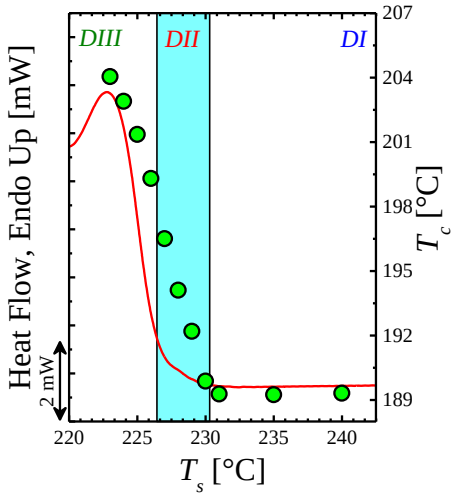

Figure 43. Standard DSC heating scans (red line) plotted along with crystallization peak temperatures (green circles) *vs.* T_s for pCBT. The vertical lines indicate the *Domain* borders. The temperature range at which materials experienced *Domain II* is highlighted.

Beside the super-nucleation effect, it is also of interest to study how these nanoparticles affect the different *Domains* in self-nucleation experiments. Results for pCBT + 10% RGO are reported in Figure 44a (DSC cooling plots for selected T_s temperatures), Figure 44b (the subsequent heating runs) and and Figure 44c (magnifications at high temperatures of heating runs), whereas results for pCBT + 10% RGO_1700 are reported in Figure 45a (cooling plots for selected T_s temperatures), Figure 45b (the subsequent heating runs) and Figure 45c (magnifications at high temperatures of heating runs).

Comparing cooling and heating curves of the two nanocomposites, both rGO exhibited similar effects. Indeed, no significant shifts of the crystallization and melting peaks temperatures were observed, changing T_s temperature, for both nanocomposites. Furthermore, also the high melting peak, centered at ~ 250 °C, does not exhibit any shift when varying T_s but, in agreement with non-isothermal DSC experiments, signal intensity for this high melting phase was increased by the presence of thermally annealed RGO. When carefully analyzing the temperature range between the two melting peaks (*i.e.* approx. 225 ÷ 260 °C), in pCBT + 10% RGO_1700, an additional broad and clear signal may be observed (Figure 45c), which was also observed, with a tiny intensity, in pCBT + 10% RGO (Figure 44c). This melting peak temperature was observed to depend on the selected T_s, thus indicating annealing of the polymer matrix, which is typical of *Domain III*. This behavior in presence of rGO could be expected, considering that the selected self-nucleation temperatures are below the melting of the high temperature phase, which can play a key role in the nucleation and annealing of pCBT.

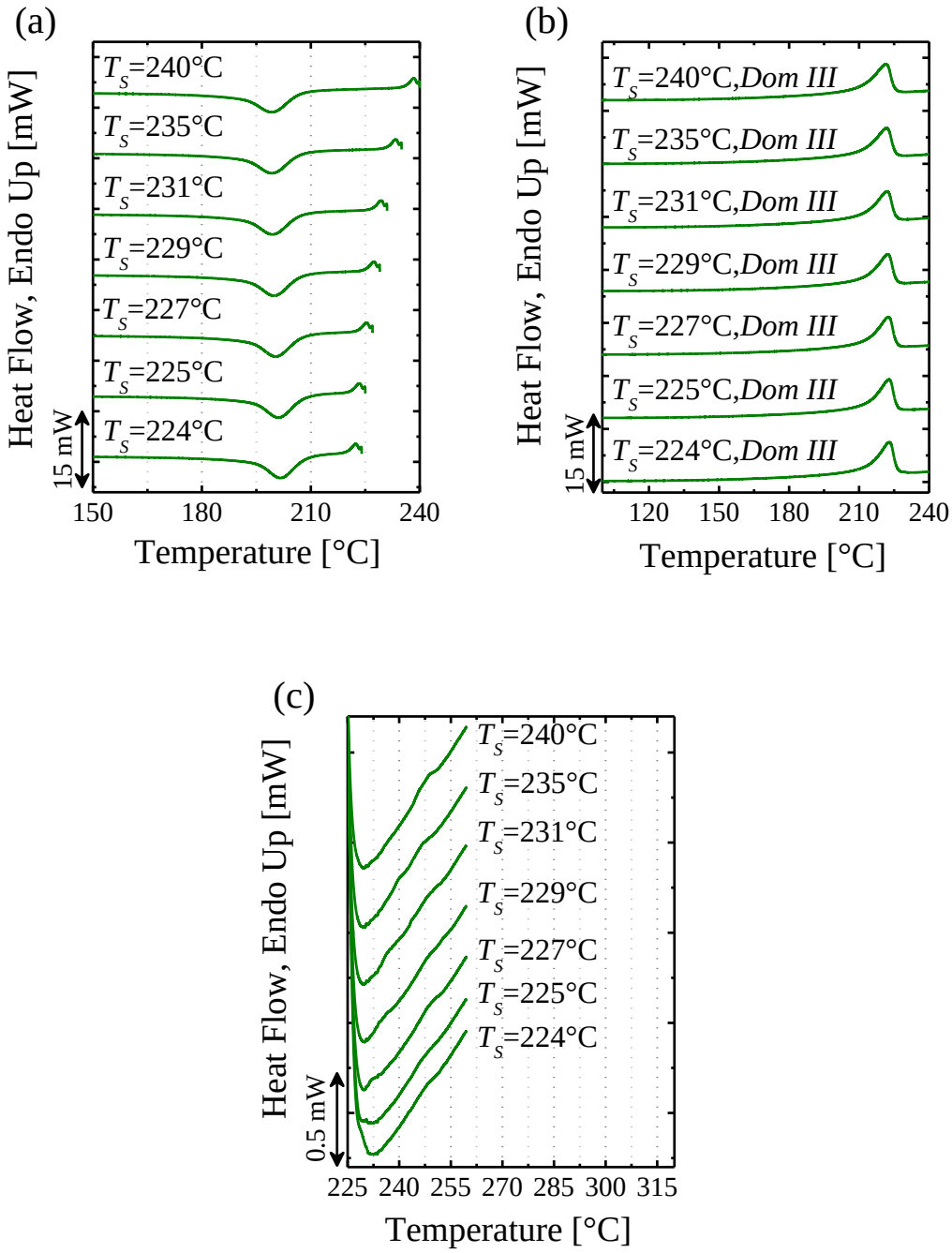

Figure 44. DSC (a) cooling scans from the indicated Ts and (b) heating scans after cooling from the indicated Ts for pCBT + 10% RGO.

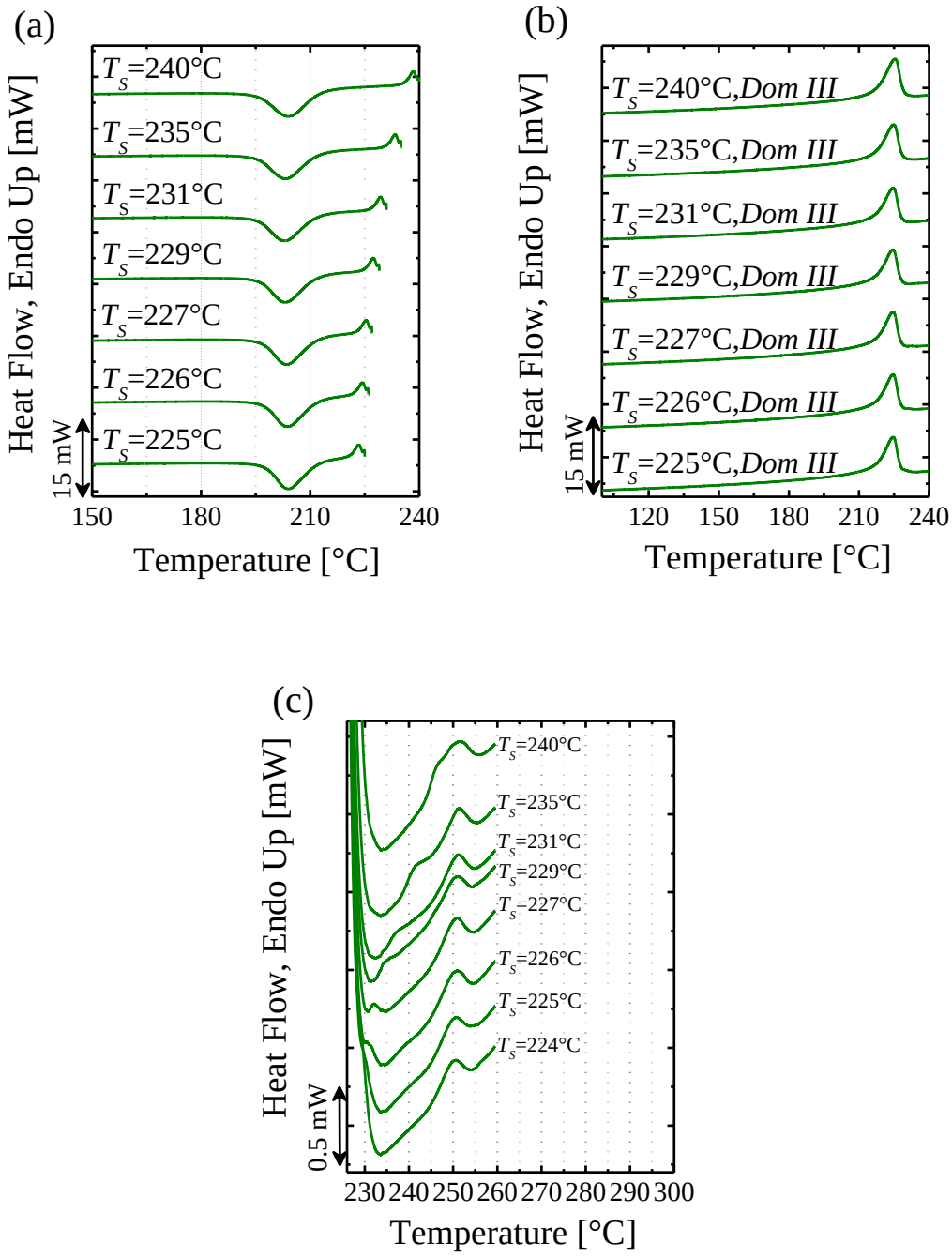

Figure 45. DSC (a) cooling scans from the indicated T_s and (b) heating scans after cooling from the indicated T_s for pCBT + 10% RGO_1700. (c) Zoom on the temperature range of the high temperature melting peak of the heating scans reported in Figure 44b.

Self-nucleation experiments on neat pCBT, above reported and discussed, showed the presence of the three *Domains* defined by Fillon [160] with the ideal self-nucleation temperature T_s = 227 °C. On the other hand, the presence of rGO drastically changed the pCBT behavior in SN tests, with annealing occurring even when the standard pCBT crystals should be molten, thus indicating that the polymer is always in *Domain III*. This behavior could be related to the presence of the highly stable crystalline population, which appears in presence of nanoflakes, especially whit annealed RGO. Furthermore, the calculation of nanoflake nucleation efficiency revealed a super-nucleating effect, which to the best of authors' knowledge was never reported in literature for pCBT/rGO nanocomposites.

6.1.4 Successive Self-Nucleation and Annealing

Successive self-nucleation and annealing may be used to obtain a fractionation due to molecular segregation based on chain length differences, [202]. Thermal fractionation experiments on pCBT were performed setting as first T_s temperature the $T_{s,ideal}$ determined in self-nucleation experiments, *i.e.* T_s = 227 °C. The thermal protocol consisted in seven T_s, from 227°C down to 197°C. Despite Müller *et al.* [161, 162] suggested 5 minutes as ideal isotherm time at T_s, in the present chapter only 1 minutes was spent at each T_s, to limit the thermal degradation of the polymer matrix during SSA experiment.

For neat pCBT, DSC heating scan after completion of SSA and the second heating measured by non-isothermal DSC experiments are reported in Figure 46. The shape of DSC curve drastically changed after thermal fractionation, with the disappearance of the lower temperature melting peak related to melting/recrystallization of thin polymer crystals [178]. Furthermore, the implementation of SSA to pCBT exhibited effective fractionation with the formation of five thermal fractions, as the isothermal at $T_{s,ideal}$ does not generate a thermal fraction but only maximizes the number of self-nuclei [162]. It is worth observing that the three thermal fractions at higher temperatures were overlapped, thus suggesting that higher time at each would result in higher annealing and in a better thermal fractionation.

The protocol for SSA thermal fractionation of nanocomposites was slightly changed respect to that of neat pCBT, owed to the presence of the high melting phase. Indeed, twelve T_s temperatures (indicated by vertical lines) were selected, starting from 252°C down to 197°C, still assuming T_s = 227 °C as $T_{s,ideal}$

(segmented blue vertical lines). Results for pCBT + 10% RGO are reported in Figure 47a and Figure 47b, whereas corresponding plots for pCBT + 10% RGO_1700 are reported in Figure 47c and Figure 47d. For both nanocomposites, thermal fractionation of the polymer matrix was observed for the main melting peak of pCBT as well as for the high-temperature melting phase. This is a further proof that the high temperature crystalline population is related to real polymer crystals, which can be annealed and fractionated. Finally, it is worth observing that after thermal fractionation, in pCBT + 10% RGO_1700 the higher melting peak temperature is centered at ~ 253 °C, which is once again close to the equilibrium melting temperature estimated in literature for neat pCBT [191, 192]. This further indicates the chain conformation as thick stack of chain crystals, especially in presence of rGO with low defectiveness and oxidation, which appear to have higher interaction with polymer chains.

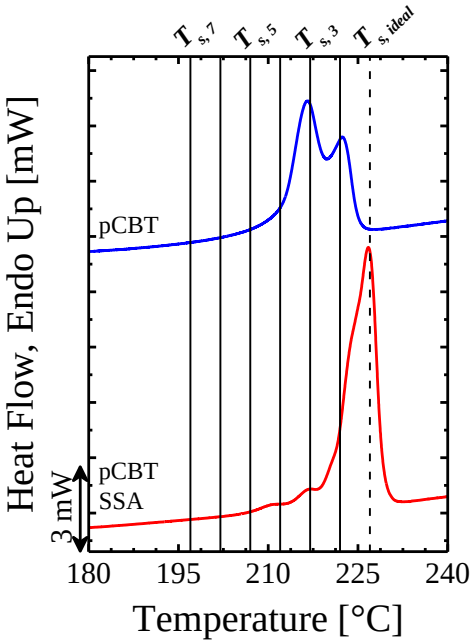

Figure 46. DSC heating scans for pCBT before (blue curve) and after (red curve) SSA thermal fractionation. The solid vertical lines represented the values of T_s temperature employed for thermal fractionation while the dashed vertical line indicates the $T_{s,ideal}$ for pCBT.

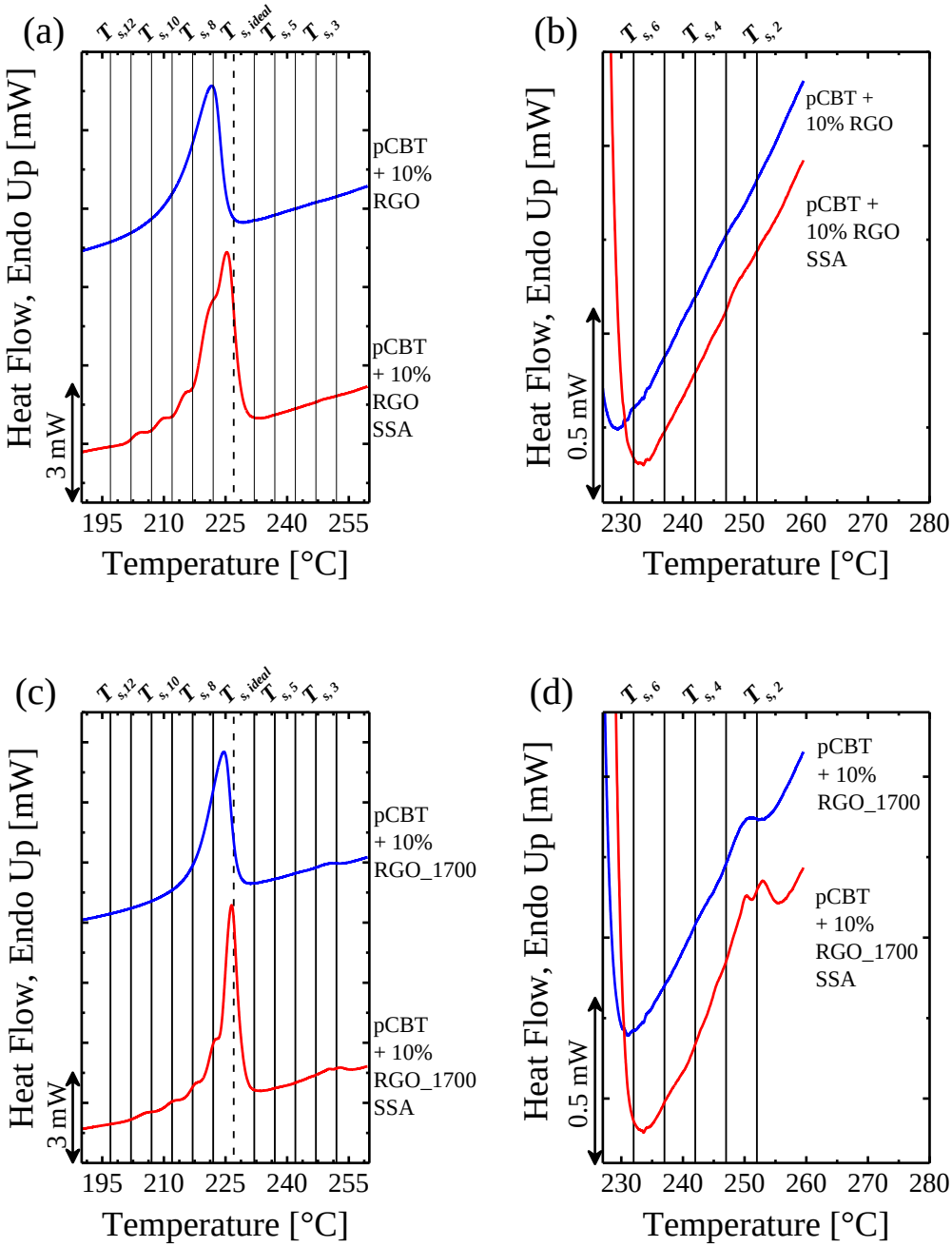

Figure 47. DSC heating scans for (a) pCBT + 10% RGO and (c) pCBT + 10% RGO_1700, before (blue curves) and after (red curves) SSA thermal fractionation. The effect of thermal fraction on the high temperature melting phase is reported in (b) for pCBT + 10% RGO and (d) for pCBT + 10% RGO_1700. The solid vertical lines represented the values of T_s temperature employed for thermal fractionation while the dashed vertical line indicates the $T_{s,ideal}$ for pCBT

Successive self-nucleation and annealing experiments revealed that pCBT can be fractionated, indicating a molecular segregation owed to chain length differences, considering that pCBT is a linear polymer. While the addition of rGO nanoflakes does not significantly affect thermal fractionation of "standard" pCBT melting peak, the characterization of the high stability fraction reveals that this is fractionable, further confirming the polymeric nature of this fraction.

6.2 Polymer chain organization

The different experiments, performed exploiting DSC, revealed that the higher melting/crystallization temperature crystalline population is constituted by thick polymer crystals, which can be annealed and fractionated. However, DSC measurements did not provide any information on the crystalline structure of the new peak. For this reason, WAXS experiments were performed first at room temperature, then heating specimens to try to maximize the diffraction pattern of the high melting/crystallization phase.

6.2.1 Room temperature WAXS

WAXS patterns collected via transmission geometry on pCBT, pCBT + 10% RGO and pCBT + 10% RGO_1700 are reported in Figure 48. Independently on the presence of rGO nanoflakes, all the WAXS patterns revealed peaks centered at diffraction angle (2Θ) 8.9° (001), 16.0° ($0\bar{1}1$), 17.2° (010), 20.5° ($\bar{1}10$), 23.2° (100), 25.3° ($1\bar{1}1$), 29.2° (101) and 31.2° ($11\bar{1}$), thus indicating that pCBT crystallized in its alpha crystalline form [203-205]. The appearance of a shoulder at $2\Theta \approx 26.2°$ in pCBT nanocomposites, was related to the (002) reflections of graphite [35], which is expected in the presence of rGO nanoflakes with thickness in the range of several nanometers. WAXS measurements performed with the incident X-rays perpendicular to the compression direction (Figure 48a) show a tiny signal related to the presence of rGO, in both nanocomposites.

WAXS patterns collected setting the incident X-rays parallel to the compression direction (Figure 48b) displayed a more intense peak at ~ 26.2°, thus evidencing a preferential orientation of nanoflakes parallel to the specimen surface, which is expected given their high aspect ratio. Furthermore, a clear anisotropy is observed for pCBT signals in nanocomposites, with polymer chains preferentially aligned parallel to the rGO sheets, especially in the case of pCBT + RGO_1700, as observable by differences between the (100) and ($1\bar{1}1$) reflections in patterns

collected perpendicular (Figure 48a) and parallel (Figure 48b) to the compression direction.

The anisotropy in pCBT nanocomposites can be more clearly observed in the differences between 2D WAXS patterns collected for pCBT (Figure 49) and nanocomposites (Figure 50 and Figure 51 for nanocomposites containing RGO and RGO_1700, respectively). In particular, a strong orientation can be observed in 2D patterns for pCBT + 10% RGO_1700 collected parallel to the compression direction (Figure 51b).

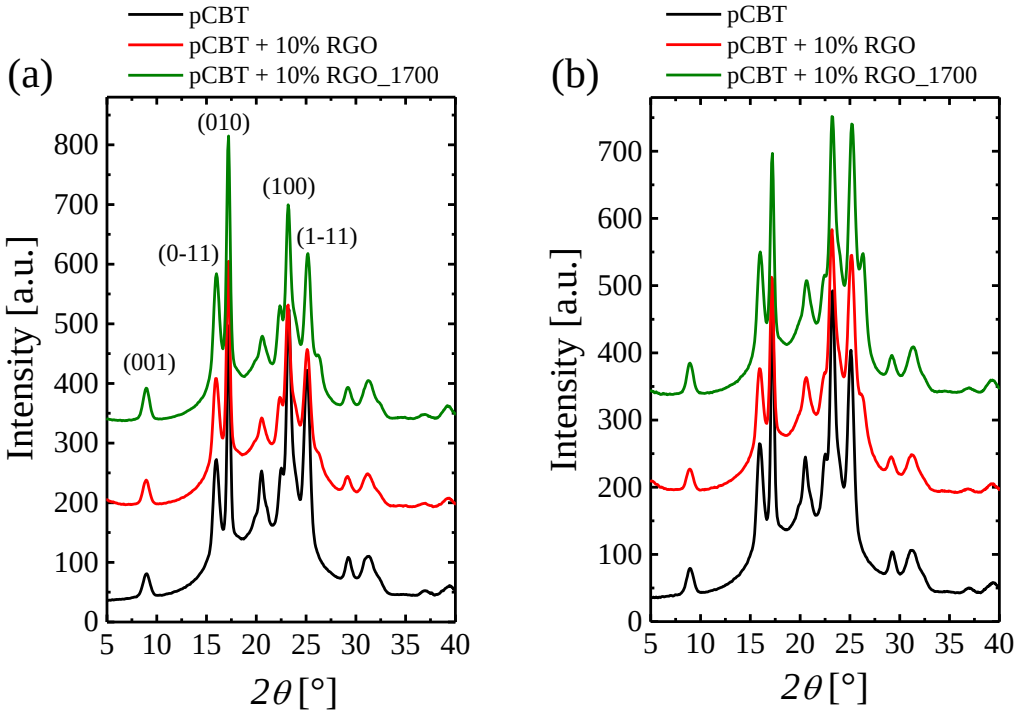

Figure 48. WAXS patterns measured via transmission geometry on pCBT, pCBT + RGO and pCBT + RGO_1700. WAXS measured (a) perpendicular and (b) parallel to the compression direction.

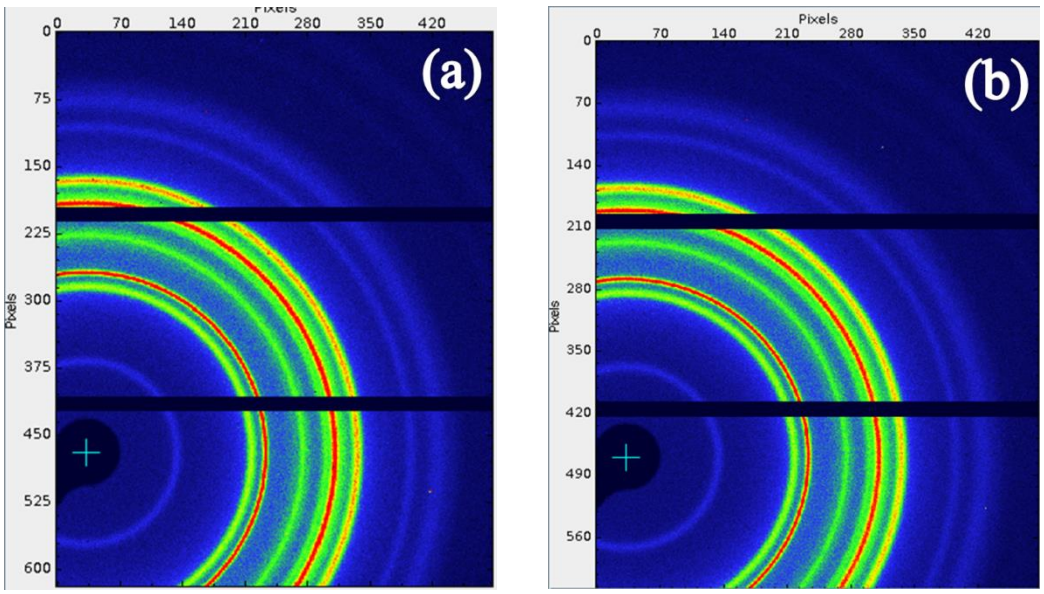

Figure 49. 2D WAXS patterns measured via transmission geometry on pCBT (a) parallel and (b) perpendicular to the compression direction.

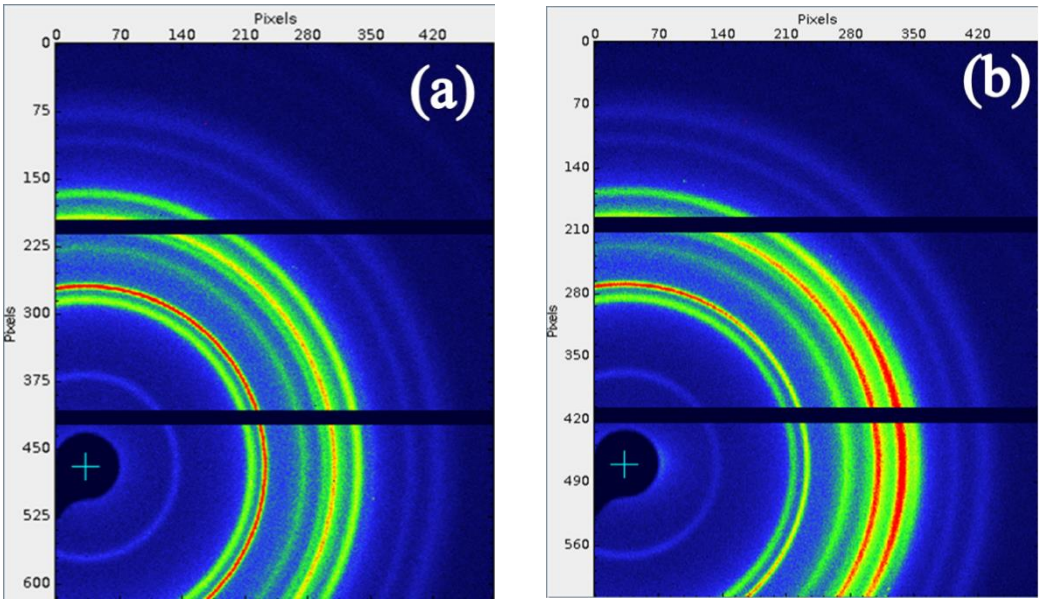

Figure 50. 2D WAXS patterns measured via transmission geometry on pCBT + 10% RGO (a) parallel and (b) perpendicular to the compression direction

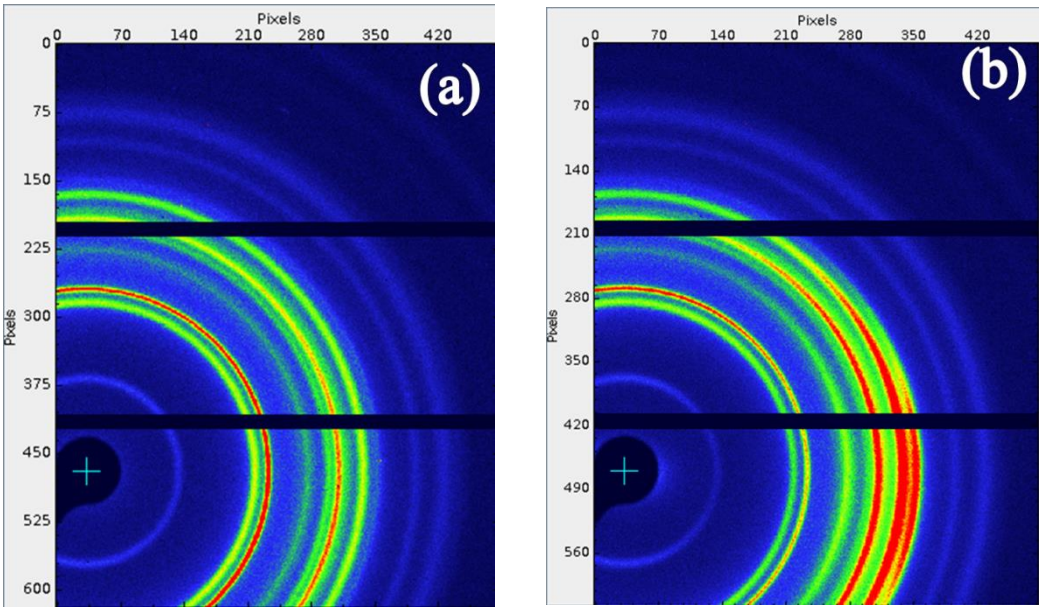

Figure 51. 2D WAXS patterns measured via transmission geometry on pCBT + 10% RGO_1700 (a) parallel and (b) perpendicular to the compression direction

Beside marked anisotropy in the polymer nanocomposites, neither peak shift nor new peaks were found in the diffraction pattern of pCBT nanocomposites vs. neat pCBT, thus suggesting the high temperature melting/crystallization fraction is not related to a new crystalline phase. To gain more insight on the crystalline organization of the high melting point fraction, *in situ* variable temperature WAXS measurements were carried out, aiming at the melting of the pCBT main crystal fraction while preserving the highly stable crystals.

6.2.2 Temperature assisted WAXS

Variable temperature *In situ* WAXS patterns collected for pure pCBT are reported in Figure 52. Starting from the top of the figure, the four red curves represent the diffraction patterns collected at the reported temperature during heating. While diffractogram is fully consistent with the one collected the room temperature (Figure 48a), the main diffraction peaks are clearly shifted to slightly lower scattering angle during heating, owing to the thermal expansion of the polymer matrix occurring during heating [204]. At 235 °C, only an amorphous halo was observed, indicating for a complete melting of polymer crystals, accordingly with DSC results (Figure 38b). The subsequent pattern (black curve in Figure 52) was collected at 260 °C, which is the temperature used in DSC experiments to erase the thermal history of pCBT, and, obviously, no diffraction peaks were observed.

After melting was complete and the thermal history was properly erase, temperature was decreased and resulting diffractograms are reported in blue. During cooling, no crystalline signals appeared down to 220 °C. When the temperature was set to 210 °C, the first diffraction peaks of pCBT became visible, related to the planes $(0\bar{1}1)$, (010), $(\bar{1}11)$, (100) and $(1\bar{1}1)$, thus evidencing the onset of crystallization. This result is consistent with DSC isothermal crystallization tests, for which 210 °C was the maximum isothermal condition at which crystallization of pCBT was achieved (Figure 41a). Further decreasing the temperature resulted in the intensification of diffraction patterns and in the shift of peaks to higher 2Θ values, which are related to the completion of pCBT crystallization and to the shrinkage of pCBT unit cell during cooling [204], respectively.

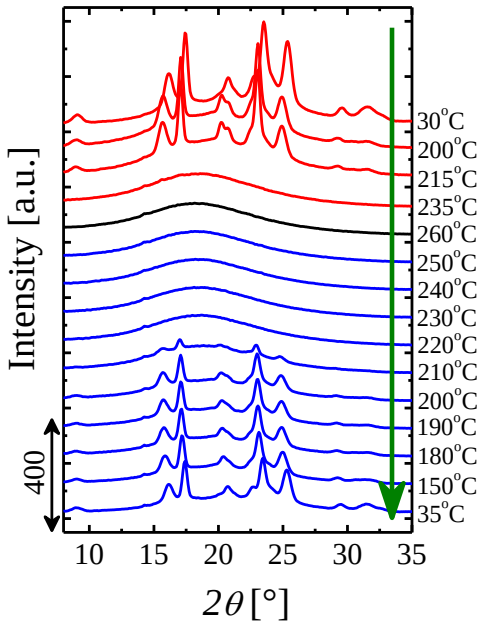

Figure 52. *In situ* WAXS diffraction patterns collected at different temperatures for pure pCBT. Red and blue curves represents the patterns collected during heating and cooling scans, respectively. The black pattern was collected at 260°C, *i.e.* the temperature at which was erased the thermal history of the material. On the right are reported the temperatures at which was collected each pattern, whereas the arrow indicates the measurement sequence.

Variable temperature WAXS patterns collected for pCBT + 10% RGO and pCBT + 10% RGO_1700 at different temperatures are reported in Figure 53a and Figure 53b, respectively. Diffraction patterns were collected on heating and

cooling scans following the same thermal protocol used for pure pCBT. The red and the blue diffractograms are related to patterns collected during heating and cooling scans, respectively, while the black one represent the scattering pattern recorded at the temperature selected to completely erase the thermal history of pCBT, *i.e.* 260 °C.

In situ measurements on pCBT + 10% RGO (Figure 53a) revealed a similar behavior to that observed for pure pCBT (Figure 52) during heating scans, with the disappearance of peaks related to polymer crystals for temperatures ≥ 235 °C. As expected, the presence of the graphite introduced a new peak located at ~ 26.5°, which is independent on the temperature. During cooling scans, crystallization occur in similar way to that of pCBT, with the simultaneous appearance of the same diffraction peaks related to $(0\bar{1}1)$, (010), $(\bar{1}11)$, (100) and $(1\bar{1}1)$ planes. However, it is worth observing that these peaks appeared at 220 °C, whereas for the pure polymer a higher super cooling (*i.e.* cooling down to 210 °C) was required for the formation of polymer crystals. This is agreement with results above reported for isothermal crystallization experiments carried out by DSC (Figure 41a). However, in WAXS measurements for pCBT + 10% RGO no detectable diffraction signals of the high stability crystalline fraction observed by non-isothermal DSC, SN and SSA were found. This is likely due to the the extremely low amount of this fraction, ~ 1 J g^{-1} measured by DSC (Table 13 and Table 14), which is probably below the WAXS sensitivity.

Variable temperature WAXS measurements on pCBT + 10% RGO_1700 (Figure 53b and Figure 53c) revealed interesting differences compared to pCBT and pCBT + 10% RGO. First, the diffraction peak at $2\Theta \approx 26.5°$, related to the presence rGO, is clearly more intense respect to that observed in pCBT + 10% RGO (Figure 53a). This is partially explained by the lower defectiveness and higher structural order of RGO_1700, as widely discussed in chapter 3, but there may also be an additional effect of higher orientation obtained with annealed RGO. More interestingly, persistence of crystalline organization was found during heating until 235 °C, thus reflecting the presence of highly stable crystalline fraction. Upon cooling steps, at 240 °C traces of diffraction signals appear at $2\Theta \approx$ 15.9°, 17.1° and 23.1° (indicated by the arrows in Figure 53c), related to the (0-11), (010) and (100) planes, typical of pCBT. Further cooling to 230 °C, all the diffraction peaks related to the pCBT alpha phase were clearly observed, while at 220 °C the peak intensity achieved the maximum value, being the crystallization completed. Comparing these results with those obtained by isothermal

crystallization experiments (performed by DSC, Figure 41a), it appears that the complete crystallization observed by WAXS at 220 °C is in agreement with the maximum isothermal temperature used in isothermal DSC tests (219 °C). However, the presence of pCBT diffraction patterns at 235 °C in heating scans and the appearance of the first peaks related to pCBT crystals at 240 °C cannot be regarded as signals related to the main crystallization step of pCBT. Indeed, at these high temperatures only the high stability fraction can survive, in agreement with non-isothermal DSC experiments.

Further trying to characterize the high melting phase, WAXS were performed on pCBT + 50% RGO_1700 prepared by solution mixing and hot compressed into a film. Results (Figure 54) are well consistent and similar with those above described for pCBT + 10% RGO_1700 even if the first crystalline peak related to pCBT crystals, ~ 17.0 ° (010), is observed at 230 °C (arrow in Figure 54b), despite the general lower intensity of pCBT diffraction pattern respect to that of pCBT + 10% RGO_1700.

WAXS results present here prove this high stability fraction to have the same diffraction pattern observed for the standard pCBT alpha phase. This suggest the higher crystal stability has to be explained by a thicker stack of pCBT chain crystals, similarly to what is considered as ideal crystals made of infinite chain stack. Indeed, the measured melting temperature was very close to the equilibrium melting temperature calculated for pure pCBT. This demonstrate, for the first time, the capability of rGO nanoflakes not only to nucleate pCBT crystal but also to determine a very regular arrangement of chains into highly stable crystals, most likely due to the polymer/nanofiller interface. The importance of such interfacial contact, is further highlighted by the differences between nanocomposites containing RGO and annealed RGO, which demonstrate that structurally ordered and low defectiveness nanoflakes obtained after annealing are much more efficient in promoting the ordered arrangement of polymer chains at the interface.

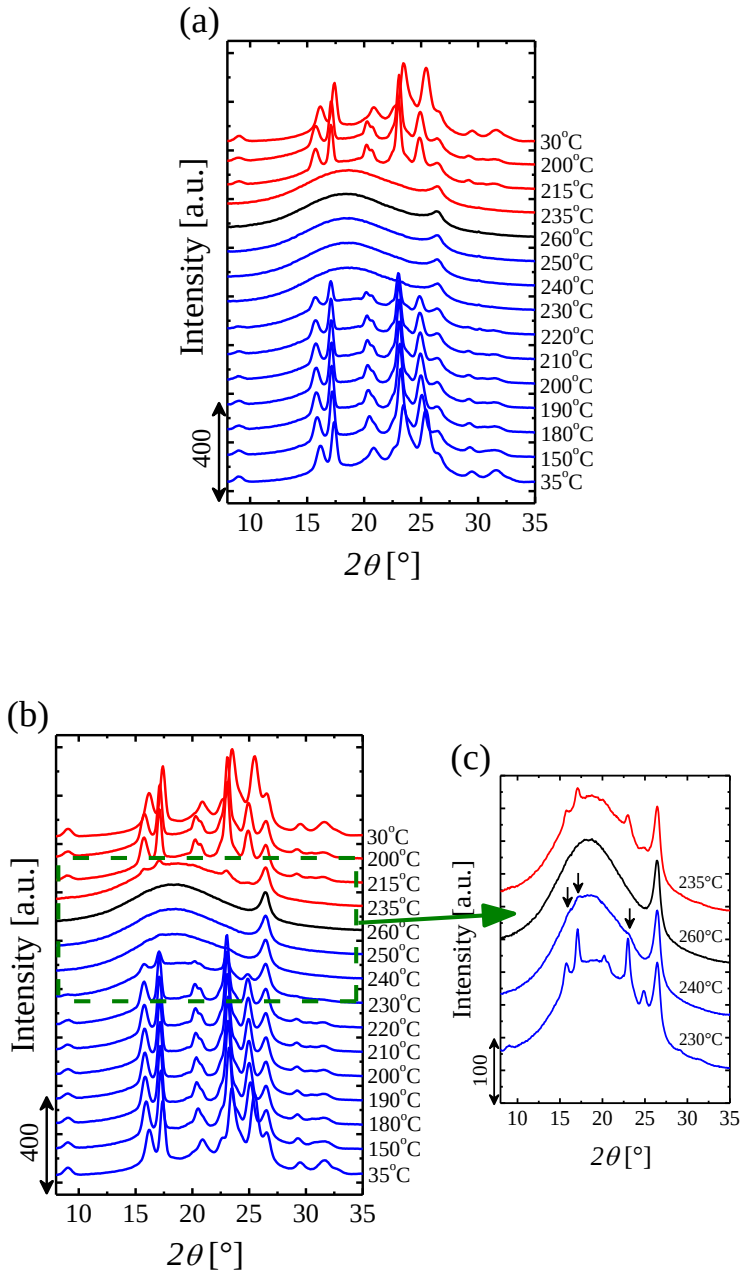

Figure 53. ***In situ*** **WAXS diffraction patterns collected at different temperatures for (a) pCBT + 10% RGO and (b) pCBT + 10% RGO_1700. Selected** ***in situ*** **WAXS diffraction patterns for pCBT + 10% RGO_1700 (c). The three arrows (c) indicates the first pCBT crystalline peaks which appear in cooling scans. Red and blue curves represent the patterns collected during heating and cooling scans, respectively. The black pattern was collected at 260°C,** ***i.e.*** **the temperature selected to erase the**

thermal history. On the right are reported the temperatures at which was collected each pattern.

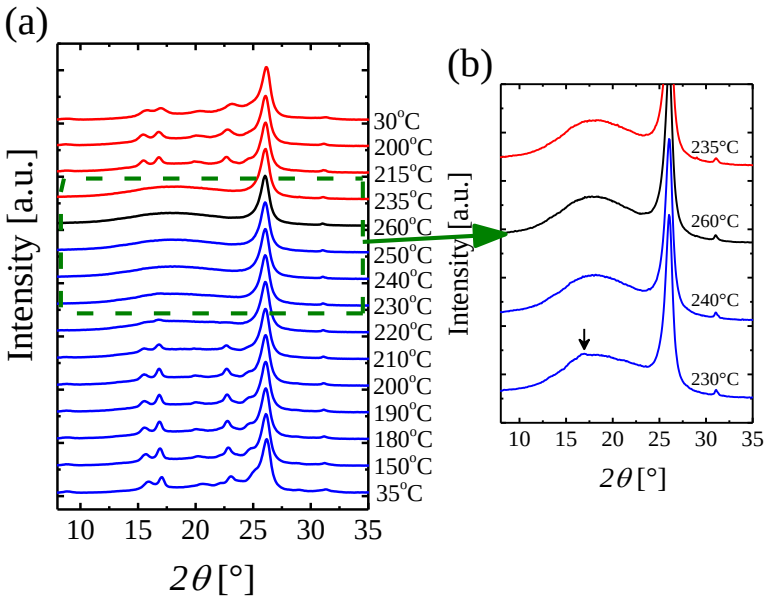

Figure 54. *In situ* WAXS diffraction patterns collected at different temperatures for pCBT + 50% RGO_1700 (a). Selected *in situ* WAXS diffraction patterns (b). The arrow (b) indicates the first pCBT crystalline peak which appear in cooling scans. Red and blue curves represent the patterns collected during heating and cooling scans, respectively. The black pattern was collected at 260°C, *i.e.* the temperature selected to erase the thermal history. On the right are reported the temperatures at which was collected each pattern.

6.3 Conclusions

In this chapter the effects of reduced graphene oxide nanoflakes on the crystallization of *in-situ* polymerized poly(butylene terephthalate) were studied in details. The addition of rGO strongly affected melting and crystallization behavior of pCBT. In the presence of rGO, the crystallization peak temperature was shifted to higher temperature values and the melting/recrystallization of thin crystals, typically observed during heating scans for neat pCBT, was suppressed, thus indicating the formation of thicker crystals during cooling. Furthermore, a new peak at higher temperature was observed in both DSC heating and cooling scans, especially in nanocomposites containing annealed rGO. This peak is related to the formation of a thick stack of chain crystals at the pCBT/RGO interface, promoted by the change in the surface chemistry in annealed RGO.

Isothermal crystallization tests revealed faster crystallization in the presence of rGO, without altering the crystallization mechanism of pCBT. In fact, an Avrami index of about 2 was calculated for both neat pCBT and nanocomposites, thus resulting in the nucleation of instantaneous axialites.

Self-nucleation experiments determined a nucleation efficiency (NE) of 164% and 270% in the presence of pristine and annealed nanoparticles, respectively, thus indicating a super-nucleating effect. Self-nucleation and successive annealing tests revealed that the crystalline population with high melting/crystallization can be fractionated with the higher melting fraction centered at ~ 253 °C, which is close to the values of the pCBT equilibrium melting temperature reported in literature. These are a further confirmation of the polymeric nature of this phase and the possible formation of extended chain crystals.

Finally, WAXS experiments showed that the polymer chains and rGO oriented simultaneously, the higher orientation obtained with annealed rGO. Tests at different temperatures showed the presence of crystalline reflections at temperatures higher than the melting temperature of neat pCBT: these traces were related to the same crystalline structure of neat pCBT (α-form). The orientation and the crystalline form observed for the new phase gave a further proof to the chain conformation as thick stack of extended chain crystals, especially in presence of thermally-annealed rGO with low defectiveness and oxidation.

Chapter 7

Effects of processing conditions on nanocomposite conductivity

Results reported in the chapter 5 evidenced the strict dependence of aspect ratio and nanocomposite properties upon processing conditions, suggesting the need for a careful optimization of mixing parameters in order to achieve high dispersion and distribution of nanoparticles while retaining a high aspect ratio of the nanoflakes. In this chapter, the effect of different processing conditions, *i.e.*, processing temperature, time and shear rate, on the properties of poly (butylene terephthalate) nanocomposites is addressed. The nanoparticle content and type were kept constant, *i.e.* nanocomposites were prepared polymerizing CBT into pCBT in presence of 5 wt.% of GNP-2. This type of graphite nanoplatelets was not used in the previous chapters, but is characterized by low defectiveness and high aspect ratio, as reported in chapter 3. In particular processing temperature (240°C or 260°C), extrusion time (5 or 10 minutes) and shear rate (50 or 100 rpm) were varied by means of a full factorial design of experiment approach, leading to the preparation of polybutylene terephthalate/GNP nanocomposite in 8 different processing conditions. Furthermore, pure pCBT was synthetized (extrusion parameters: 240°C, 5 minutes and 50 rpm) as reference material. The different nanocomposites are labeled as pCBT_GNP/*x*/*y*/*z* where *x* is the temperature in °C, *y* the extrusion time in min and *z* the shear rate in rpm. Processing conditions, coupled with nanocomposites labeling, are reported in Table 17.

Table 17. Labeling and processing conditions used for pCBT and pCBT nanocomposites

Material	Processing parameters		
	Temperature [°C]	Time [Minutes]	Shear rate [rpm]
pCBT	240	5	50
pCBT_GNP-2/240/5/50	240	5	50
pCBT_GNP-2/240/10/50	240	10	50
pCBT_GNP-2/240/5/100	240	5	100
pCBT_GNP-2/240/10/100	240	10	100
pCBT_GNP-2/260/5/50	260	5	50
pCBT_GNP-2/260/10/50	260	10	50
pCBT_GNP-2/260/5/100	260	5	100
pCBT_GNP-2/260/10/100	260	10	100

7.1 Characterization

7.1.1 Polymerization evaluation

Differential scanning calorimetry

The polymerization of CBT into pCBT, and the effect of the processing conditions on melting/crystallization behavior of the different nanocomposites, were monitored by differential scanning calorimetry (Figure 55 and Table 18). Heating curves demonstrate that no residual traces of the characteristic melting peaks of the oligomer were observed for all the nanocomposites. Furthermore, in heating scans, the presence of only one endothermic peak for pCBT_GNP-2 nanocomposites indicates the formation of stable crystals during cooling. Instead, in pure pCBT the presence of an additional endothermic peak at lower temperatures was related to melting/recrystallization of thin crystals [178, 206]. The presence of carbon nanoflakes usually affects the crystallization behavior of

the polymer matrix, as demonstrated in the previous chapters: in fact, while pure pCBT has a crystallization temperature of 192.2 °C, values ranging between 195.2 °C and 204.6 °C were measured for pCBT + GNP-2 nanocomposites, the highest for pCBT_GNP-2/240/10/100, thus indicating a pronounced nucleating effect of GNP. Crystallinity degree (Table 18) of pure pCBT was estimated equal to 49.2%, while for nanocomposites values ranging between 45.9% and 53.6% were calculated. The comparison between the different materials reveals that none of the three processing parameters (temperature, time and shear rate) or their combination have a clear effect on neither crystallinity nor crystallization peak temperature.

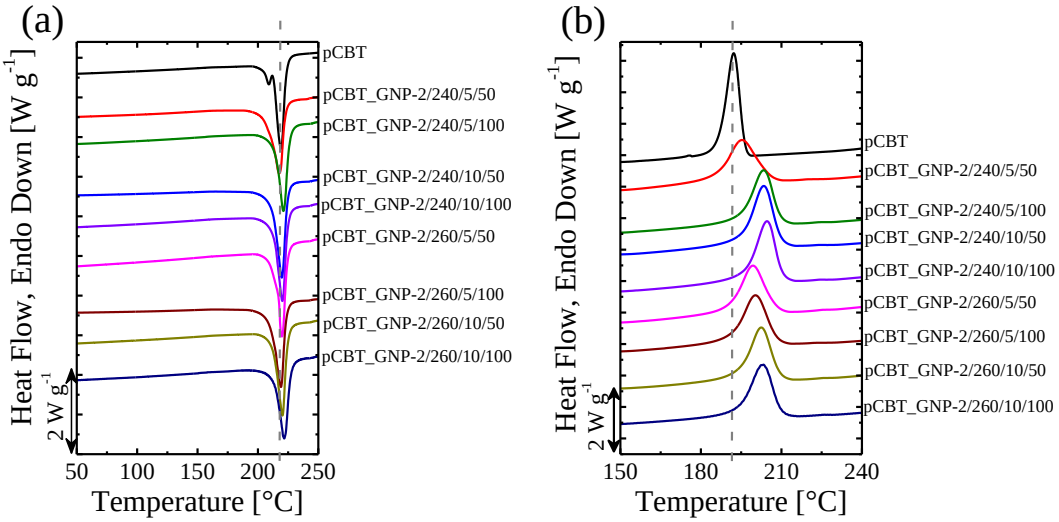

Figure 55. DSC curves for pCBT and pCBT_GNP-2 nanocomposites. a) Heating and b) cooling scans, both carried out at 20°C/min

Table 18. Melting temperature (T_m), crystallization temperature (T_c) and crystallinity (X_c) for pCBT and pCBT_GNP-2 nanocomposites

Nanocomposite	T_m [°C]	T_c [°C]	X_c [%]
pCBT	219.1	192.2	49.2
pCBT_GNP-2/240/5/50	217.5	195.2	48.4
pCBT_GNP-2/240/10/50	219.8	203.4	53.6
pCBT_GNP-2/240/5/100	221.1	203.4	47.0

pCBT_GNP-2/240/10/100	220.2	204.6	50.5
pCBT_GNP-2/260/5/50	219.9	199.4	45.9
pCBT_GNP-2/260/10/50	220.3	202.5	46.0
pCBT_GNP-2/260/5/100	219.1	200.3	49.1
pCBT_GNP-2/260/10/100	221.8	203.3	46.7

Viscometric molecular weight determination

The average viscosimetric molecular weight [175] of pCBT samples was determined, after GNP extraction, from the intrinsic viscosity of pCBT solutions and results are summarized in Table 19. The value of the M_v calculated for pCBT was 40500 g mol^{-1}, achieving a sufficient polymerization degree of pCBT using the extrusion process. The presence of graphene nanoparticles affects the ring-opening polymerization of CBT, with a general reduction in the molecular weight of the polymer matrix, in agreement with Fabbri *et al.* [147]. Indeed, the average molecular weight of pCBT including 5 wt.% of GNP-2 decreased in more than 40% respect to the value of the neat pCBT, for all nanocomposites. None of the processing parameters or their combination exhibits major effects on the final molecular weight of the neat polymer, thus indicating that M_v is mainly affected by the presence of nanoparticles. However, it is worth observing that the combination of high processing time and low temperature leads to the obtainment of the highest molecular weight suggesting that low polymerization temperature is beneficial to reduce chain scission during mixing.

Table 19. Viscosity values extrapolated for pCBT and pCBT_GNP-2 nanocomposites

Nanocomposite	M_v [kg mol^{-1}]
pCBT	40.5 ± 0.5
pCBT_GNP-2/240/5/50	24.8 ± 0.1
pCBT_GNP-2/240/10/50	27.1 ± 0.1

pCBT_GNP-2/240/5/100	28.7 ± 0.1
pCBT_GNP-2/240/10/100	28.5 ± 0.3
pCBT_GNP-2/260/5/50	25.5 ± 0.1
pCBT_GNP-2/260/10/50	25.8 ± 0.1
pCBT_GNP-2/260/5/100	22.9 ± 0.2
pCBT_GNP-2/260/10/100	27.6 ± 0.3

7.1.3 Nanoparticle organization

Rheology

The study of GNP dispersion and distribution, in pCBT, was performed by means of linear viscoelasticity in the molten state; indeed, complex viscosity, η*, and elastic modulus, G', are well-known to be related to nanoparticle amount and organization in a polymer matrix [179, 184]. G' and η* plots for pCBT and its nanocomposites, obtained from dynamic frequency tests, are reported in Figure 56 as a function of deformation frequency. pCBT exhibits the typical behavior of pure polymers in linear regime, with viscosity approximately independent on the frequency and modulus decreasing when frequency decreases; it is worth noting that, owing to the instrument limits, it was not possible to evaluate G' (for pure pCBT) at frequencies below $\omega \approx 6$ rad s^{-1}. The inclusion of GNP leads to higher G' and η* in the whole frequency range: for all the nanocomposites, a strong shear thinning effect (decrease of the viscosity as frequency increases, extending over two decades in the explored frequency range) and a weak G' dependence on the frequency were observed, thus indicating the formation of a percolated structure constituted by graphite nanoplatelets [51, 99, 179]. Furthermore, the formation of the solid like network in pCBT nanocomposites is evidenced by a predominance of the elastic response in the whole frequency range, while in pure pCBT viscoelastic properties are mainly dominated by the viscous response (Figure 56c). To further investigate the effect of the different processing conditions on the viscoelastic properties of pCBT_GNP-2 nanocomposites, G' and η* values at low frequencies ($\omega \approx 1$ rad s^{-1}) were compared (Table 20). Results show that viscoelastic properties of pCBT nanocomposites were weakly affected by the extrusion temperature; in fact, for nanocomposites prepared with the same processing time and shear rate, slightly higher modulus and viscosity

values were measured when lower temperatures were used for nanocomposite preparation (*i.e.*, G' and η* values of ~ 3.1 · 10^3 Pa and ~ 3.7 · 10^3 Pa s^{-1}, respectively, were measured for pCBT_GNP/240/5/50, whereas pCBT_GNP/260/5/50 showed G' ≈ 1.1 · 10^3 Pa and η* ≈ 1.5 · 10^3 Pa s^{-1}), suggesting a denser percolation network obtained at the lower processing temperature. On the other hand, no significant trends on both viscosity and elastic modulus were observed varying time or shear rate.

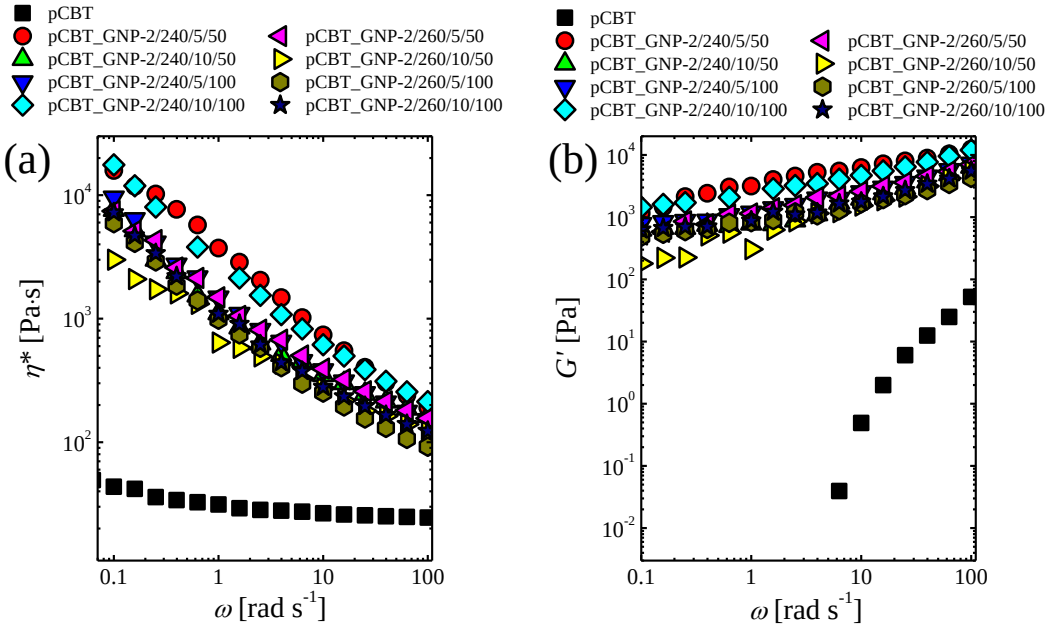

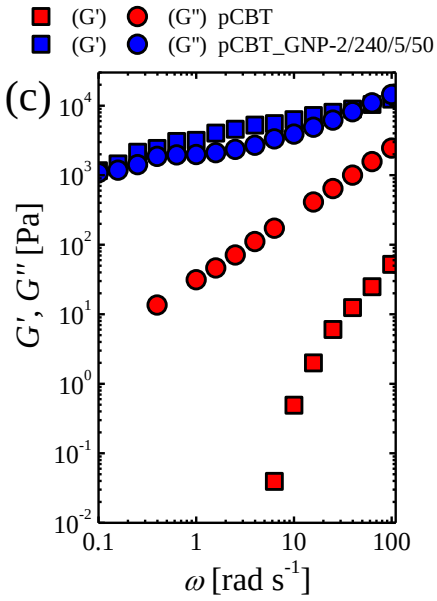

Figure 56. Dynamic frequency sweep test at 250°C for pCBT and pCBT + GNP-2 nanocomposites. (a) η* and (b) G' as a function of the angular frequency. (c) G' and G" as a function of the angular frequency for pCBT and pCBT_GNP-2/240/50

Table 20. Elastic modulus and viscosity (both measured at ω ≈ 1 rad/s) for pCBT and pCBT_GNP-2 nanocomposites

Nanocomposite	G' (ω ≈ 1 rad s^{-1}) [Pa]	η* (ω ≈ 1 rad s^{-1}) [Pa·s]
pCBT	-	30
pCBT_GNP-2/240/5/50	3164	3732
pCBT_GNP-2/240/10/50	783	1103
pCBT_GNP-2/240/5/100	1191	1435
pCBT_GNP-2/240/10/100	2422	2578
pCBT_GNP-2/260/5/50	1141	1498
pCBT_GNP-2/260/10/50	305	812
pCBT_GNP-2/260/5/100	831	963
pCBT_GNP-2/260/10/100	874	1071

7.1.3 Electrical conductivity

The organization of conductive particles in a solid-like network is crucial for the preparation of electrically conductive materials [51, 207]: in particular, the higher the density of the percolation network, the higher the electrical conductivity. Pure pCBT displays an electrical conductivity in the range of 10^{-13} S m^{-1} [181], which is typical for pure polymers, whereas the addition of graphite nanoplatelets leads to a sharp increase (see Figure 57 and Table 21) with values ranging between $2.75 \cdot 10^{-5}$ and $5.89 \cdot 10^{-3}$ S m^{-1} for pCBT_GNP-2/260/10/100 and pCBT_GNP-2/240/5/50, respectively, thus indicating that all the nanocomposites are well above the electrical percolation threshold. It is clearly observable that the highest and the lowest electrical conductivity values were measured using the milder (low time, low shear rate) and the severer (high time, high shear rate) processing conditions, respectively. Temperature is also affecting the conductivity values, generally leading to higher electrical performance with lower processing temperature despite the opposite effect was observed in pCBT_GNP-2/5/10. These suggest a strong effect of the harsher processing conditions, with a likely reduction of the GNP aspect ratio during extrusion for long time and/or high shear rates and/or high temperatures [76, 208]. In fact, nanoparticle aspect ratio was reported to affect electrical conductivities of polymer nanocomposites, with higher values obtained when high aspect ratio nanoparticles were used [188, 209].

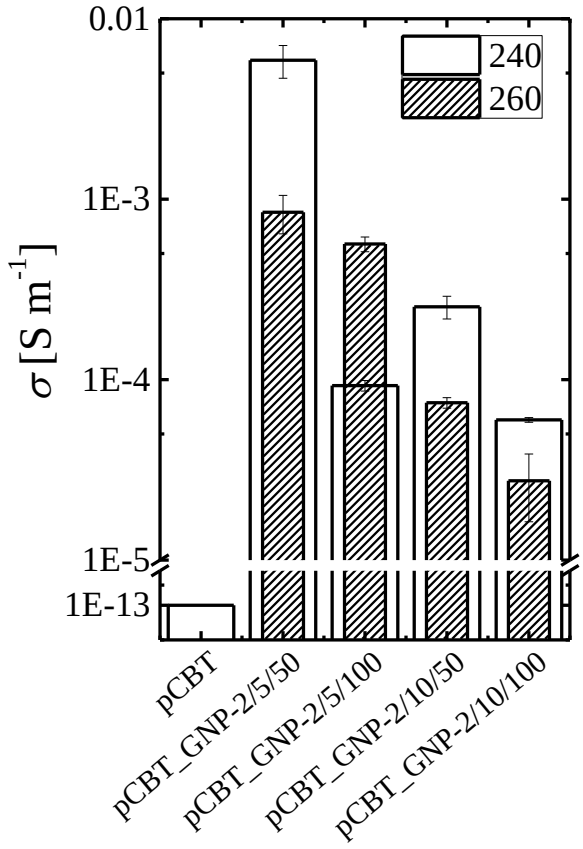

Figure 57. Electrical conductivity of pCBT + GNP-2 as function of the different extrusion parameters

Table 21. Electrical conductivity data for pCBT nanocomposites as a function of processing parameters

Electrical conductivity [S m^{-1}]		
Nanocomposite	240 °C	260°C
pCBT_GNP-2/5/50	σ = (5.9 ± 0.1) E-3	σ = (8.5 ± 2.0) E-4
pCBT_GNP-2/5/100	σ = (9.3 ± 0.6) E-5	σ = (5.6 ± 0.5) E-4
pCBT_GNP-2/10/50	σ = (2.5 ± 0.4) E-4	σ = (7.4 ± 0.5) E-5
pCBT_GNP-2/10/100	σ = (6.0 ± 0.2) E-5	σ = (2.8 ± 1.1) E-5

7.1.4 Thermal conductivity

Bulk thermal conductivity results for pCBT and pCBT_GNP-2 nanocomposites as a function of processing parameters are reported in Figure 58 and Table 22. Pure pCBT exhibits a thermal conductivity of ~ 0.24 W m^{-1} K^{-1} which is consistent with results reported in literature for semi-crystalline polymers [1]. The addition of GNP leads to an improvement in the conductivity properties with values ranging between 0.72 and 0.98 W m^{-1} K^{-1} for pCBT_GNP/260/10/100 and pCBT_GNP/240/5/50, respectively, thus indicating an increase between 3-fold and 4-fold, with respect to pure polymer. Thermal conductivity results, as a function of the different parameters, exhibit a trend similar to that observed for electrical conductivities (Figure 58), with the highest conductivity values obtained combining short time and low shear rate. Indeed, the reduction in thermal conductivity between the nanocomposite obtained in the mildest conditions (240/5/50) *vs.* the one prepared in the harshest conditions (260/10/100) is as much as 26%. This fact is most likely related to the reduction in nanoflake aspect ratio, which was reported to have a detrimental effect on the improvement of nanocomposites thermal conductivity [189].

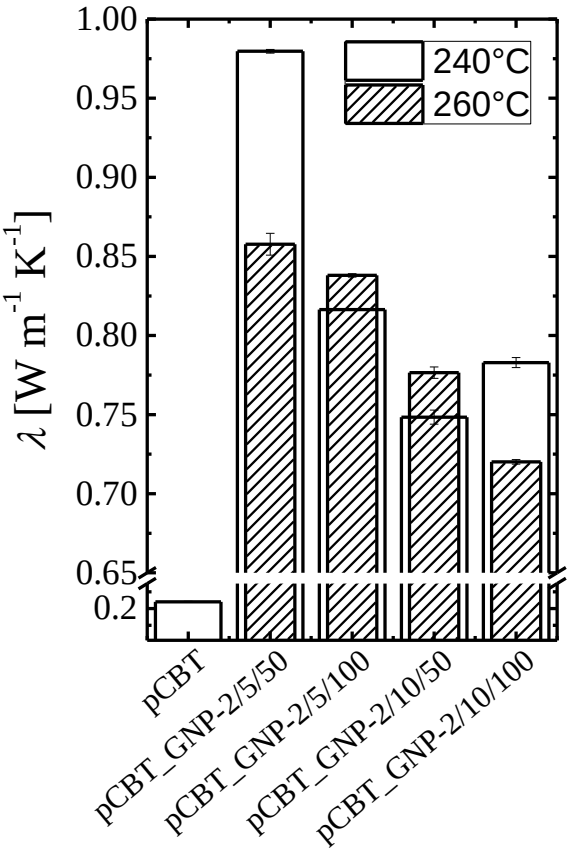

Figure 58. Thermal conductivity of pCBT and pCBT + GNP-2 as function of the different extrusion parameters

Table 22. Thermal conductivity data for pCBT nanocomposites as a function of processing parameters

Thermal Conductivity [W m^{-1} K^{-1}]		
Nanocomposite	240 °C	260°C
pCBT_GNP-2/5/50	$\lambda = 0.980 \pm 0.001$	$\lambda = 0.858 \pm 0.007$
pCBT_GNP-2/5/100	$\lambda = 0.816 \pm 0.001$	$\lambda = 0.838 \pm 0.001$
pCBT_GNP-2/10/50	$\lambda = 0.748 \pm 0.004$	$\lambda = 0.777 \pm 0.004$
pCBT_GNP-2/10/100	$\lambda = 0.783 \pm 0.003$	$\lambda = 0.720 \pm 0.001$

Beside the clear effect of mixing time and shear rate, for both electrical and thermal conductivity, the role of processing temperature appears to be complex as in some cases a decrease of conductivity was observed when increasing temperature, whereas the opposite trend was obtained. To further analyze the results obtained for the four main properties addressed (molecular weight, melt viscosity, electrical and thermal conductivity) upon the processing parameters, average values were calculated for properties of the four different formulations prepared with one processing parameter as a constant. This averaging was repeated for all the different properties and parameters, leading to average values suitable to compare performances obtained at the low and high setting points for each of the parameter (temperature, mixing time and shear rate). Results of this analysis are reported in Figure 59, in which averaged values calculated as above for low setting points, of the different parameters, were normalized to 1 and averaged values for high setting points were scaled accordingly. From this analysis it is clear that electrical conductivity is the property being affected the most by melt processing conditions: comparing the average value of the electrical conductivities at the lowest and highest setting points, systematically higher electrical conductivities were measured with the use of the lowest setting points, as increase by factors 4, 10 and 19 were obtained for temperature, time and shear rate, respectively, as compared with their highest setting points counterparts.

Beside the effect on electrical conductivity, the increase in mixing time decreases percolation density in the melt, indirectly evaluated from melt viscosity, as well as thermal conductivity, whereas a slight increase in molecular weight was obtained for longer processing time. The screw rotation rate has a larger effect in reducing both melt viscosity and thermal conductivity, with a slight increase of molecular weight. Finally, temperature increase was not found to be beneficial for any of the properties addressed, possibly due to side reactions or chain scission during melt mixing.

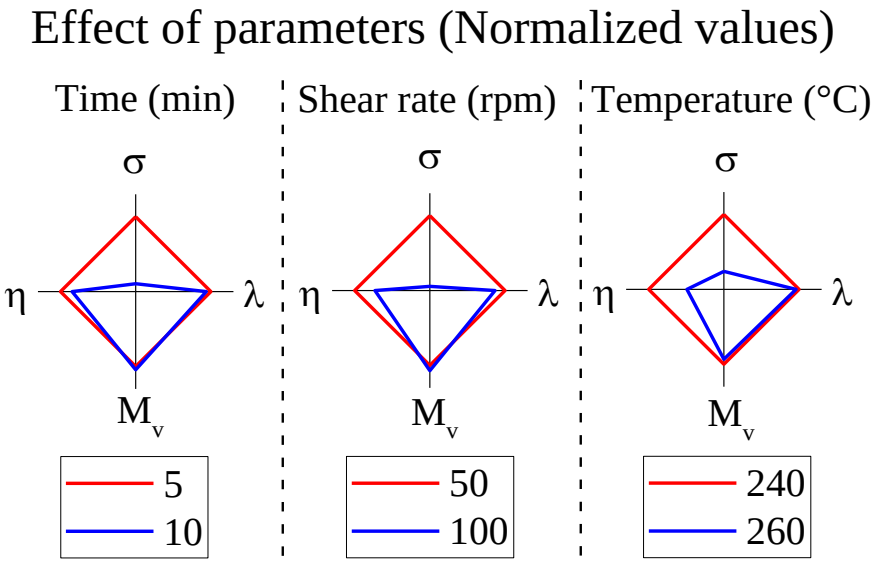

Figure 59. Effect of time, shear rate and temperature on electrical conductivity, thermal conductivity, molecular weight and viscosity of pCBT + GNP-2 nanocomposites. Each of the axis report averaged and normalized values for comparison between performance of higher *vs.* lower setting points. Scale on electrical conductivity is logarithmic.

Based on the results here showed it appears clear that the use of mild processing conditions is essential to maximize electrical and thermal properties of pCBT_GNP-2 nanocomposites. Despite the work reported in this chapter was not aimed to a full optimization of processing conditions, which would require both enlarging processing windows and considering additional parameters (*e.g.* screw profile), the results obtained should be taken into account when designing up-scaling of nanocomposites production onto industrial scale equipment, which is clearly beyond the scope of this paper.

Beside the effect of the addressed processing parameters, electrical and thermal conductivities are typically strongly affected by the GNP-2 content, increasing the amount of nanoparticle content is clearly expected to improve electrical and thermal conductivity. However, higher amount of GNP-2 is directly related to a significant increase in viscosity, which may also restrict the possible processing window.

7.2 Conclusions

In this chapter, the effect of different processing parameters on the properties of poly (butylene terephthalate) nanocomposites prepared via ring-opening polymerization of CBT in presence of graphite nanoplatelets was addressed. In particular, the present paper is focused on the effects of processing temperature, mixing time and shear rate on polymer molecular weight, nanoparticle dispersion as well as electrical and thermal conductivity of pCBT/GNP-2 nanocomposites.

Average viscometric molecular weight of pCBT was found to be significantly affected by the presence of nanoflakes, with a general reduction in the molecular weight, compared to pure pCBT, in the range of 40%, regardless of the processing parameters used for compounding. Despite the limited molecular weight obtained, a satisfactory dispersion and distribution of GNP-2 was observed, with the formation of a dense percolating networks, evidenced by the study of linear viscoelasticity in the molten state.

Electrical and thermal conductivity results showed similar trends with the highest conductivity values ($\sigma \approx 6 \cdot 10^{-3}$ S m^{-1} and $\lambda \approx 1.0$ W m^{-1} K^{-1}, respectively) obtained combining short time, low temperature and low shear rate, whereas the lowest values were obtained ($\sigma \approx 3 \cdot 10^{-5}$ S m^{-1} and $\lambda \approx 0.7$ W m^{-1} K^{-1}, respectively) setting the three parameters at the higher level (harsher processing conditions). These observations were related to the reduction of nanoflake aspect ratio upon ring-opening polymerization for longer time and greater shear rates. These results evidences the need for careful optimization of processing parameters during preparation of polymer nanocomposites containing graphene related materials.

General conclusions

This thesis was focused on the development of polymer/GRM nanocomposites by ring opening polymerization of cyclic butylene terephthalate (CBT) during melt mixing into poly (butylene terephthalate) (pCBT) in presence of different types of graphene-related materials. In particular, two different graphite nanoplatelets grade (GNP and GNP-2) and two types of reduced graphene oxide (RGO and RGO-2) were used. Based on the results obtained in this thesis, the following conclusions may be highlighted:

- Graphene-related materials may have very different properties depending on the preparation methods. Lateral size, thickness and oxidation degree must be carefully selected depending on the application targeted. GNP and RGO currently appear to be the most promising types of carbon nanofillers for polymer nanocomposites, coupling availability with properties.
- RGO flakes thermally reduced by conventional rapid heating, in the range of 1000 °C, typically present highly defective nanoflakes, mainly in terms of sp^3 carbons and remaining oxidized groups. Despite dispersion of these nanoparticles may lead to denser percolation networks compared to GNP at the same loading, the thermal and electrical conductivities of their nanocomposites showed different dependencies on RGO defectiveness. In fact, while electrical conductivity mostly depends on the density of the percolation network, thermal conductivity is extremely sensitive to nanoflake

defectiveness, so that pCBT/GNP were demonstrated to outperform pCBT/rGO at the same particle concentration. On the other hand, high temperature treatment at 1700 °C for 1 h in vacuum was demonstrated able to eliminate most of the oxidized species and to eliminate highly defective carbon, resulting in materials with a reduced defectiveness, while preserving the nanoflake aspect ratio. As expected, thermally annealed rGO allowed to obtain superior thermal conductivities, higher than those obtained with pristine rGO or GNP, thus evidencing that heat transfer in the composite is indeed optimized when coupling fine dispersion of nanoparticles and their high intrinsic conductivity. The exploitation of low defective and high aspect-ratio nanoparticles is mandatory for a successful improvement of polymer properties, especially regarding thermal conductivity.

- The exploitation of 5 wt.% RGO_1700 led to a bulk thermal conductivity $\lambda \approx 0.9$ W m^{-1} K^{-1}, which is higher than the ~ 0.5 W m^{-1} K^{-1} measured for nanocomposite containing the same amount of pristine RGO, thus proving the need for the exploitation of low defective nanoflakes. At the same content, nanocomposites containing low aspect ratio GNP exhibited a thermal conductivity of about 0.6 W m^{-1} K^{-1}. The exploitation of 5 wt.% of low defective and high aspect ratio GNP-2 led to thermal conductivity values in between 0.7 and 1.0 W m^{-1} K^{-1}, depending on the processing conditions. Furthermore, at the same nanoparticle content (5 wt.%), nanocomposite based on unpolymerized CBT and RGO_1700 showed a thermal conductivity value of ~ 1.5 W m^{-1} K^{-1}, *i.e.* the highest value measured at this concentration in this thesis, owed to the limited reduction of particle size during mixing compared to the pCBT nanocomposites. These results indicate that the proper selection of nanoparticle and mixing parameters are mandatory for the preparation of thermally conductive polymer nanocomposites. However, the lower aspect ratio of GNP made possible to prepare increase the filler content up to 30 wt.%, resulting in a bulk thermal conductivity ~ 2.5 W m^{-1} K^{-1}, *i.e.* about 10 times the value of neat pCBT, which is the highest value measured between all the nanocomposites prepared in this thesis. It is interesting to observe that adding 10 wt.% of RGO_1700 and 20 wt.% of GNP led to the same thermal conductivity value (~ 1.8 W m^{-1} K^{-1}), which can be also obtained in composites containing about 50 wt.% of graphite. Based on the measured thermal conductivity values,

nanocomposites prepared in this thesis can be regarded as materials for the production of heat sinks, considering that for these applications typically a minimum thermal conductivity of ~ 1 W m^{-1} K^{-1} is required.

- Dispersion of graphene related materials into polymers by melt mixing is challenging owing to the limited chemical affinity between the two phases. However, reasonable dispersion were demonstrated possible in this thesis by the pre-impregnation of the expanded structure of graphene-related materials with polymer or polymer precursors. Pre-impregnation was found mandatory for the preparation of high quality polymer nanocomposites, with limited differences in term of nanoparticle dispersion and thermal and electrical properties between solvent-assisted extrusion and in-situ polymerization. However, pre-impregnation of oligomers was found preferable both in terms of processing flexibility and sustainability.
- The proper control of processing parameters was demonstrated mandatory for the obtainment of high quality polymer nanocomposites, especially when low defective and high aspect ratio nanoflakes are used. This is related to a reduction of nanoparticle aspect ratio occurring during polymerization of CBT into pCBT, with a larger reduction when severer mixing conditions are used; in fact, nanocomposite prepared with the milder mixing condition resulted in 36% and two-order of magnitude thermal and electrical conductivity enhancement, respectively, respect to the nanocomposite prepared under the severer processing conditions, thus suggesting the need for gentle mixing to separate nanoflakes, but avoiding excessive fragmentation. However, the optimization carried out in this thesis is not complete, and many parameters (including nanoparticle quantities, screw profile, etc) have to be further studied to up-scale this process to an industrial level. Furthermore, careful optimization of processing parameters is required also to control the molecular weight of pCBT, considering that about 40% decrease, respect to neat pCBT was observed for the molecular weight of nanocomposites containing 5 wt.% GRM, directly affecting the mechanical properties of the nanocomposites.
- graphene-related materials were found to act as strong nucleating agent on both CBT and pCBT, with a general shift of crystallization peak to higher temperature. For cyclic oligomers splitting of the

crystallization process into multiple peaks suggests that the nucleation activity of GRM is exerted preferentially on higher molecular weight fraction in the CBT mixture. For pCBT, a shift of crystallization peak to higher temperatures was observed, dependently on nanoparticle defectiveness and aspect ratio. In fact, comparing nanocomposites, the lower and higher peak shift were observed for pristine and annealed rGO, respectively. A shift in between those of rGO and annealed rGO was observed for GNP. The crystallization peak shift was estimated ~ 11 and ~ 18 °C in pCBT + 10% RGO and RGO_1700, respectively, and such increase was never reported in literature for pCBT/GRM nanocomposites. None of the GRM was reported to affect the crystalline phase of pCBT, which appeared always in its α-form. Furthermore, less defective nanoflakes led to a strong orientation of polymer chains on the nanoflake surfaces with the formation of a highly thermally stable crystal population which melts at ~ 250 °C (*i.e.* ~ 25°C more than pCBT melting peak) and crystallizes at ~ 235 °C (*i.e.* ~ 45°C higher than the crystallization peak in pristine pCBT) and is related to thick α-form pCBT crystals. The formation of these crystals is interesting for a possible control of contact between nanoflakes through polymer crystallized on the nanoparticle surfaces, which may lead to a higher heat transfer between nanoflakes.

The results reported in this thesis demonstrate the viability of CBT polymerization during melt mixing with graphene related materials to produce thermally and electrically conductive polymers nanocomposites for possible industrial applications. However, further significant improvements are possible and hoped for the successful exploitation of these nanomaterial. In particular, further development in the synthesis of graphene-related materials with higher aspect ratio and lower defectiveness is still needed. In this regards, the substitution of the currently most popular process of oxidation and reduction with other more efficient and more sustainable processes would represent a significant step forward in the exploitation of graphene-related materials. Beside the quality of the nanoparticles, also processing methods may be significantly improved, by the optimization of processing parameters, the use of suitable compatibilizers etc, hopefully leading to improved percolation networks as well as higher molecular weight of the polymer obtained after ring opening polymerization. Furthermore, similar ring opening polymerization procedure could be adopted for the preparation of nanocomposites based on other matrices, *e.g.* poly (lactic acid).

References

[1] Z. Han, A. Fina, Thermal conductivity of carbon nanotubes and their polymer nanocomposites: a review, Progress in polymer science 36(7) (2011) 914-944.

[2] M. Vadivelu, C.R. Kumar, G.M. Joshi, Polymer composites for thermal management: a review, Composite Interfaces 23(9) (2016) 847-872.

[3] J.G. Drobny, Polymers for electricity and electronics: materials, properties, and applications, John Wiley & Sons2012.

[4] C. T'Joen, Y. Park, Q. Wang, A. Sommers, X. Han, A. Jacobi, A review on polymer heat exchangers for HVAC&R applications, international journal of refrigeration 32(5) (2009) 763-779.

[5] B. Adhikari, S. Majumdar, Polymers in sensor applications, Progress in polymer science 29(7) (2004) 699-766.

[6] E. Riande, R. Díaz-Calleja, Electrical properties of polymers, CRC Press2004.

[7] K. Hu, D.D. Kulkarni, I. Choi, V.V. Tsukruk, Graphene-polymer nanocomposites for structural and functional applications, Progress in Polymer Science 39(11) (2014) 1934-1972.

[8] B. Li, W.-H. Zhong, Review on polymer/graphite nanoplatelet nanocomposites, Journal of materials science 46(17) (2011) 5595-5614.

[9] W.E. Jones, J. Chiguma, E. Johnson, A. Pachamuthu, D. Santos, Electrically and thermally conducting nanocomposites for electronic applications, Materials 3(2) (2010) 1478-1496.

[10] N. Burger, A. Laachachi, M. Ferriol, M. Lutz, V. Toniazzo, D. Ruch, Review of thermal conductivity in composites: Mechanisms, parameters and theory, Progress in Polymer Science 61 (2016) 1-28.

[11] H. Chen, V.V. Ginzburg, J. Yang, Y. Yang, W. Liu, Y. Huang, L. Du, B. Chen, Thermal conductivity of polymer-based composites: Fundamentals and applications, Progress in Polymer Science 59 (2016) 41-85.

[12] W.M. Rohsenow, J.P. Hartnett, Y.I. Cho, Handbook of heat transfer, McGraw-Hill New York1998.

[13] T.Y. Kim, C.-H. Park, N. Marzari, The electronic thermal conductivity of graphene, Nano letters 16(4) (2016) 2439-2443.

[14] S. Yiğen, V. Tayari, J. Island, J. Porter, A. Champagne, Electronic thermal conductivity measurements in intrinsic graphene, Physical Review B 87(24) (2013) 241411.

[15] M. Pietralla, High thermal conductivity of polymers: Possibility or dream?, Journal of Computer-Aided Materials Design 3(1-3) (1996) 273-280.

[16] A.R.J. Hussain, A.A. Alahyari, S.A. Eastman, C. Thibaud-Erkey, S. Johnston, M.J. Sobkowicz, Review of polymers for heat exchanger applications: Factors concerning thermal conductivity, Applied Thermal Engineering 113 (2017) 1118-1127.

[17] C. Choy, Thermal conductivity of polymers, Polymer 18(10) (1977) 984-1004.

[18] B. Weidenfeller, M. Anhalt, S. Kirchberg, Thermal diffusivity and mechanical properties of polymer matrix composites, Journal of Applied Physics 112(9) (2012) 093513.

[19] D.E. Kline, Thermal conductivity studies of polymers, Journal of Polymer Science 50(154) (1961) 441-450.

[20] S. Shen, A. Henry, J. Tong, R. Zheng, G. Chen, Polyethylene nanofibres with very high thermal conductivities, Nature nanotechnology 5(4) (2010) 251-255.

[21] Y. Lu, J. Liu, X. Xie, D.G. Cahill, Thermal Conductivity in the Radial Direction of Deformed Polymer Fibers, ACS Macro Letters 5(6) (2016) 646-650.

[22] T. Zhang, X. Wu, T. Luo, Polymer nanofibers with outstanding thermal conductivity and thermal stability: Fundamental linkage between molecular characteristics and macroscopic thermal properties, The Journal of Physical Chemistry C 118(36) (2014) 21148-21159.

[23] W. Dos Santos, J. De Sousa, R. Gregorio, Thermal conductivity behaviour of polymers around glass transition and crystalline melting temperatures, Polymer Testing 32(5) (2013) 987-994.

[24] E. Pop, V. Varshney, A.K. Roy, Thermal properties of graphene: Fundamentals and applications, MRS bulletin 37(12) (2012) 1273-1281.

[25] V.D. Punetha, S. Rana, H.J. Yoo, A. Chaurasia, J.T. McLeskey, M.S. Ramasamy, N.G. Sahoo, J.W. Cho, Functionalization of carbon nanomaterials for advanced polymer nanocomposites: A comparison study between CNT and graphene, Progress in Polymer Science (2016).

[26] M. Namasivayam, J. Shapter, Factors affecting carbon nanotube fillers towards enhancement of thermal conductivity in polymer nanocomposites: A review, Journal of Composite Materials (2017) 0021998317692398.

[27] A. Bianco, H.-M. Cheng, T. Enoki, Y. Gogotsi, R.H. Hurt, N. Koratkar, T. Kyotani, M. Monthioux, C.R. Park, J.M. Tascon, All in the graphene family–a recommended nomenclature for two-dimensional carbon materials, Carbon 65 (2013) 1-6.

[28] K.S. Novoselov, A.K. Geim, S. Morozov, D. Jiang, Y. Zhang, S.a. Dubonos, I. Grigorieva, A. Firsov, Electric field effect in atomically thin carbon films, science 306(5696) (2004) 666-669.

[29] A.K. Geim, Graphene: status and prospects, science 324(5934) (2009) 1530-1534.

[30] A.A. Balandin, S. Ghosh, W. Bao, I. Calizo, D. Teweldebrhan, F. Miao, C.N. Lau, Superior thermal conductivity of single-layer graphene, Nano letters 8(3) (2008) 902-907.

[31] C. Lee, X. Wei, J.W. Kysar, J. Hone, Measurement of the elastic properties and intrinsic strength of monolayer graphene, science 321(5887) (2008) 385-388.

[32] D. Chung, Materials for thermal conduction, Applied thermal engineering 21(16) (2001) 1593-1605.

[33] A.A. Balandin, Thermal properties of graphene and nanostructured carbon materials, Nature materials 10(8) (2011) 569-81.

[34] X. Mu, Z. Song, Y. Wang, Z. Xu, D.B. Go, T. Luo, Thermal transport in oxidized polycrystalline graphene, Carbon 108 (2016) 318-326.

[35] M. Tortello, S. Colonna, M. Bernal, J. Gomez, M. Pavese, C. Novara, F. Giorgis, M. Maggio, G. Guerra, G. Saracco, Effect of thermal annealing on the heat transfer properties of reduced graphite oxide flakes: A nanoscale characterization via scanning thermal microscopy, Carbon 109 (2016) 390-401.

[36] J.H. Seol, I. Jo, A.L. Moore, L. Lindsay, Z.H. Aitken, M.T. Pettes, X. Li, Z. Yao, R. Huang, D. Broido, Two-dimensional phonon transport in supported graphene, Science 328(5975) (2010) 213-216.

[37] S. Chen, Q. Wu, C. Mishra, J. Kang, H. Zhang, K. Cho, W. Cai, A.A. Balandin, R.S. Ruoff, Thermal conductivity of isotopically modified graphene, Nature materials 11(3) (2012) 203-207.

[38] S. Ghosh, I. Calizo, D. Teweldebrhan, E.P. Pokatilov, D.L. Nika, A.A. Balandin, W. Bao, F. Miao, C.N. Lau, Extremely high thermal conductivity of graphene: Prospects for thermal management applications in nanoelectronic circuits, Applied Physics Letters 92(15) (2008) 151911.

[39] D. Nika, E. Pokatilov, A. Askerov, A. Balandin, Phonon thermal conduction in graphene: Role of Umklapp and edge roughness scattering, Physical Review B 79(15) (2009) 155413.

[40] T. Feng, X. Ruan, Z. Ye, B. Cao, Spectral phonon mean free path and thermal conductivity accumulation in defected graphene: The effects of defect type and concentration, Physical Review B 91(22) (2015) 224301.

[41] B. Mortazavi, S. Ahzi, Thermal conductivity and tensile response of defective graphene: A molecular dynamics study, Carbon 63 (2013) 460-470.

[42] B. Mortazavi, S. Ahzi, Molecular dynamics study on the thermal conductivity and mechanical properties of boron doped graphene, Solid State Communications 152(15) (2012) 1503-1507.

[43] B. Mortazavi, A. Rajabpour, S. Ahzi, Y. Rémond, S. Mehdi Vaez Allaei, Nitrogen doping and curvature effects on thermal conductivity of graphene: A non-equilibrium molecular dynamics study, Solid State Communications 152(4) (2012) 261-264.

[44] H. Malekpour, P. Ramnani, S. Srinivasan, G. Balasubramanian, D.L. Nika, A. Mulchandani, R.K. Lake, A.A. Balandin, Thermal conductivity of graphene with defects induced by electron beam irradiation, Nanoscale 8(30) (2016) 14608-14616.

[45] E. Rollings, G.-H. Gweon, S. Zhou, B. Mun, J. McChesney, B. Hussain, A. Fedorov, P. First, W. De Heer, A. Lanzara, Synthesis and characterization of atomically thin graphite films on a silicon carbide substrate, Journal of Physics and Chemistry of Solids 67(9) (2006) 2172-2177.

[46] X. Li, W. Cai, J. An, S. Kim, J. Nah, D. Yang, R. Piner, A. Velamakanni, I. Jung, E. Tutuc, Large-area synthesis of high-quality and uniform graphene films on copper foils, Science 324(5932) (2009) 1312-1314.

[47] S.J. Chae, F. Güneş, K.K. Kim, E.S. Kim, G.H. Han, S.M. Kim, H.J. Shin, S.M. Yoon, J.Y. Choi, M.H. Park, Synthesis of large-area graphene layers on poly-nickel substrate by chemical vapor deposition: wrinkle formation, Advanced Materials 21(22) (2009) 2328-2333.

[48] M. Mecklenburg, A. Schuchardt, Y.K. Mishra, S. Kaps, R. Adelung, A. Lotnyk, L. Kienle, K. Schulte, Aerographite: ultra lightweight, flexible nanowall,

carbon microtube material with outstanding mechanical performance, Advanced Materials 24(26) (2012) 3486-3490.

[49] U. Khan, A. O'Neill, M. Lotya, S. De, J.N. Coleman, High-concentration solvent exfoliation of graphene, Small 6(7) (2010) 864-71.

[50] Y. Hernandez, V. Nicolosi, M. Lotya, F.M. Blighe, Z. Sun, S. De, I. McGovern, B. Holland, M. Byrne, Y.K. Gun'Ko, High-yield production of graphene by liquid-phase exfoliation of graphite, Nature nanotechnology 3(9) (2008) 563-568.

[51] S. Colonna, O. Monticelli, J. Gomez, C. Novara, G. Saracco, A. Fina, Effect of morphology and defectiveness of graphene-related materials on the electrical and thermal conductivity of their polymer nanocomposites, Polymer 102 (2016) 292-300.

[52] S. Stankovich, D.A. Dikin, R.D. Piner, K.A. Kohlhaas, A. Kleinhammes, Y. Jia, Y. Wu, S.T. Nguyen, R.S. Ruoff, Synthesis of graphene-based nanosheets via chemical reduction of exfoliated graphite oxide, Carbon 45(7) (2007) 1558-1565.

[53] Z.-S. Wu, W. Ren, L. Gao, B. Liu, C. Jiang, H.-M. Cheng, Synthesis of high-quality graphene with a pre-determined number of layers, Carbon 47(2) (2009) 493-499.

[54] H.C. Schniepp, J.-L. Li, M.J. McAllister, H. Sai, M. Herrera-Alonso, D.H. Adamson, R.K. Prud'homme, R. Car, D.A. Saville, I.A. Aksay, Functionalized single graphene sheets derived from splitting graphite oxide, The Journal of Physical Chemistry B 110(17) (2006) 8535-8539.

[55] M. Lotya, Y. Hernandez, P.J. King, R.J. Smith, V. Nicolosi, L.S. Karlsson, F.M. Blighe, S. De, Z. Wang, I. McGovern, Liquid phase production of graphene by exfoliation of graphite in surfactant/water solutions, Journal of the American Chemical Society 131(10) (2009) 3611-3620.

[56] N. Liu, F. Luo, H. Wu, Y. Liu, C. Zhang, J. Chen, One-step ionic-liquid-assisted electrochemical synthesis of ionic-liquid-functionalized graphene sheets directly from graphite, Advanced Functional Materials 18(10) (2008) 1518-1525.

[57] K.S. Novoselov, V. Fal, L. Colombo, P. Gellert, M. Schwab, K. Kim, A roadmap for graphene, Nature 490(7419) (2012) 192-200.

[58] K. Novoselov, D. Jiang, F. Schedin, T. Booth, V. Khotkevich, S. Morozov, A. Geim, Two-dimensional atomic crystals, Proceedings of the National Academy of Sciences of the United States of America 102(30) (2005) 10451-10453.

[59] R.M. Jacobberger, R. Machhi, J. Wroblewski, B. Taylor, A.L. Gillian-Daniel, M.S. Arnold, Simple graphene synthesis via chemical vapor deposition, Journal of Chemical Education 92(11) (2015) 1903-1907.

[60] D. Su, M. Ren, X.a. Li, W. Huang, Synthesis of graphene by chemical vapor deposition: effect of growth conditions, Journal of nanoscience and nanotechnology 13(10) (2013) 6471-6484.

[61] N.-E. Weber, A. Binder, M. Kettner, S. Hirth, R.T. Weitz, Ž. Tomović, Metal-free synthesis of nanocrystalline graphene on insulating substrates by carbon dioxide-assisted chemical vapor deposition, Carbon 112 (2017) 201-207.

[62] W.S. Hummers Jr, R.E. Offeman, Preparation of graphitic oxide, Journal of the American Chemical Society 80(6) (1958) 1339-1339.

[63] U. Hofmann, W. Rüdorff, The formation of salts from graphite by strong acids, Transactions of the Faraday Society 34 (1938) 1017-1021.

[64] S. Lin, L. Dong, J. Zhang, H. Lu, Room-Temperature Intercalation and~ 1000-Fold Chemical Expansion for Scalable Preparation of High-Quality Graphene, Chemistry of Materials 28(7) (2016) 2138-2146.

[65] D.R. Dreyer, S. Park, C.W. Bielawski, R.S. Ruoff, The chemistry of graphene oxide, Chemical Society reviews 39(1) (2010) 228-40.

[66] W. Gao, L.B. Alemany, L. Ci, P.M. Ajayan, New insights into the structure and reduction of graphite oxide, Nat Chem 1(5) (2009) 403-8.

[67] D. Yang, A. Velamakanni, G. Bozoklu, S. Park, M. Stoller, R.D. Piner, S. Stankovich, I. Jung, D.A. Field, C.A. Ventrice, R.S. Ruoff, Chemical analysis of graphene oxide films after heat and chemical treatments by X-ray photoelectron and Micro-Raman spectroscopy, Carbon 47(1) (2009) 145-152.

[68] R. Rozada, J.I. Paredes, M.J. Lopez, S. Villar-Rodil, I. Cabria, J.A. Alonso, A. Martinez-Alonso, J.M. Tascon, From graphene oxide to pristine graphene: revealing the inner workings of the full structural restoration, Nanoscale 7(6) (2015) 2374-90.

[69] R. Rozada, J.I. Paredes, S. Villar-Rodil, A. Martínez-Alonso, J.M. Tascón, Towards full repair of defects in reduced graphene oxide films by two-step graphitization, Nano Research 6(3) (2013) 216-233.

[70] K. Parvez, Z.-S. Wu, R. Li, X. Liu, R. Graf, X. Feng, K. Müllen, Exfoliation of graphite into graphene in aqueous solutions of inorganic salts, Journal of the American Chemical Society 136(16) (2014) 6083-6091.

[71] K. Parvez, R. Li, S.R. Puniredd, Y. Hernandez, F. Hinkel, S. Wang, X. Feng, K. Müllen, Electrochemically exfoliated graphene as solution-processable, highly conductive electrodes for organic electronics, ACS nano 7(4) (2013) 3598-3606.

[72] S. Yang, S. Bruller, Z.S. Wu, Z. Liu, K. Parvez, R. Dong, F. Richard, P. Samori, X. Feng, K. Mullen, Organic Radical-Assisted Electrochemical Exfoliation for the Scalable Production of High-Quality Graphene, Journal of the American Chemical Society 137(43) (2015) 13927-32.

[73] J. Munuera, J. Paredes, S. Villar-Rodil, M. Ayán-Varela, A. Martínez-Alonso, J. Tascon, Electrolytic exfoliation of graphite in water with multifunctional electrolytes: en route towards high quality, oxide-free graphene flakes, Nanoscale 8(5) (2016) 2982-2998.

[74] J. Wang, K.K. Manga, Q. Bao, K.P. Loh, High-yield synthesis of few-layer graphene flakes through electrochemical expansion of graphite in propylene carbonate electrolyte, Journal of the American Chemical Society 133(23) (2011) 8888-8891.

[75] Z.Y. Xia, S. Pezzini, E. Treossi, G. Giambastiani, F. Corticelli, V. Morandi, A. Zanelli, V. Bellani, V. Palermo, The Exfoliation of Graphene in Liquids by Electrochemical, Chemical, and Sonication-Assisted Techniques: A Nanoscale Study, Advanced Functional Materials (2013) n/a-n/a.

[76] M. Zhang, Y. Li, Z. Su, G. Wei, Recent advances in the synthesis and applications of graphene–polymer nanocomposites, Polymer Chemistry 6(34) (2015) 6107-6124.

[77] K.M. Shahil, A.A. Balandin, Graphene-multilayer graphene nanocomposites as highly efficient thermal interface materials, Nano letters 12(2) (2012) 861-7.

[78] A.P. Kumar, D. Depan, N.S. Tomer, R.P. Singh, Nanoscale particles for polymer degradation and stabilization—trends and future perspectives, Progress in Polymer Science 34(6) (2009) 479-515.

[79] P.-C. Ma, N.A. Siddiqui, G. Marom, J.-K. Kim, Dispersion and functionalization of carbon nanotubes for polymer-based nanocomposites: A review, Composites Part A: Applied Science and Manufacturing 41(10) (2010) 1345-1367.

[80] T. Kuilla, S. Bhadra, D. Yao, N.H. Kim, S. Bose, J.H. Lee, Recent advances in graphene based polymer composites, Progress in Polymer Science 35(11) (2010) 1350-1375.

[81] M.P. Weir, D.W. Johnson, S.C. Boothroyd, R.C. Savage, R.L. Thompson, S.R. Parnell, A.J. Parnell, S.M. King, S.E. Rogers, K.S. Coleman, Extrinsic Wrinkling and Single Exfoliated Sheets of Graphene Oxide in Polymer Composites, Chem. Mater 28(6) (2016) 1698-1704.

[82] M. Ma, Z. Zhu, B. Wu, S. Chen, Y. Shi, X. Wang, Preparation of highly conductive composites with segregated structure based on polyamide-6 and reduced graphene oxide, Materials Letters 190 (2017) 71-74.

[83] C. Vallés, F. Beckert, L. Burk, R. Mülhaupt, R.J. Young, I.A. Kinloch, Effect of the C/O ratio in graphene oxide materials on the reinforcement of epoxy-based nanocomposites, Journal of Polymer Science Part B: Polymer Physics 54(2) (2016) 281-291.

[84] X. Qi, Y. Guo, Y. Wei, P. Dong, Q. Fu, Multishape and Temperature Memory Effects by Strong Physical Confinement in Poly (propylene carbonate)/Graphene Oxide Nanocomposites, The Journal of Physical Chemistry B 120(42) (2016) 11064-11073.

[85] K. Liu, E. Andablo-Reyes, N. Patil, D.H. Merino, S. Ronca, S. Rastogi, Influence of reduced graphene oxide on the rheological response and chain orientation on shear deformation of high density polyethylene, Polymer 87 (2016) 8-16.

[86] P. Kumar, S. Yu, F. Shahzad, S.M. Hong, Y.-H. Kim, C.M. Koo, Ultrahigh electrically and thermally conductive self-aligned graphene/polymer composites using large-area reduced graphene oxides, Carbon 101 (2016) 120-128.

[87] C.S. Boland, U. Khan, G. Ryan, S. Barwich, R. Charifou, A. Harvey, C. Backes, Z. Li, M.S. Ferreira, M.E. Möbius, Sensitive electromechanical sensors using viscoelastic graphene-polymer nanocomposites, Science 354(6317) (2016) 1257-1260.

[88] Y. Li, J. Zhu, S. Wei, J. Ryu, L. Sun, Z. Guo, Poly (propylene)/graphene nanoplatelet nanocomposites: melt rheological behavior and thermal, electrical, and electronic properties, Macromolecular Chemistry and Physics 212(18) (2011) 1951-1959.

[89] N. Song, J. Yang, P. Ding, S. Tang, L. Shi, Effect of polymer modifier chain length on thermal conductive property of polyamide 6/graphene nanocomposites, Composites Part A: Applied Science and Manufacturing 73 (2015) 232-241.

[90] J. Kim, J. Kim, S. Song, S. Zhang, J. Cha, K. Kim, H. Yoon, Y. Jung, K.-W. Paik, S. Jeon, Strength dependence of epoxy composites on the average filler size of non-oxidized graphene flake, Carbon 113 (2017) 379-386.

[91] N. Maity, A. Mandal, A.K. Nandi, Synergistic interfacial effect of polymer stabilized graphene via non-covalent functionalization in poly (vinylidene fluoride) matrix yielding superior mechanical and electronic properties, Polymer 88 (2016) 79-93.

[92] J. Luo, F. Zhao, X. Fei, X. Liu, J. Liu, Mussel inspired preparation of polymer grafted graphene as a bridge between covalent and noncovalent methods, Chemical Engineering Journal 293 (2016) 171-181.

[93] Y. Gao, O.T. Picot, E. Bilotti, T. Peijs, Influence of filler size on the properties of poly (lactic acid)(PLA)/graphene nanoplatelet (GNP) nanocomposites, European Polymer Journal 86 (2017) 117-131.

[94] C. Vallés, I.A. Kinloch, R.J. Young, N.R. Wilson, J.P. Rourke, Graphene oxide and base-washed graphene oxide as reinforcements in PMMA nanocomposites, Composites Science and Technology 88 (2013) 158-164.

[95] K.F. Ratzsch, V. Cecen, F. Tölle, K.A. Wartig, R. Thomann, R. Mülhaupt, C. Friedrich, Rheology, Electrical Properties, and Percolation of TRGO-Filled EVA-Copolymers, Macromolecular Materials and Engineering 299(9) (2014) 1134-1144.

[96] S. Dul, L. Fambri, A. Pegoretti, Fused deposition modelling with ABS–graphene nanocomposites, Composites Part A: Applied Science and Manufacturing 85 (2016) 181-191.

[97] Y. Han, T. Wang, X. Gao, T. Li, Q. Zhang, Preparation of thermally reduced graphene oxide and the influence of its reduction temperature on the thermal, mechanical, flame retardant performances of PS nanocomposites, Composites Part A: Applied Science and Manufacturing 84 (2016) 336-343.

[98] M. El Achaby, F.-E. Arrakhiz, S. Vaudreuil, A. el Kacem Qaiss, M. Bousmina, O. Fassi-Fehri, Mechanical, thermal, and rheological properties of graphene-based polypropylene nanocomposites prepared by melt mixing, Polymer Composites 33(5) (2012) 733-744.

[99] J.R. Potts, D.R. Dreyer, C.W. Bielawski, R.S. Ruoff, Graphene-based polymer nanocomposites, Polymer 52(1) (2011) 5-25.

[100] R. Verdejo, M.M. Bernal, L.J. Romasanta, M.A. Lopez-Manchado, Graphene filled polymer nanocomposites, Journal of Materials Chemistry 21(10) (2011) 3301-3310.

[101] A.S. Nia, W.H. Binder, Graphene as initiator/catalyst in polymerization chemistry, Progress in Polymer Science (2016).

[102] Z. Xu, C. Gao, In situ polymerization approach to graphene-reinforced nylon-6 composites, Macromolecules 43(16) (2010) 6716-6723.

[103] J.-H. Yang, S.-H. Lin, Y.-D. Lee, Preparation and characterization of poly (l-lactide)–graphene composites using the in situ ring-opening polymerization of PLLA with graphene as the initiator, Journal of Materials Chemistry 22(21) (2012) 10805-10815.

[104] P. Wang, J. Zhang, L. Dong, C. Sun, X. Zhao, Y. Ruan, H. Lu, Interlayer Polymerization in Chemically Expanded Graphite for Preparation of Highly Conductive, Mechanically Strong Polymer Composites, Chemistry of Materials (2017).

[105] Y.J. Noh, H.I. Joh, J. Yu, S.H. Hwang, S. Lee, C.H. Lee, S.Y. Kim, J.R. Youn, Ultra-high dispersion of graphene in polymer composite via solvent free fabrication and functionalization, Scientific reports 5 (2015) 9141.

[106] P. Liu, Z. Yao, L. Li, J. Zhou, In situ Synthesis and mechanical, thermal properties of polyimide nanocomposite film by addition of functionalized graphene oxide, Polymer Composites (2014).

[107] R. Shamsi, M. Koosha, M. Mahyari, Improving the mechanical, thermal and electrical properties of polyurethane-graphene oxide nanocomposites synthesized by in-situ polymerization of ester-based polyol with hexamethylene diisocyanate, Journal of Polymer Research 23(12) (2016) 262.

[108] H.O. Pierson, Handbook of carbon, graphite, diamonds and fullerenes: processing, properties and applications, William Andrew2012.

[109] S. Chandrasekaran, C. Seidel, K. Schulte, Preparation and characterization of graphite nano-platelet (GNP)/epoxy nano-composite: Mechanical, electrical and thermal properties, European Polymer Journal 49(12) (2013) 3878-3888.

[110] Y. Li, H. Zhang, H. Porwal, Z. Huang, E. Bilotti, T. Peijs, Mechanical, electrical and thermal properties of in-situ exfoliated graphene/epoxy nanocomposites, Composites Part A: Applied Science and Manufacturing 95 (2017) 229-236.

[111] C. Heo, J.-H. Chang, Polyimide nanocomposites based on functionalized graphene sheets: Morphologies, thermal properties, and electrical and thermal conductivities, Solid State Sciences 24 (2013) 6-14.

[112] Z. Tang, H. Kang, Z. Shen, B. Guo, L. Zhang, D. Jia, Grafting of polyester onto graphene for electrically and thermally conductive composites, Macromolecules 45(8) (2012) 3444-3451.

[113] J. Canales, M.E. Muñoz, M. Fernández, A. Santamaría, Rheology, electrical conductivity and crystallinity of a polyurethane/graphene composite: Implications for its use as a hot-melt adhesive, Composites Part A: Applied Science and Manufacturing 84 (2016) 9-16.

[114] Y. Zhang, Y. Wang, C.M. Wang, Y. Gu, Thermal Conductivity of Graphene and Its Polymer Nanocomposites: A Review, Advanced Computational Nanomechanics (2015) 1.

[115] K.M. Shahil, A.A. Balandin, Graphene–multilayer graphene nanocomposites as highly efficient thermal interface materials, Nano letters 12(2) (2012) 861-867.

[116] C.-C. Teng, C.-C.M. Ma, C.-H. Lu, S.-Y. Yang, S.-H. Lee, M.-C. Hsiao, M.-Y. Yen, K.-C. Chiou, T.-M. Lee, Thermal conductivity and structure of non-covalent functionalized graphene/epoxy composites, Carbon 49(15) (2011) 5107-5116.

[117] P. Ding, S. Su, N. Song, S. Tang, Y. Liu, L. Shi, Highly thermal conductive composites with polyamide-6 covalently-grafted graphene by an in situ polymerization and thermal reduction process, Carbon 66 (2014) 576-584.

[118] Y. Hwang, M. Kim, J. Kim, Improvement of the mechanical properties and thermal conductivity of poly (ether-ether-ketone) with the addition of graphene

oxide-carbon nanotube hybrid fillers, Composites Part A: Applied Science and Manufacturing 55 (2013) 195-202.

[119] H. Wu, L.T. Drzal, High thermally conductive graphite nanoplatelet/polyetherimide composite by precoating: Effect of percolation and particle size, Polymer Composites 34(12) (2013) 2148-2153.

[120] X. Xiong, J. Wang, H. Jia, E. Fang, L. Ding, Structure, thermal conductivity, and thermal stability of bromobutyl rubber nanocomposites with ionic liquid modified graphene oxide, Polymer degradation and stability 98(11) (2013) 2208-2214.

[121] S. Araby, I. Zaman, Q. Meng, N. Kawashima, A. Michelmore, H.C. Kuan, P. Majewski, J. Ma, L. Zhang, Melt compounding with graphene to develop functional, high-performance elastomers, Nanotechnology 24(16) (2013) 165601.

[122] K. Chu, W.-s. Li, H. Dong, Role of graphene waviness on the thermal conductivity of graphene composites, Applied Physics A 111(1) (2013) 221-225.

[123] C. Min, D. Yu, J. Cao, G. Wang, L. Feng, A graphite nanoplatelet/epoxy composite with high dielectric constant and high thermal conductivity, Carbon 55 (2013) 116-125.

[124] S.H. Song, K.H. Park, B.H. Kim, Y.W. Choi, G.H. Jun, D.J. Lee, B.S. Kong, K.W. Paik, S. Jeon, Enhanced Thermal Conductivity of Epoxy–Graphene Composites by Using Non-Oxidized Graphene Flakes with Non-Covalent Functionalization, Advanced Materials 25(5) (2013) 732-737.

[125] D.K. Smith, M.L. Pantoya, Effect of nanofiller shape on effective thermal conductivity of fluoropolymer composites, Composites Science and Technology 118 (2015) 251-256.

[126] M. Shtein, R. Nadiv, M. Buzaglo, K. Kahil, O. Regev, Thermally Conductive Graphene-Polymer Composites: Size, Percolation, and Synergy Effects, Chemistry of Materials 27(6) (2015) 2100-2106.

[127] P. Kapitza, The study of heat transfer in helium II, J. Phys.(USSR) 4(1-6) (1941) 181-210.

[128] M. Wang, N. Hu, L. Zhou, C. Yan, Enhanced interfacial thermal transport across graphene–polymer interfaces by grafting polymer chains, Carbon 85 (2015) 414-421.

[129] Z. Zabihi, H. Araghi, Effect of functional groups on thermal conductivity of graphene/paraffin nanocomposite, Physics Letters A 380(45) (2016) 3828-3831.

[130] D. Konatham, A. Striolo, Thermal boundary resistance at the graphene-oil interface, Applied Physics Letters 95(16) (2009) 163105.

[131] X. Shen, Z. Wang, Y. Wu, X. Liu, J.-K. Kim, Effect of functionalization on thermal conductivities of graphene/epoxy composites, Carbon 108 (2016) 412-422.

[132] S. Lin, M.J. Buehler, The effect of non-covalent functionalization on the thermal conductance of graphene/organic interfaces, Nanotechnology 24(16) (2013) 165702.

[133] S. Zhao, H. Chang, S. Chen, J. Cui, Y. Yan, High-performance and multifunctional epoxy composites filled with epoxide-functionalized graphene, European Polymer Journal 84 (2016) 300-312.

[134] Z. Li, D. Wang, M. Zhang, L. Zhao, Enhancement of the thermal conductivity of polymer composites with Ag–graphene hybrids as fillers, physica status solidi (a) 211(9) (2014) 2142-2149.

[135] S. Ganguli, A.K. Roy, D.P. Anderson, Improved thermal conductivity for chemically functionalized exfoliated graphite/epoxy composites, Carbon 46(5) (2008) 806-817.

[136] J. Gu, X. Yang, Z. Lv, N. Li, C. Liang, Q. Zhang, Functionalized graphite nanoplatelets/epoxy resin nanocomposites with high thermal conductivity, International Journal of Heat and Mass Transfer 92 (2016) 15-22.

[137] J. Renteria, S. Legedza, R. Salgado, M.P. Balandin, S. Ramirez, M. Saadah, F. Kargar, A.A. Balandin, Magnetically-functionalized self-aligning graphene fillers for high-efficiency thermal management applications, Materials & Design 88 (2015) 214-221.

[138] G. Lian, C.-C. Tuan, L. Li, S. Jiao, Q. Wang, K.-S. Moon, D. Cui, C.-P. Wong, Vertically Aligned and Interconnected Graphene Networks for High Thermal Conductivity of Epoxy Composites with Ultralow Loading, Chemistry of Materials 28(17) (2016) 6096-6104.

[139] O. Eksik, S.F. Bartolucci, T. Gupta, H. Fard, T. Borca-Tasciuc, N. Koratkar, A novel approach to enhance the thermal conductivity of epoxy nanocomposites using graphene core–shell additives, Carbon 101 (2016) 239-244.

[140] X. Zhang, Q. Shen, X. Zhang, H. Pan, Y. Lu, Graphene oxide-filled multilayer coating to improve flame-retardant and smoke suppression properties of flexible polyurethane foam, Journal of Materials Science 51(23) (2016) 10361-10374.

[141] H. Ha, J. Park, S. Ando, C.B. Kim, K. Nagai, B.D. Freeman, C.J. Ellison, Gas permeation and selectivity of poly (dimethylsiloxane)/graphene oxide composite elastomer membranes, Journal of Membrane Science 518 (2016) 131-140.

[142] P.-G. Ren, X.-H. Liu, F. Ren, G.-J. Zhong, X. Ji, L. Xu, Biodegradable graphene oxide nanosheets/poly-(butylene adipate-co-terephthalate)

nanocomposite film with enhanced gas and water vapor barrier properties, Polymer Testing 58 (2017) 173-180.

[143] X. Sheng, W. Cai, L. Zhong, D. Xie, X. Zhang, Synthesis of Functionalized Graphene/Polyaniline Nanocomposites with Effective Synergistic Reinforcement on Anticorrosion, Industrial & Engineering Chemistry Research 55(31) (2016) 8576-8585.

[144] S. Colonna, A. Fina, Z. Han, G. Saracco, Graphene nanoplatelets for thermally conductive polymer nanocomposites, Graphene Conference, Toulouse, 2014.

[145] D. Zhang, Y. Lin, G. Wu, Polylactide-based nanocomposites with stereocomplex networks enhanced by GO-g-PDLA, Composites Science and Technology 138 (2017) 57-67.

[146] A.R. Tripathy, A. Elmoumni, H.H. Winter, W.J. MacKnight, Effects of catalyst and polymerization temperature on the in-situ polymerization of cyclic poly (butylene terephthalate) oligomers for composite applications, Macromolecules 38(3) (2005) 709-715.

[147] P. Fabbri, E. Bassoli, S.B. Bon, L. Valentini, Preparation and characterization of poly (butylene terephthalate)/graphene composites by in-situ polymerization of cyclic butylene terephthalate, Polymer 53(4) (2012) 897-902.

[148] N. Nomura, R. Ishii, M. Akakura, K. Aoi, Stereoselective ring-opening polymerization of racemic lactide using aluminum-achiral ligand complexes: Exploration of a chain-end control mechanism, Journal of the American Chemical Society 124(21) (2002) 5938-5939.

[149] A.C. Ferrari, D.M. Basko, Raman spectroscopy as a versatile tool for studying the properties of graphene, Nature nanotechnology 8(4) (2013) 235-46.

[150] A.C. Ferrari, J. Robertson, Interpretation of Raman spectra of disordered and amorphous carbon, Physical review B 61(20) (2000) 14095.

[151] A. Eckmann, A. Felten, I. Verzhbitskiy, R. Davey, C. Casiraghi, Raman study on defective graphene: effect of the excitation energy, type, and amount of defects, Physical Review B 88(3) (2013) 035426.

[152] M.S. Dresselhaus, A. Jorio, A.G. Souza Filho, R. Saito, Defect characterization in graphene and carbon nanotubes using Raman spectroscopy, Philosophical transactions. Series A, Mathematical, physical, and engineering sciences 368(1932) (2010) 5355-77.

[153] L.M. Malard, M.A. Pimenta, G. Dresselhaus, M.S. Dresselhaus, Raman spectroscopy in graphene, Physics Reports 473(5-6) (2009) 51-87.

[154] M.S. Seehra, V. Narang, U.K. Geddam, A.B. Stefaniak, Correlation between X-ray diffraction and Raman spectra of 16 commercial graphene–based materials and their resulting classification, Carbon 111 (2017) 380-385.

[155] A. Ganguly, S. Sharma, P. Papakonstantinou, J. Hamilton, Probing the thermal deoxygenation of graphene oxide using high-resolution in situ X-ray-based spectroscopies, The Journal of Physical Chemistry C 115(34) (2011) 17009-17019.

[156] I.Y. Jeon, Y.R. Shin, G.J. Sohn, H.J. Choi, S.Y. Bae, J. Mahmood, S.M. Jung, J.M. Seo, M.J. Kim, D. Wook Chang, L. Dai, J.B. Baek, Edge-carboxylated graphene nanosheets via ball milling, Proc Natl Acad Sci U S A 109(15) (2012) 5588-93.

[157] M. Shtein, I. Pri-Bar, M. Varenik, O. Regev, Characterization of graphene-nanoplatelets structure via thermogravimetry, Analytical chemistry 87(8) (2015) 4076-4080.

[158] K.-H. Illers, Heat of fusion and specific volume of poly (ethylene terephthalate) and poly (butylene terephthalate, Colloid and Polymer Science 258(2) (1980) 117-124.

[159] A.T. Lorenzo, M.L. Arnal, J. Albuerne, A.J. Müller, DSC isothermal polymer crystallization kinetics measurements and the use of the Avrami equation to fit the data: guidelines to avoid common problems, Polymer testing 26(2) (2007) 222-231.

[160] B. Fillon, J. Wittmann, B. Lotz, A. Thierry, Self-nucleation and recrystallization of isotactic polypropylene (α phase) investigated by differential scanning calorimetry, Journal of Polymer Science Part B: Polymer Physics 31(10) (1993) 1383-1393.

[161] A.J. Müller, M.L. Arnal, Thermal fractionation of polymers, Progress in polymer science 30(5) (2005) 559-603.

[162] A. Müller, R. Michell, R. Pérez, A. Lorenzo, Successive self-nucleation and annealing (SSA): Correct design of thermal protocol and applications, European Polymer Journal 65 (2015) 132-154.

[163] D. Blundell, A. Keller, A. Kovacs, A new self-nucleation phenomenon and its application to the growing of polymer crystals from solution, Journal of Polymer Science Part B: Polymer Letters 4(7) (1966) 481-486.

[164] W. Borman, Molecular weight–viscosity relationships for poly (1, 4-butylene terephthalate), Journal of Applied Polymer Science 22(8) (1978) 2119-2126.

[165] J.E. Mark, Polymer data handbook, Oxford university press2009.

[166] J.D. Renteria, S. Ramirez, H. Malekpour, B. Alonso, A. Centeno, A. Zurutuza, A.I. Cocemasov, D.L. Nika, A.A. Balandin, Strongly anisotropic thermal conductivity of free-standing reduced graphene oxide films annealed at high temperature, Advanced Functional Materials 25(29) (2015) 4664-4672.

[167] M. Jin, T.H. Kim, S.C. Lim, D.L. Duong, H.J. Shin, Y.W. Jo, H.K. Jeong, J. Chang, S. Xie, Y.H. Lee, Facile physical route to highly crystalline graphene, Advanced Functional Materials 21(18) (2011) 3496-3501.

[168] A.C. Ferrari, Raman spectroscopy of graphene and graphite: Disorder, electron–phonon coupling, doping and nonadiabatic effects, Solid State Communications 143(1-2) (2007) 47-57.

[169] A. Bagri, C. Mattevi, M. Acik, Y.J. Chabal, M. Chhowalla, V.B. Shenoy, Structural evolution during the reduction of chemically derived graphene oxide, Nature chemistry 2(7) (2010) 581-587.

[170] T. Sun, S. Fabris, S. Baroni, Surface precursors and reaction mechanisms for the thermal reduction of graphene basal surfaces oxidized by atomic oxygen, The Journal of Physical Chemistry C 115(11) (2011) 4730-4737.

[171] I. Roppolo, A. Chiappone, K. Bejtka, E. Celasco, A. Chiodoni, F. Giorgis, M. Sangermano, S. Porro, A powerful tool for graphene functionalization: Benzophenone mediated UV-grafting, Carbon 77 (2014) 226-235.

[172] A. Ferrari, J. Meyer, V. Scardaci, C. Casiraghi, M. Lazzeri, F. Mauri, S. Piscanec, D. Jiang, K. Novoselov, S. Roth, Raman spectrum of graphene and graphene layers, Physical review letters 97(18) (2006) 187401.

[173] F. Tuinstra, J.L. Koenig, Raman spectrum of graphite, The Journal of chemical physics 53(3) (1970) 1126-1130.

[174] J. Loomis, X. Fan, F. Khosravi, P. Xu, M. Fletcher, R.W. Cohn, B. Panchapakesan, Graphene/elastomer composite-based photo-thermal nanopositioners, Scientific reports 3 (2013) 1900.

[175] J. Ribeiro-Soares, M. Oliveros, C. Garin, M. David, L. Martins, C. Almeida, E. Martins-Ferreira, K. Takai, T. Enoki, R. Magalhães-Paniago, Structural analysis of polycrystalline graphene systems by Raman spectroscopy, Carbon 95 (2015) 646-652.

[176] R. Blume, D. Rosenthal, J.P. Tessonnier, H. Li, A. Knop-Gericke, R. Schlögl, Characterizing Graphitic Carbon with X-ray Photoelectron Spectroscopy: A Step-by-Step Approach, ChemCatChem 7(18) (2015) 2871-2881.

[177] S. Chen, Y. Xin, Y. Zhou, F. Zhang, Y. Ma, H. Zhou, L. Qi, Branched CNT@SnO2 nanorods@carbon hierarchical heterostructures for lithium ion batteries with high reversibility and rate capability, Journal of Materials Chemistry A 2(37) (2014) 15582-15589.

[178] Z. Mohd Ishak, P. Shang, J. Karger-Kocsis, A modulated DSC study on the in situ polymerization of cyclic butylene terephthalate oligomers, Journal of Thermal Analysis and Calorimetry 84(3) (2006) 637-641.

[179] H.-B. Zhang, W.-G. Zheng, Q. Yan, Z.-G. Jiang, Z.-Z. Yu, The effect of surface chemistry of graphene on rheological and electrical properties of polymethylmethacrylate composites, Carbon 50(14) (2012) 5117-5125.

[180] H. Kim, A.A. Abdala, C.W. Macosko, Graphene/polymer nanocomposites, Macromolecules 43(16) (2010) 6515-6530.

[181] H. Chen, C. Huang, W. Yu, C. Zhou, Effect of thermally reduced graphite oxide (TrGO) on the polymerization kinetics of poly(butylene terephthalate) (pCBT)/TrGO nanocomposites prepared by in situ ring-opening polymerization of cyclic butylene terephthalate, Polymer 54(6) (2013) 1603-1611.

[182] D.G. Papageorgiou, I.A. Kinloch, R.J. Young, Graphene/elastomer nanocomposites, Carbon 95 (2015) 460-484.

[183] T. Abt, M. Sánchez-Soto, A Review of the Recent Advances in Cyclic Butylene Terephthalate Technology and its Composites, Critical Reviews in Solid State and Materials Sciences (2016) 1-45.

[184] F. Samyn, S. Bourbigot, C. Jama, S. Bellayer, S. Nazare, R. Hull, A. Castrovinci, A. Fina, G. Camino, Crossed characterisation of polymer-layered silicate (PLS) nanocomposite morphology: TEM, X-ray diffraction, rheology and solid-state nuclear magnetic resonance measurements, European Polymer Journal 44(6) (2008) 1642-1653.

[185] J. Vermant, S. Ceccia, M. Dolgovskij, P. Maffettone, C. Macosko, Quantifying dispersion of layered nanocomposites via melt rheology, Journal of Rheology (1978-present) 51(3) (2007) 429-450.

[186] Z. Ishak, K. Gatos, J. Karger-Kocsis, On the in-situ polymerization of cyclic butylene terephthalate oligomers: DSC and rheological studies, Polymer Engineering & Science 46(6) (2006) 743-750.

[187] R. Wagener, T.J. Reisinger, A rheological method to compare the degree of exfoliation of nanocomposites, Polymer 44(24) (2003) 7513-7518.

[188] H. Kim, Y. Miura, C.W. Macosko, Graphene/polyurethane nanocomposites for improved gas barrier and electrical conductivity, Chemistry of Materials 22(11) (2010) 3441-3450.

[189] N. Burger, A. Laachachi, M. Ferriol, M. Lutz, V. Toniazzo, D. Ruch, Review of thermal conductivity in composites: Mechanisms, parameters and theory, Progress in Polymer Science (2016).

[190] G. Balogh, S. Hajba, J. Karger-Kocsis, T. Czigány, Preparation and characterization of in situ polymerized cyclic butylene terephthalate/graphene nanocomposites, Journal of Materials Science 48(6) (2013) 2530-2535.

[191] S.A. Samsudin, S.N. Kukureka, M.J. Jenkins, The equilibrium melting temperature and isothermal crystallisation kinetics of cyclic poly (butylene

terephthalate) and styrene maleimide (c-PBT/SMI) blends, Journal of Thermal Analysis and Calorimetry 114(3) (2013) 1307-1315.

[192] C.M. Wu, C.W. Jiang, Crystallization and morphology of polymerized cyclic butylene terephthalate, Journal of Polymer Science Part B: Polymer Physics 48(11) (2010) 1127-1134.

[193] S. Colonna, M. Bernal, G. Gavoci, J. Gomez, C. Novara, G. Saracco, A. Fina, Effect of processing conditions on the thermal and electrical conductivity of poly (butylene terephthalate) nanocomposites prepared via ring-opening polymerization, Materials & Design (2017).

[194] R. Pérez, M. Córdova, J. López, J. Hoskins, B. Zhang, S. Grayson, A. Müller, Nucleation, crystallization, self-nucleation and thermal fractionation of cyclic and linear poly (ε-caprolactone) s, Reactive and Functional Polymers 80 (2014) 71-82.

[195] Z. Li, J. Wang, R.A. Pérez-Camargo, A.J. Müller, B. Zhang, S.M. Grayson, W. Hu, Non-monotonic molecular weight dependence of crystallization rates of linear and cyclic poly (epsilon-caprolactone) s in a wide temperature range, Polymer International 65(9) (2016) 1074-1079.

[196] A.J. Müller, R.M. Michell, A.T. Lorenzo, Isothermal Crystallization Kinetics of Polymers, Polymer Morphology: Principles, Characterization, and Processing (2016) 181-203.

[197] A. Lorenzo, A. Müller, Estimation of the nucleation and crystal growth contributions to the overall crystallization energy barrier, Journal of Polymer Science Part B: Polymer Physics 46(14) (2008) 1478-1487.

[198] R.A. Pérez, J.V. López, J.N. Hoskins, B. Zhang, S.M. Grayson, M.T. Casas, J. Puiggalí, A.J. Müller, Nucleation and antinucleation effects of functionalized carbon nanotubes on cyclic and linear poly (ε-caprolactones), Macromolecules 47(11) (2014) 3553-3566.

[199] B. Fillon, B. Lotz, A. Thierry, J. Wittmann, Self-nucleation and enhanced nucleation of polymers. Definition of a convenient calorimetric “efficiency scale” and evaluation of nucleating additives in isotactic polypropylene (α phase), Journal of Polymer Science Part B: Polymer Physics 31(10) (1993) 1395-1405.

[200] A.J. Müller, M.L. Arnal, M. Trujillo, A.T. Lorenzo, Super-nucleation in nanocomposites and confinement effects on the crystallizable components within block copolymers, miktoarm star copolymers and nanocomposites, European Polymer Journal 47(4) (2011) 614-629.

[201] J. Dai, Y. Shen, J.-h. Yang, T. Huang, N. Zhang, Y. Wang, Crystallization and melting behaviors of polypropylene admixed by graphene and β-phase nucleating agent, Colloid and Polymer Science 292(4) (2014) 923-933.

[202] I. Arandia, A. Mugica, M. Zubitur, A. Iturrospe, A. Arbe, G. Liu, D. Wang, R. Mincheva, P. Dubois, A.J. Müller, Application of SSA thermal fractionation and X-ray diffraction to elucidate comonomer inclusion or exclusion from the crystalline phases in poly (butylene succinate-ran-butylene azelate) random copolymers, Journal of Polymer Science Part B: Polymer Physics 54(22) (2016) 2346-2358.

[203] H. Parton, J. Baets, P. Lipnik, B. Goderis, J. Devaux, I. Verpoest, Properties of poly(butylene terephthatlate) polymerized from cyclic oligomers and its composites, Polymer 46(23) (2005) 9871-9880.

[204] M. Yasuniwa, S. Tsubakihara, K. Ohoshita, S.i. Tokudome, X-ray studies on the double melting behavior of poly (butylene terephthalate), Journal of Polymer Science Part B: Polymer Physics 39(17) (2001) 2005-2015.

[205] I. Desborough, I. Hall, A comparison of published crystalline structures of poly (tetramethylene terephthalate), Polymer 18(8) (1977) 825-830.

[206] Z.-f. Li, Z. Zhang, H.-x. Feng, Z.-b. Wang, Y. Li, P. Chen, Correlation between polymerization of cyclic butylene terephthalate (CBT) and crystallization of polymerized CBT, Chinese Journal of Polymer Science 33(8) (2015) 1104-1113.

[207] H. Münstedt, Z. Starý, Is electrical percolation in carbon-filled polymers reflected by rheological properties?, Polymer (2016).

[208] B. Krause, R. Boldt, P. Pötschke, A method for determination of length distributions of multiwalled carbon nanotubes before and after melt processing, Carbon 49(4) (2011) 1243-1247.

[209] H. Kim, C.W. Macosko, Morphology and properties of polyester/exfoliated graphite nanocomposites, Macromolecules 41(9) (2008) 3317-3327.